

# **Genetically- and spatially-defined basolateral amygdala neurons control food consumption and social interaction**

Dissertation an der Fakultät für Biologie der Ludwig-Maximilians-Universität München zur Erlangung des akademischen Grades eines Doktor der Naturwissenschaften (Dr. rer. nat.)

24.11. 2023

**Hansol Lim**



Diese Dissertation wurde angefertigt

unter der Leitung von Prof. Dr. Rüdiger Klein in der Abteilung Moleküle – Signale –  
Entwicklung am Max-Planck-Institut FÜR BIOLOGISCHE INTELLIGENZ in Martinsried,  
Deutschland.

Erstgutachter: Prof. Dr. Rüdiger Klein

Zweitgutachter: Prof. David Keays

Tag der Abgabe: November 24, 2023

Tag der mündlichen Prüfung: May 3, 2024

### **Eidesstattliche Erklärung**

Ich versichere hiermit an Eides statt, dass die vorgelegte Dissertation von mir  
selbständig und ohne unerlaubte Hilfe angefertigt ist.

München, den.24.11.2023.....hansol lim .....

## Erklärung

Hiermit erkläre ich, \*

- ☒ dass die Dissertation nicht ganz oder in wesentlichen Teilen einer anderen Prüfungskommission vorgelegt worden ist.
- ☒ dass ich mich anderweitig einer Doktorprüfung ohne Erfolg **nicht** unterzogen habe.
- ☐ dass ich mich mit Erfolg der Doktorprüfung im Hauptfach ..... und in den Nebenfächern ..... bei der Fakultät für ..... der .....  
(Hochschule/Universität) unterzogen habe.
- ☐ dass ich ohne Erfolg versucht habe, eine Dissertation einzureichen oder mich der Doktorprüfung zu unterziehen.

München, den.24.11.2023..... ....hansol lim.....

\*) Nichtzutreffendes streichen

# Abstract

The basolateral amygdala (BLA) contains discrete neuronal circuits that integrate positive or negative emotional information and drive the appropriate innate and adaptive behavior. Whether these circuits consist of genetically-identifiable and anatomically segregated neuron types, is currently debated. Also, our understanding of the response patterns and behavioral spectra of genetically-identifiable BLA neurons is limited. Here, we classified 11 glutamatergic BLA cell types and their spatial distribution. Several clusters were enriched in lateral versus basal amygdala, others were enriched in either anterior or posterior regions of the BLA. We further found that two BLA subpopulations innately responded to valence-specific stimuli, whereas one represented both aversive and social cues. Positive-valence BLA neurons promoted normal feeding, while mixed selectivity neurons promoted fear learning and social interactions. These findings enhance our understanding of cell type diversity and spatial organization of the BLA and the role of distinct BLA populations in representing valence-specific and mixed stimuli.



## Contents

<b>Eidesstattliche Erklärung .....</b>	<b>2</b>
<b>Erklärung .....</b>	<b>3</b>
<b>Abstract .....</b>	<b>4</b>
<b>Introduction .....</b>	<b>9</b>
1.1 The Amygdala .....	9
1.1.1 Cellular composition of BLA .....	10
1.1.2 Genetically identified neurons in the BLA .....	11
1.1.3 Development of amygdala .....	13
1.2 Neural circuits of emotion in BLA .....	14
1.2.1 Which kind of information is processed in the BLA? .....	14
1.2.2 BLA and Fear .....	15
1.2.3 BLA and reward .....	18
1.2.4 Valence coding in BLA .....	19
1.2.5 The amygdala in social behavior .....	20
1.3 Advanced methods to identify, manipulate and observe cell types .....	21
1.3.1 Identify cell types in transcriptomics: single cell (nucleus) RNA sequencing (sc(n)RNA seq) .....	21
1.3.2 Identify cell types in anatomy: sequential multiplexed in situ hybridization (smFISH) .....	23
1.3.3 Manipulate cell types: Cre mice and Optogenetics .....	25
1.3.4 Observe neural activities of cell types: in vivo Calcium imaging .....	27
<b>Thesis summary .....</b>	<b>29</b>
<b>Materials and Methods .....</b>	<b>31</b>
3.1 Animals .....	31
3.2 Viral constructs .....	31
3.3 Single nucleus RNA sequencing .....	32

3.3.1	Preparation .....	32
3.3.2	Single nucleus isolation and library preparation .....	32
3.3.3	snRNA-Seq analysis .....	33
3.3.4	Marker-gene selection for glutamatergic neurons for spatial validation (smFISH) .....	36
3.4	Hairpin chain reaction (HCR) sequential multi-fluorescent in situ hybridization.....	37
3.4.1	Preparation and imaging .....	37
3.4.2	Data analysis for HCR.....	38
3.5	Stereotaxic surgeries.....	39
3.6	Acute brain slice preparation and electrophysiological recordings ..	40
3.7	Behavior paradigms.....	41
3.7.1	Feeding experiments.....	41
3.7.2	Social interaction test .....	41
3.7.3	Contextual fear conditioning (cFC) .....	42
3.7.4	Optogenetic conditional place preference(avoidance) test. ....	43
3.7.5	Open field task (OFT).....	44
3.8	Optogenetic manipulations .....	44
3.9	In vivo Ca <sup>2+</sup> imaging of freely moving mice .....	44
3.9.1	Imaging.....	44
3.9.2	Preprocessing.....	45
3.9.3	Calcium data analysis for Food and Social assay and fear conditioning .....	45
3.10	Histology .....	47
3.11	Immunohistochemistry.....	48
3.12	Data Analysis (statistics) .....	48
<b>Results</b>	.....	<b>50</b>
4.1	Single-nuclei transcriptomic characterization of adult BLA neuronal types .....	50
4.2	Transcriptional correlation of genes spatially marked BLA subregions	55

Spatial organization of glutamatergic BLA clusters .....	55
The combination of marker genes predicts the spatial localization in the BLA.....	62
4.3 Expression of transcriptional clusters in BLA subregions .....	66
4.4 Cell type specific- functional circuits for valence.....	71
4.4.1 Activities of BLA <sup>Lypd1</sup> neurons increase during fasting and feeding .....	71
4.4.2 BLA <sup>Etv1</sup> neurons are activated by innate fear stimuli.....	84
4.4.3Activities of BLA <sup>Etv1</sup> neurons increase during social interactions ..	84
4.4.4 BLA <sup>Lypd1</sup> neurons promote normal food uptake. ....	89
4.4.5 BLA <sup>Etv1</sup> neurons are necessary for fear memory formation.....	92
4.4.6 BLA <sup>Etv1</sup> neurons are necessary for social interaction.....	92
4.5 GO terms and comparison with published data supported our transcriptional, anatomical and functional populations in BLA.....	97
<b>Discussion.....</b>	<b>101</b>
5.1 Summary of thesis findings .....	101
5.2 The similarity of GABAergic interneurons between cortex and BLA .	101
5.3 Molecularly-defined glutamatergic BLA cell types.....	102
5.4 Spatial organization of glutamatergic BLA clusters.....	103
5.5 Putative additional function of marker gene-identified neuronal populations .....	103
5.6 Activity profiles of three transcriptional, anatomically defined neurons during fasting and re-feeding.....	104
5.7 The distinct neuronal responses of BLA <sup>Rspo2</sup> and <sup>Etv1</sup> neurons for negative, <sup>Lypd1</sup> neurons for positive valence, but BLA <sup>Etv1</sup> uniquely for social valence. ....	105
5.8 Informing and Interpreting future Experiments.....	109
<b>Abbreviations .....</b>	<b>110</b>
<b>References.....</b>	<b>113</b>
<b>Declaration .....</b>	<b>Error! Bookmark not defined.</b>

<b>Author Contributions .....</b>	<b>129</b>
<b>CV .....</b>	<b>129</b>

# Introduction

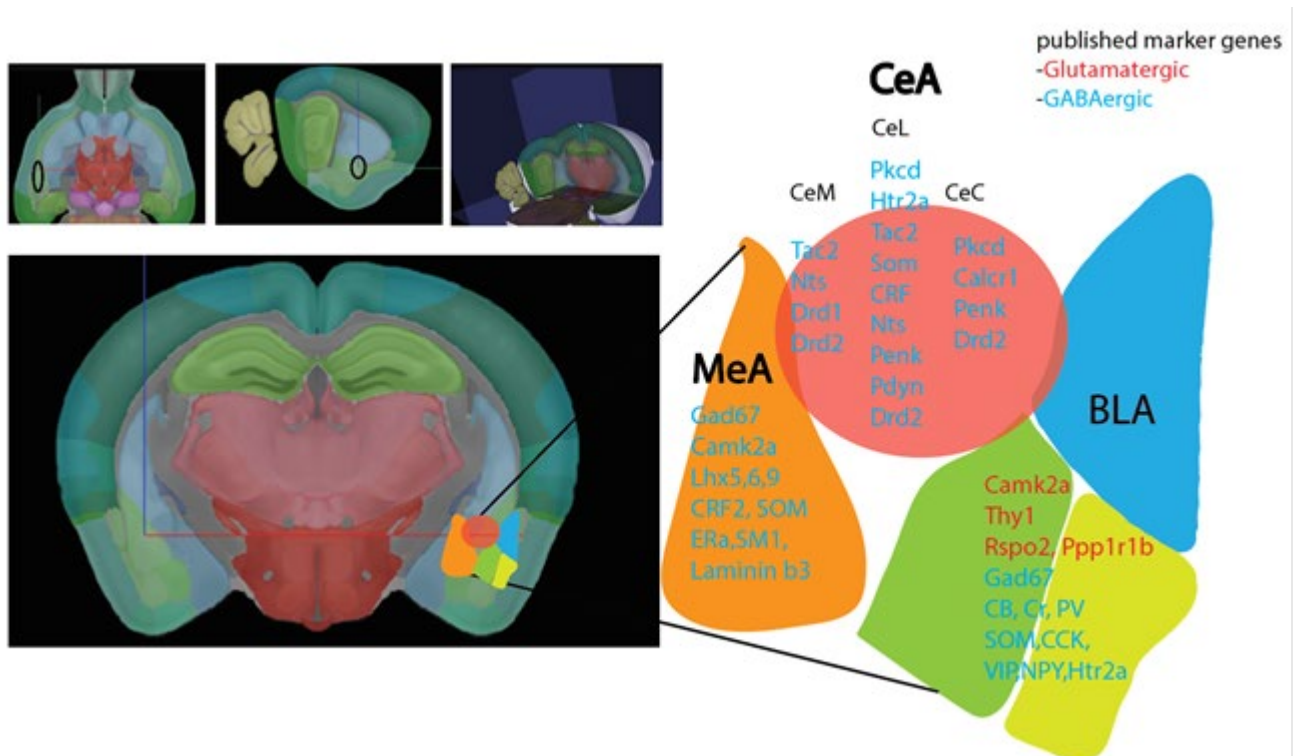
## 1.1 The Amygdala

All organisms exhibit emotional behaviors, which are defined as behavioral responses to stimuli of emotional significance, such as those related to food or threats. The amygdala is widely recognized as a central neural hub for processing emotions. The remarkable conservation of its circuitry and function across evolutionary scales (McDonald 1998a), underscores the fundamental role that emotional processing and the amygdala play in the lives of organisms. Notably, even non-mammalian species, including reptiles, birds, and fish, possess a brain region akin to the amygdala, exhibiting similar circuitry and functions to their mammalian counterparts (Jarvis et al. 2005; Lanuza et al. 1998a). The amygdala is comprised of various interconnected nuclei, predominantly the basolateral amygdala complex (BLA), consisting of the lateral (LA), basal (BA), and basomedial (BM) components, alongside the central nucleus of the amygdala (CeA), composed of lateral (CeL) and medial (CeM) subdivisions (Intro\_Figure1). Notably, the BLA receives environmental information from the sensory thalamus and cortices, projecting prominently to the LA. Subsequently, the LA projects intrinsically within the BLA, extending to the BA, BM, and CeA (Intro\_Figure 2). Moreover, the BLA maintains reciprocal connections with cortical regions, particularly the midline and orbital prefrontal cortices (PFCs), the hippocampus (HPC), as well as sensory association areas (Freese and Amaral 2005; McDonald 1998) (Intro\_Figure 2). Consequently, it is firmly established that the BLA functions as a central processing hub for a wide array of information.

### 1.1.1 Cellular composition of BLA

Based on Golgi staining studies conducted in rats, BLA neurons have been categorized into two principal classes: pyramidal neurons, characterized as excitatory neurons releasing glutamate, constituting up to 95% of the neuronal population, and local interneurons, a smaller subset representing approximately 5% of Golgi-impregnated neurons (McDonald 1982). Pyramidal neurons typically exhibit between 3 to 7 dendrites emanating from their soma, often with one prominent dendrite analogous to the apical dendrite found in cortical neurons (Sah and Lopez De Armentia 2003). Unlike pyramidal neurons in the cortex or hippocampus, those within the BLA lack a discernible layered organization and are distributed in a seemingly arbitrary manner. Notably, the axons of pyramidal neurons extend beyond the BLA, giving rise to several collaterals that intricately arborize within the BLA. In contrast, local interneurons in the BLA feature between two to six primary dendrites and are characterized by dendrites with sparse spines, accompanied by dense local axonal arborizations. These interneurons can be further classified into subtypes, such as multipolar, bi-tufted, bipolar, and chandelier cells, contingent upon their specific dendritic branching patterns. These cells predominantly release gamma amino-butyric acid (GABA) (McDonald and Augustine 1993).

Furthermore, based on the somatic size of pyramidal cells, the Basal Amygdala (BA) has been subcategorized into three distinct subfields: the magnocellular, intermediate, and parvocellular subdivisions (Pitkänen et al., 1997). The magnocellular segment corresponds to the anterior BA (aBA), where pyramidal neurons possess larger cell bodies (Björklund, Hökfelt, and Swanson 1987), while projection neurons within the parvocellular subdivision exhibit smaller cell bodies. Lastly, the intermediate BA was initially delineated in rats as the transitional region between the magnocellular and parvocellular BA, where the diminishing anteroposterior gradient of large pyramidal cells intersects with the ascending gradient of small pyramidal cells.



**Intro\_Figure1. The anatomy of amygdala complex and genetically identified populations.** 3-dimensional anatomy of amygdala complex with the bottom view (top right) and sagittal section (top middle) and overall location of amygdala complex in whole mouse brain (top left). The coronal section of the mouse brain shows an amygdala complex and schematic illustration showed several amygdala nuclei. green/blue-colored BLA regions are more similar to the cortex therefore, they are called Cortical like regions, whereas orange or red-colored regions (CeA or MeA) are closer to the striatum (striatal-like) (Adapted from (Beyeler and Dabrowska 2020 and Allen mouse brain Atlas)

### 1.1.2 Genetically identified neurons in the BLA

In the BLA, akin to other cortical regions, glutamatergic neurons express calcium/calmodulin-dependent protein kinase IIa (Camk2a) (A J McDonald, Muller, and Mascagni 2002) (Intro\_Figure 1). Noteworthy is the ubiquity of Camk2a within all pyramidal cells, distinguishing them from the smaller non-pyramidal neurons (interneurons), which lack this marker. Consequently, Camk2a serves as a selective indicator of glutamatergic pyramidal neurons in the BLA, though it is imperative to acknowledge recent sequencing findings, which introduced the potential utilization of Camk2a as a marker for projecting neurons by revealing Camk2a+ inhibitory neurons of parvalbumin or somatostatin subtypes

(Keaveney et al. 2020). Furthermore, a subset of glutamatergic neurons within the BLA expresses thymus cell antigen 1 (Thy1)(Jasnow et al. 2013). Optogenetic and chemogenetic activations of Thy1-expressing neurons inhibit fear consolidation and accelerate memory extinction, respectively (McCullough et al. 2016). Conversely, optogenetic inhibition of Thy1 neurons has been observed to diminish fear extinction (Intro\_Figure 1), confirming Thy1+ neurons as pivotal contributors to fear modulation. Within this subset, two electrophysiologically distinct populations of BLA neurons have been discerned based on their response to the extinction of a conditioned cue and an electric shock (Herry et al., 2008). The initial population exhibited a "fear-on" response, characterized by an augmented firing frequency in reaction to the predictive cue during and after fear conditioning, but a reduced firing frequency during extinction training. In contrast, the second population, denoted as "fear-off" neurons, manifested increased firing rates exclusively in response to the cue during extinction training. Additionally, molecular scrutiny of Thy1+ neurons employing RNA sequencing identified genes that were markedly upregulated in this population, including those encoding the neurotensin receptor 2 (Ntsr2) and Rspo2 (Rspodin-2) (McCullough et al. 2016). Significantly, pharmacological interventions targeting Ntsr2 neurons suggested that neurons expressing Ntsr2 within the BLA are prospective "Fear-OFF" (McCullough et al. 2016). In alignment with this, a recent study demonstrated that neurotensin (NT)-expressing neurons in the paraventricular nucleus of the thalamus (PVT) projecting to the BLA bolstered reward valence (Li et al. 2022). Conversely, the same study found that Rspo2-expressing neurons are "Fear-ON" neurons, displaying heightened responses to negative valence stimuli (Kim et al. 2016; Zhang et al., 2020). Moreover, RNA sequencing unveiled an elevation in mRNA levels when contrasting various projector populations. Notably, the BLA-CeM projectors exhibited over four-fold higher levels of mRNA for the Ntsr1 1 compared to the BLA-NAc projectors. These findings imply a potential functional disparity between these two populations(Namburi et al. 2015a) . Nevertheless, it is important to note that these markers are not exclusive and do not allow for the precise genetic targeting of a specific projector population. A recent investigation employing activity-dependent profiling via fos promoter, combined with gene screening, (Kim et al. 2016) has shown that anterior magnocellular and posterior parvocellular projection neurons can be delineated by the expression of distinct gene markers. Neurons expressing Rspo2, located in the anterior BLA, correspond to the magnocellular neurons, whereas neurons expressing Ppp1r1b, encoding the protein



phosphatase 1 regulatory inhibitor subunit 1B (DARPP-32), are situated in the posterior BLA and correspond to parvocellular neurons (Intro\_Figure 1). Intriguingly, optogenetic stimulation of *Rspo2*<sup>+</sup> cells elicit a negative response in naïve mice, while stimulation of *Ppp1r1b*<sup>+</sup> cells induces a positive response (J. Kim et al. 2016). Both populations project to the NAc and CeA, with *Rspo2*<sup>+</sup> cells forming monosynaptic contacts with *PKCδ*<sup>+</sup> cells of the CeC for negative valence, whereas *Ppp1r1b*<sup>+</sup> cells innervate the other cellular subtypes of the CeM and CeL for positive valence (Kim et al. 2017). Moreover, a recent investigation utilizing a cholecystokinin (CCK) reporter mouse line has disclosed that the projection neurons in the BLA can be categorized as either CCK (+) or CCK (-), and the optogenetic stimulation of these two BLA subpopulations into the NAc-core elicits distinct behaviors associated with negative and positive valence (Shen et al. 2019) (Intro\_Figure1).

### **1.1.3 Development of amygdala**

Furthermore, an intriguing area of inquiry pertains to the origin of this diverse array of BLA neuronal subpopulations. Are these subpopulations predetermined during early developmental stages? If so, could specific precursor cells be identified for each population? Prior investigations into the progenitors of amygdala excitatory neurons have focused on key transcription factors such as *Pax6*, *Emx1*, and *Tbr1*. These factors exhibit intricate expression patterns within the mouse embryonic telencephalon, with *Tbr1*<sup>+</sup> neurons giving rise to the entirety of the basal lateral amygdala, while *Pax6*<sup>+</sup> neurons contribute predominantly to the basal medial regions of the amygdala (Cocas et al. 2009). Additionally, studies have revealed distinct spatial distributions of neurons expressing *Tbr1*, *Ngn2*, and *Sema5a* at embryonic day E18.5, with dense concentration observed exclusively in the lateral amygdala (LA), while *Cad8* and *Emx1*-positive neurons were primarily situated in the basal amygdala (BA) (Gorski et al. 2002; Medina et al. 2004). However, a comprehensive investigation encompassing fate mapping from progenitor cells to mature neuronal subtypes within the amygdala remains an unexplored frontier.

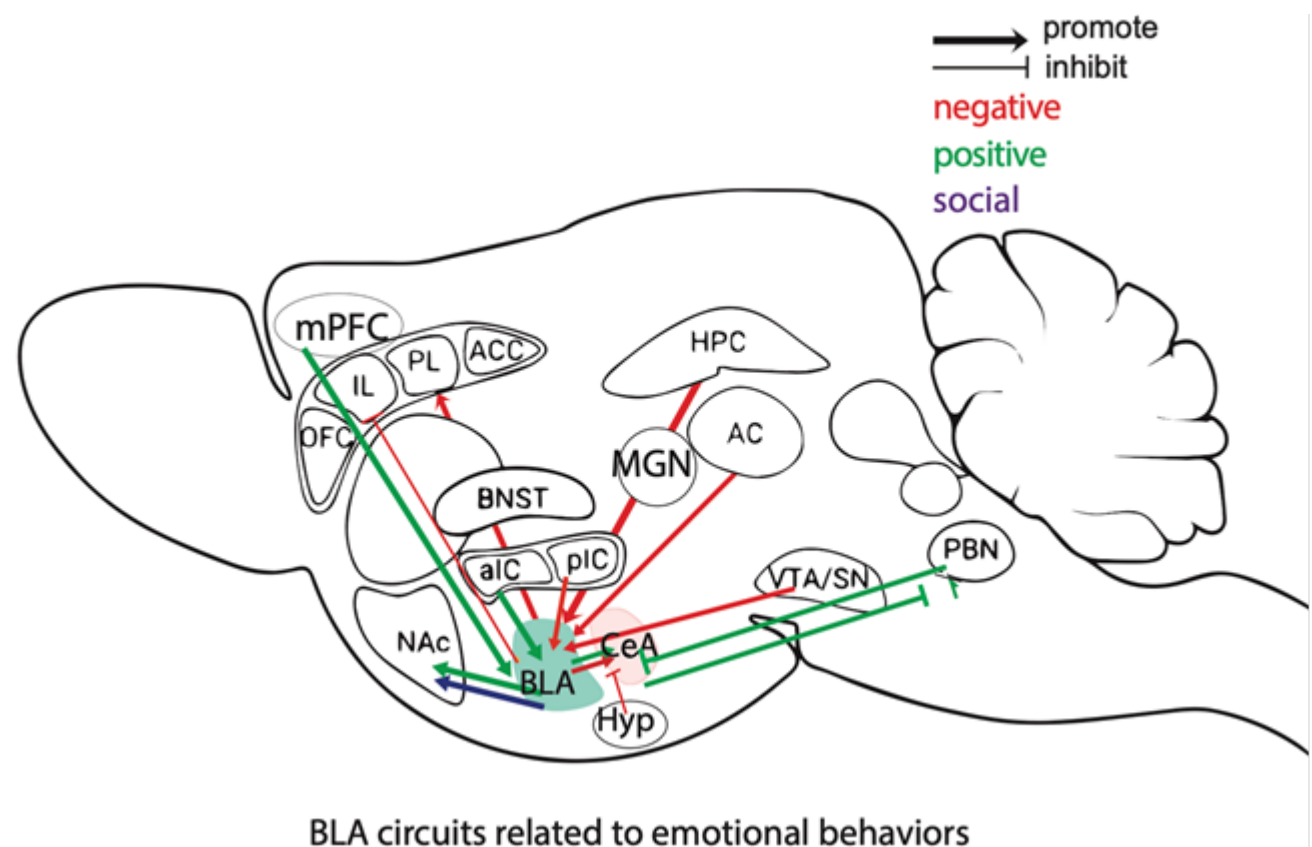
Noteworthy transformations are not confined to the embryonic phase; the postnatal development of the BLA also undergoes significant changes. The adolescent transition, for instance, ushers in notable alterations in the neuronal encoding of emotions, particularly in relation to fear (Ganella et al. 2018; Ganella and Kim 2014) or autism spectrum disorders (ASD) related to social interaction (Chevallier et al. 2012; Ferri et al. 2016). Moreover, this

transitional period is marked by synaptic, behavioral, and anatomical plasticity within the BLA (Johnson et al. 2016).

## 1.2 Neural circuits of emotion in BLA

### 1.2.1 Which kind of information is processed in the BLA?

The BLA is especially considered as a neural hub for emotionally driven behaviors, including aversive states like fear (Bergstrom et al. 2013; Fanselow and LeDoux 1999; Maren and Quirk 2004) and anxiety (Daviu et al. 2019). In addition to the analysis of negative valence settings, there has been a growing body of research indicating the involvement of the BLA in appetitive and reward-driven behavior (Baxter and Murray 2002; Wassum and Izquierdo 2015), as well as social interaction and associated neuropsychiatric conditions. (Ashwin et al. 2007; Bookheimer et al. 2008; Felix-Ortiz et al. 2016; Felix-Ortiz and Tye 2014a; Kennedy and Adolphs 2012) (Intro\_Figure 2).



**Intro\_Figure2. Diverse connection networks for emotional behaviors are studied by optogenetic or pharmacogenetic manipulation.** The arrow or end lines indicate promotion or inhibition of certain behaviors, respectively. AC, auditory cortex; BNST, bed nucleus of the stria terminalis; CeA, central nucleus of the amygdala;; EC, entorhinal cortex; Hyp, hypothalamus; IL, infralimbic; MGN, medial geniculate nucleus; mPFC, medial prefrontal cortex; NAc, nucleus accumbens; PBN, parabrachial nucleus; PL, prelimbic; aIC, anterior insular cortex; pIC, posterior insular cortex(Adapted from (Janak and Tye 2015 and Lieselot L.G et al., 2023)).

### 1.2.2 BLA and Fear

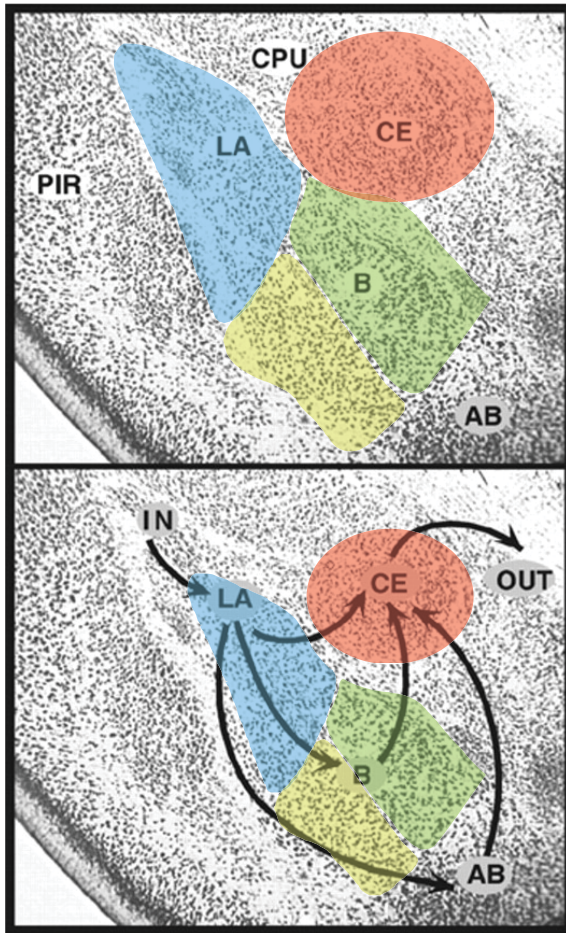
The amygdala is the neuroanatomical center of fear memory. The central role of BLA in emotional learning and memory was deeply studied during Pavlovian fear conditioning (Maren 2005). In short, conditioned fear is mediated by the transmission of information about an initially neutral stimulus (conditioned stimulus [CS]) paired in time with a different noxious stimulus (unconditioned stimulus [US]). In the laboratory, usually, a tone [CS] is associated with a foot shock [US]. The input about the CS and US arrives in the BLA, where it is processed, and from where fear reactions are expressed by way of output projections to the behavioral, autonomic, and endocrine response control systems located in the brainstem (LeDoux 2000)(Intro\_Figure 3). As a result, the CS elicits defensive or fear responses, such as freezing, when presented alone (Sigurdsson et al. 2007). Fear conditioning is crucial for animals to predict and avoid harmful situations and is therefore crucial to survival.

Fear conditioning has been studied with two different pathways of CS. One is auditory CS and another is context CS. Firstly, this tone CS pathway was considered hippocampus-independent and solely mediated by the amygdala. Therefore, the convergence of synaptic inputs about the CS and the US leads to the potentiation of synapses conveying CS information to the LA. Auditory and somatosensory information reaches the LA from auditory regions and is then relayed to the CeA, (Mascagni, McDonald, and Coleman 1993; Romanski and LeDoux 1993) then, projects to areas of the brainstem and hypothalamus

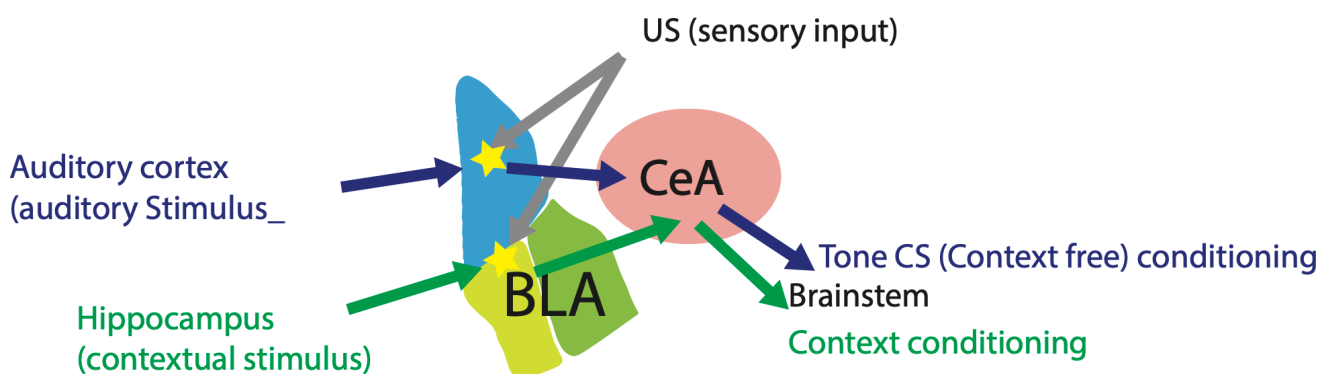
that control the expression of defensive behavior, hormonal secretions and autonomic responses (Sigurdsson et al. 2007).

In addition to expressing fear responses to the tone, rats also exhibit these when returned to the chamber in which the tone and shock were paired, or a chamber in which shocks occur alone. This is called contextual fear conditioning and requires both the amygdala and the hippocampus (Phillips 1992). Shortly, inputs from areas of the ventral hippocampus project to the B and AB nuclei of the amygdala and then next, to the brainstems for behavior response (Intro\_Figure 4).

Overall, two types of CS, before conditioning, the CS inputs are relatively weak, being unable to elicit fear responses; in contrast, the US inputs are stronger and capable of eliciting robust responses in LA neurons. Since CS and US inputs converge onto LA neurons, during fear conditioning the CS inputs are active during strong postsynaptic depolarization caused by the US. As a result, the CS becomes stronger and more effective, called “potentiation”, at driving LA neurons that can subsequently activate downstream structures. Thus, in the original model, a main station is considered LA for CS formation of tone, BA for CS formation of context, and CeA for conditioned fear responses (Pare and Duvarci 2012).



**Intro\_Figure3. Fear circuits in the amygdala.** The amygdala consists of several different regions. Those of most relevance to the pathways of fear conditioning are the lateral (LA), basal (B), accessory basal (AB), and central (CE) nuclei. The piriform cortex (PIR) lies lateral to the amygdala, and the caudate-putamen (CPU) is just dorsal to it in the Nissl-stained section (upper). The major pathways connecting LA, B, AB, and CE are shown (bottom). (Adapted from (LeDoux 2000))



**Intro\_Figure 4. Two types of Fear conditioning.** Conditioning to a tone [conditioned stimulus (CS)] involves projections from the auditory system to the lateral nucleus of the amygdala (LA) and from LA to the central nucleus of the amygdala (CE). In contrast, conditioning to the apparatus and other contextual cues present, when the CS and unconditioned stimulus are paired, involves the representation of the context by the hippocampus and the communication between the hippocampus and the basal (B) and accessory basal (B) nuclei of the amygdala, which in turn project to CE. Footshock (unconditioned stimulus (US)) from sensory circuits generated potentiation (star-marked) to strengthen the synaptical connection for CS and US and it resulted in fear conditioning (Adapted from (LeDoux 2000)).

### 1.2.3 BLA and reward

Previous anatomical, developmental, and transcriptional studies have indicated a diverse range of neuronal responses in the BLA. In addition to fear, research has shown that amygdala lesions can also impair reward-based behaviors (Cador, Robbins, and Everitt 1989a; Everitt, Cador, and Robbins 1989; Hatfield et al. 1996; Hiroi and White 1991; Málková, Gaffan, and Murray 1997). For instance, LA lesions have been found to prevent amphetamine place preference conditioning. Also, BLA neurons have been observed to develop excitatory responses to a CS paired with aversive outcomes, as well as to auditory, visual, or olfactory CSs paired with rewarding outcomes such as sweet liquid or food pellets (Sanghera, Rolls, and Roper-Hall 1979; Schoenbaum, Chiba, and Gallagher 1998; Tye et al. 2008; Tye and Janak 2007; Uwano et al. 1995).

Interestingly, amygdala lesions did impair the ability to respond to cues in the face of changing reward value, leading to the hypothesis that learning mediated by the amygdala is related to the current, relative value of biologically significant outcomes (Balleine and Killcross 2006; Baxter and Murray 2002). The value of a reward is determined by its current biological significance, such as food being more significant when one is hungry. The amygdala provides information about an organism's "state value." The BLA and CeA have distinct roles in representing value, as demonstrated through procedures that alter the current value of an outcome. BLA lesions impair the ability to change behavior in response to specific reward outcomes. Therefore, the BLA is believed to represent outcome value and sensory features, allowing for discrimination among similar outcomes (Málková et al.

1997). In contrast, the CeA is thought to maintain a more general representation of the motivational significance of an outcome (Balleine and Killcross 2006).

### **1.2.4 Valence coding in BLA**

Since both negative and positive cues recruit BLA neurons, these findings raise the question of how the processing of two antagonistic cues by amygdala networks is organized. For example, would neurons with excitatory responses to negative cues also show increased activity to positive cues in conversion, or is there segregation of positive- and negative-valence signals; conversion, or diversion? This question was addressed by directly comparing neural responses in the same subjects simultaneously on both appetitive and aversive tasks. These within-subject comparisons in rodents and non-human primates consistently reveal populations of valence-selective neurons (Belova et al. 2007; Sangha, Chadick, and Janak 2013; Schoenbaum, Chiba, and Gallagher 1999; Shabel et al. 2011) such that some neurons excited by a fear cue do not respond to a reward cue, or even show inhibition in the presence of the reward cue, and vice versa. However, valence-encoding is complemented by salience-encoding; some BLA units show excitatory responses to both fear and reward cues (Belova et al. 2007). The intensity of a stimulus defines its salience, which can trigger responses related to arousal and attention, ultimately enhancing processing in the amygdala and target regions. A role in signaling the salience of stimuli agrees with the suggested contributions of the BLA in attention (Holland and Gallagher 1999; Roesch et al. 2012). Nevertheless, amygdala neuronal pairs sensitive to stimuli of the same valence are more likely to show correlated neural activity than neuronal pairs sensitive to opposite valences, supporting the idea of functional networks (Zhang et al. 2013).

The mechanisms by which the BLA mediates such diverse emotional information have been studied multimodally in anatomy, separating lateral and basal (basolateral) or anterior and posterior compartments (McDonald 1984a; Swanson and Petrovich 1998), and in connectivity by projection targets (Ambroggi et al. 2008; Beyeler et al. 2018; Cador, Robbins, and Everitt 1989; Felix-Ortiz et al. 2016; Hintiryan et al. 2021; Peng et al. 2015; Redondo et al. 2014; Stuber et al. 2011) (Intro\_Figure 2). Most recently, a transcriptional approach has shown different gene expression properties within BLA cell types (Kim et al. 2016; O'Leary et al. 2020) or within BLA subregions (Namburi et al. 2015; Zirlinger,

Kreiman, and Anderson 2001) to explain functional diversity in the BLA. However, the correlation between molecular diversity and spatial anatomy of BLA neurons has not been fully explored. Consequently, the functional importance of BLA subpopulations identified by both anatomical and molecular features is not well understood. It remains to be shown if transcriptional profiling of BLA neurons can aid in segregating these neurons anatomically and in selecting neurons that encode for opposing valences. Our study aimed at addressing this open question.

### **1.2.5 The amygdala in social behavior**

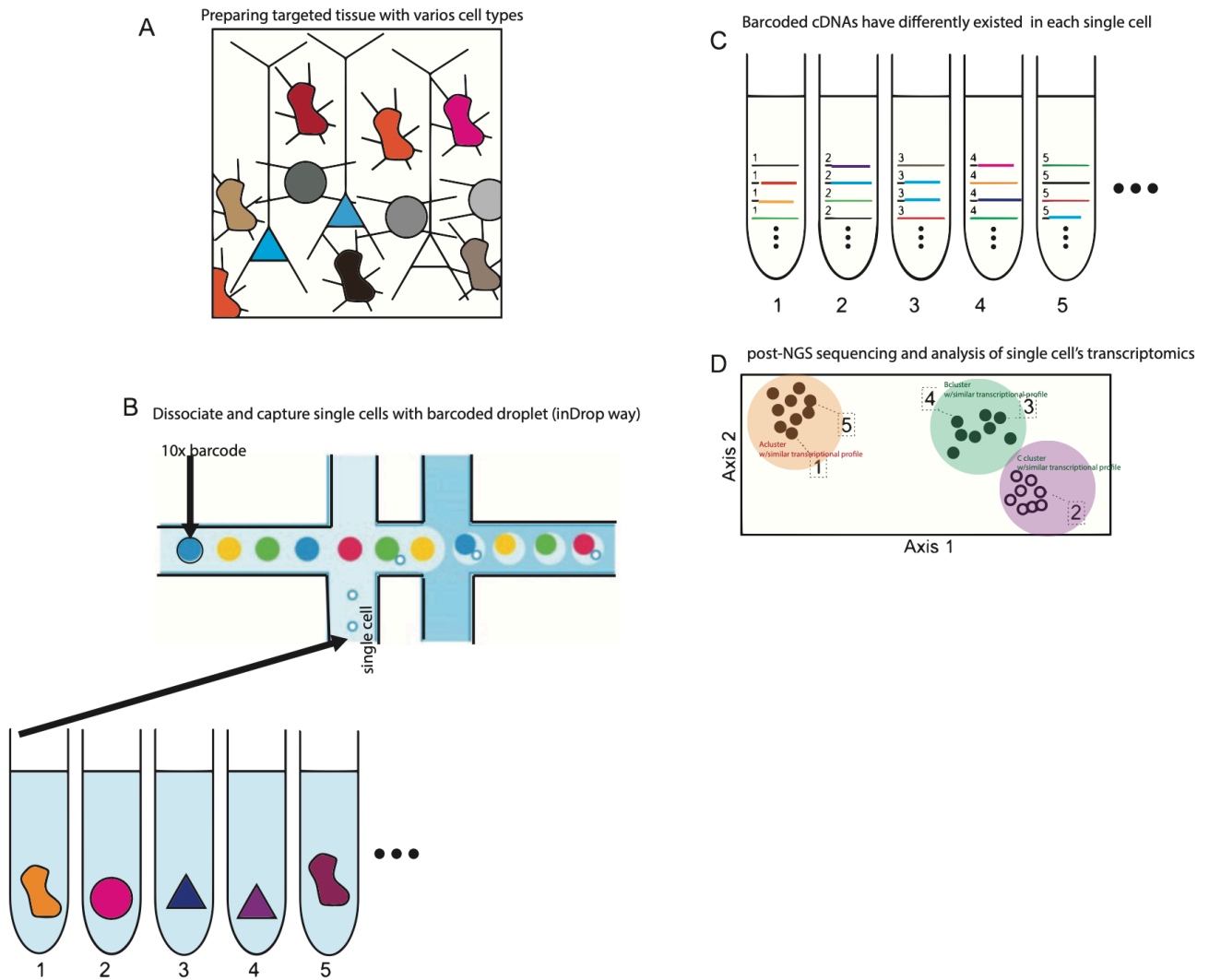
Apart from valence and salience-related behaviors, the BLA was also part of those brain areas necessary for social behavior, from the earliest descriptions of deficits that were produced by the removal of the temporal lobes, including the amygdala (Brown and Sharpey-Schafer 1997). One of the earlier lesion-based research studies claimed that the amygdala is necessary for survival (Kling, Lancaster, and Benitone 1970). In this study, adult monkeys with bilateral amygdala lesions showed no interest in others, did not behave according to their pre-surgical social status, ignored or failed to understand the signals of their peers, became isolated, defenseless, and anorexic, and died in a few weeks. Also, other studies confirmed that the amygdala plays a role in as such social decision-making (Bickart, Dickerson, and Feldman Barrett 2014), the representation of social status (Munuera, Rigotti, and Salzman 2018), the allocation of visual attention to social stimuli (Minxha et al. 2017), social anxiety (Klumpp and Fitzgerald 2018), the production of facial expressions (Gothard 2014), and the coordination of autonomic responses that are elicited by social stimuli (Laine et al. 2009).



## **1.3 Advanced methods to identify, manipulate and observe cell types**

### **1.3.1 Identify cell types in transcriptomics: single cell (nucleus) RNA sequencing (sc(n)RNA seq)**

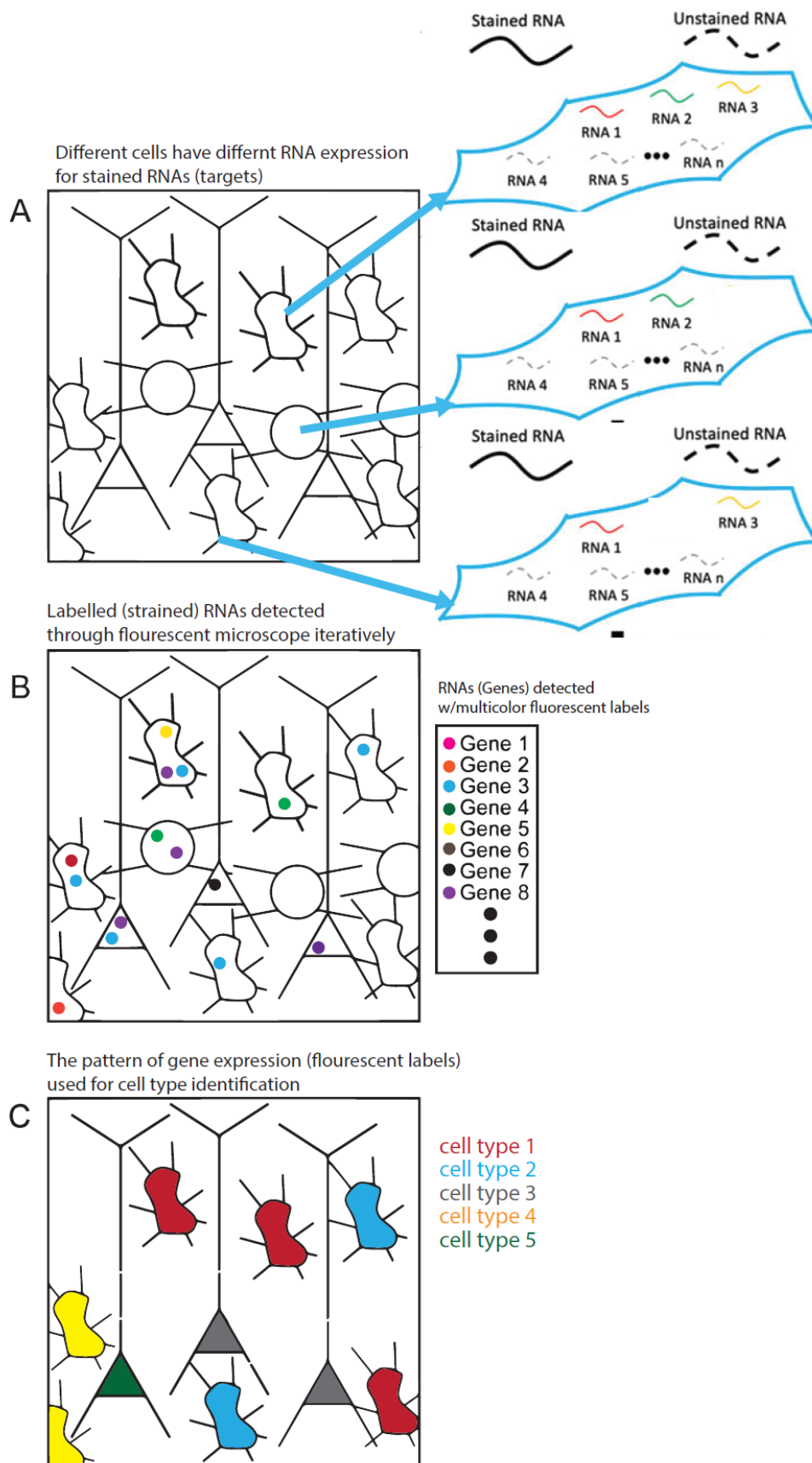
Single-cell or nucleus RNA sequencing, also known as sc(n)RNA-seq, involves the direct sequencing of RNA from individual cells (nuclei) to determine its abundance (Intro\_Figure 5). The process begins with the dissociation of tissue from specific regions of interest, followed by the capture of dissociated cells for sequencing. Next, cell capture is commonly performed in droplets (Intro\_Figure 5A and B). Each captured cell is linked to a distinct oligonucleotide barcode, which facilitates the unique identification of RNA from that particular cell in comparison to all other cells (Intro\_Figure 5C). Following Nanoliter-scale Gel Beads-in-emulsion (GEMs) generation, barcoded cDNA is synthesized from RNA using either in vitro transcription or polymerase chain reaction and then amplified. The amplified cDNA is then fragmented and joined to molecular adapters that enable high-throughput sequencing. Finally, sequencing is performed, with many small sequenced stretches (“reads”) obtained for the interrogated cells. After these reads are obtained, computational analysis is performed to derive cell types and their associated transcriptomic profiles (Intro\_Figure 5D) (Cembrowski 2019). The only difference between scRNA seq and snRNAseq use whole cells or isolated nuclei, respectively. In brief, to encapsulate single nuclei with mRNA-capture beads in nanolitre-scale droplets for snRNA seq, the collected tissue chunks from the brains were transferred in a homogenization buffer and after several filter steps, the nuclei were separated by ultracentrifugation. This additional procedure proceeded before the droplet generation step.



**Intro\_Figure 5. An overview of single-cell RNA sequencing workflow from** (adapted from Cembrowski 2019 and Pan, Y et al., 2022). A. Schematic of brain cells in tissue. B. After dissociation, individual cells are captured for sequencing here we showed 10x genomics in-Droplet barcoded RNA sequencing each barcode with one single cell to identify single cell later. C. After lysis and reverse transcription, cDNA is synthesized, with barcodes. D. After amplification and sequencing, the resulting data are analyzed. In this example, cells 1 and 5 share similar transcriptomes.

### **1.3.2 Identify cell types in anatomy: sequential multiplexed in situ hybridization (smFISH)**

The process for localizing RNA in a brain section using ISH involves several steps, as illustrated in Intro\_Figure 6. Initially, the genes of interest are identified, and probes are created that can hybridize to a specific sequence within each related transcript. To apply this probe to brain tissue, thin sections (usually  $\leq 20\ \mu\text{m}$ ) are obtained from a subject of interest using a cryostat, placed on slides, and frozen until needed (Intro\_Figure 6A). Ultimately, gene expression is observed by detecting amplified probe signals through either chromogenic or fluorescent methods (Intro\_Figure 6B). Advanced smFISH techniques, which use a multiplexed approach involving multiple rounds of hybridization, detection, and stripping, can detect hundreds or thousands of gene-expression targets within the same tissue section (Cembrowski 2019b; Cembrowski et al. 2018).



**Intro\_Figure 6. An overview of smFISH workflow** (Adapted from (Cembrowski 2019)).

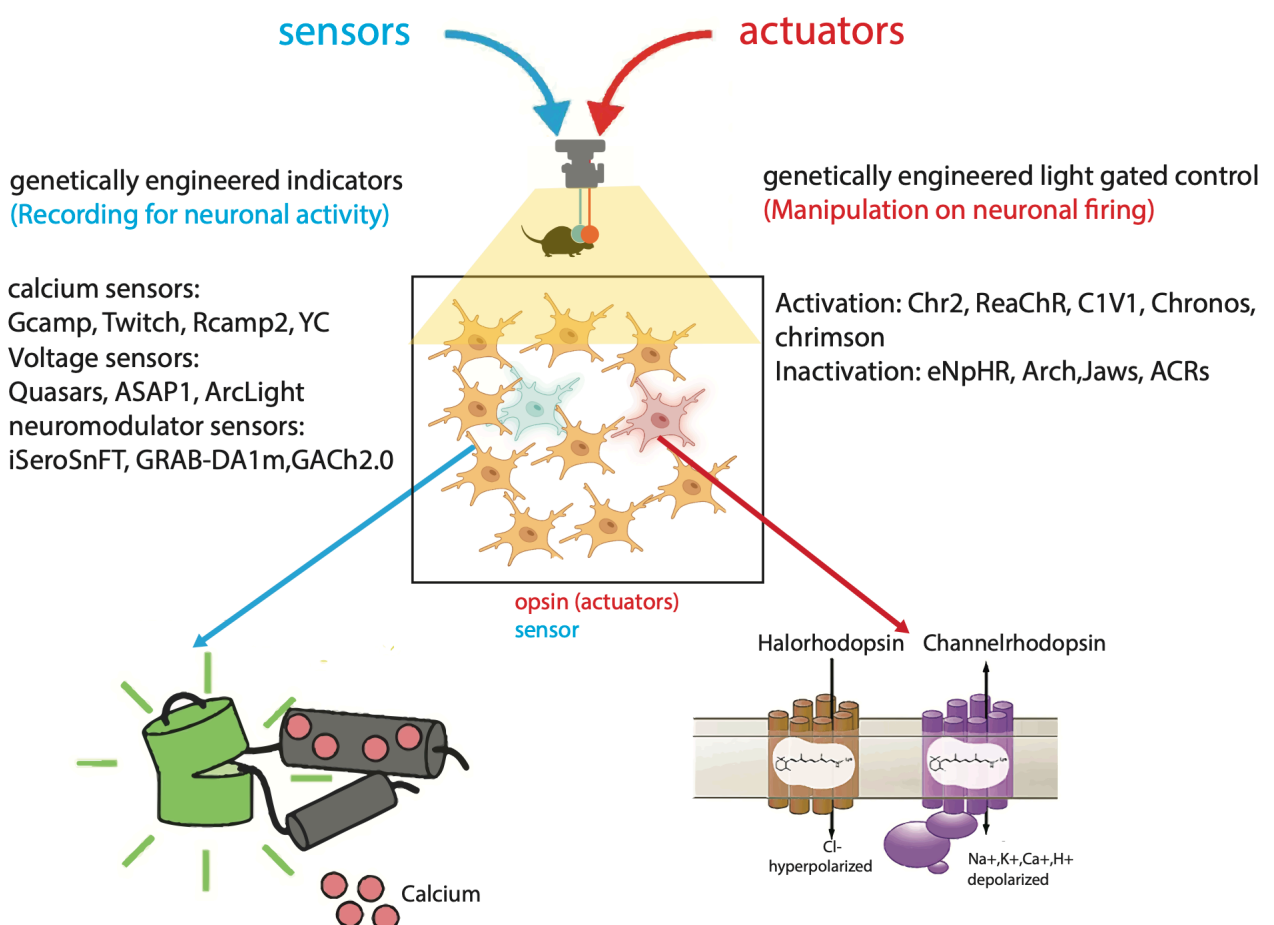
A. Schematic of brain cells in tissue. B. After fluorescent in situ hybridization, expression of each individual gene can be mapped onto all cells within the region of interest. Individual RNA molecules manifest as diffraction-limited puncta within the cytosol. C. After quantifying gene expression on a per-cell basis, cell types can be mapped to their respective spatial location.

### 1.3.3 Manipulate cell types: Cre mice and Optogenetics

One of the most common ways to classify neurons in recent years has been through the use of genetic markers to identify molecularly defined subpopulations. With the sc(n) RNA seq dataset, we could identify which genetic markers to use for purposes such as cell type genes or specific functional genes. After defining the gene, to target neural subpopulations in vivo, transgenic mice that express the cre recombinase enzyme are widely used. Cre is a bacteriophage enzyme that can be expressed under a specific promoter or enhancer, where an exogenous promoter or the Cre cDNA is inserted into the first coding exon of a gene of interest into the genome to strongly drive a gene of interest (Josh Huang and Zeng 2013). Next, to target cre-expressing neurons in a region of interest within the brain, genetically engineered adenoassociated viruses (AAVs) deliver the gene by flanking the specific trans-gene between short DNA sequences (lox sites), typically a stop fragment to hold transcription of the downstream sequence. Recombination between two sets of lox sites catalyzed by cre allows expression of the tool only in cre-expressing neurons.

Optogenetics is a tool considered as a key technique in circuit neuroscience. Optogenetic-based manipulation uses light-sensitive transmembrane proteins, opsins, that respond to light either by pumping ions into or out of the cells or by opening an ion channel. Defined populations of neurons are transduced with light-activated microbial opsins, allowing the activity of neurons to be controlled by light in a reversible and temporally and spatially specific manner. To achieve this, mice expressing cre in the neural population of interest are stereotactically injected with a cre-dependent AAV carrying the actuator opsin into the brain region of interest. The most common opsins are channelrhodopsin-2 (ChR2) for activation (Nagel et al. 2003) and halorhodopsins (NpHR) for inhibition (Chow et al.

2010) (Intro\_Figure 7, “manipulation”). Microbial-type rhodopsins represent membrane ion transport proteins; ChR2 are light-gated proton channels from the green alga *Chlamydomonas reinhardtii*, a cation channel that is activated by blue light (~450-490nm). Photon absorption leads to the flow of cations into the cell and membrane depolarization. ChR2 can be used to induce high-fidelity spiking patterns in neurons, in some way mimicking endogenous neural activity (Boyden et al. 2005). The archaeal light-driven chloride pump (NpHR) from *Natronomonas pharaonis*, activated by ~590nm yellow light and pumps extracellular chloride ions into the cell, allows temporally precise optical inhibition of neuronal activity, through either knockout of single action potentials or sustained blockade of spiking (Zhang et al. 2007)(Intro\_Figure 7, “manipulation”). Finally, opsins are fused to fluorescent proteins to facilitate their visualization and delivered via a virus that infects broad sets of cells or more specific subpopulations that express the Cre recombinase. Devices to deliver light, like implanted optical fibers, need to aim at the deep target, and experiments are commonly performed at least four weeks after viral delivery.



### **Intro\_Figure7. The toolkit for all-optical interrogation of neural circuits.**

A schematic outline of the diverse elements required for the all-optical approach is shown.

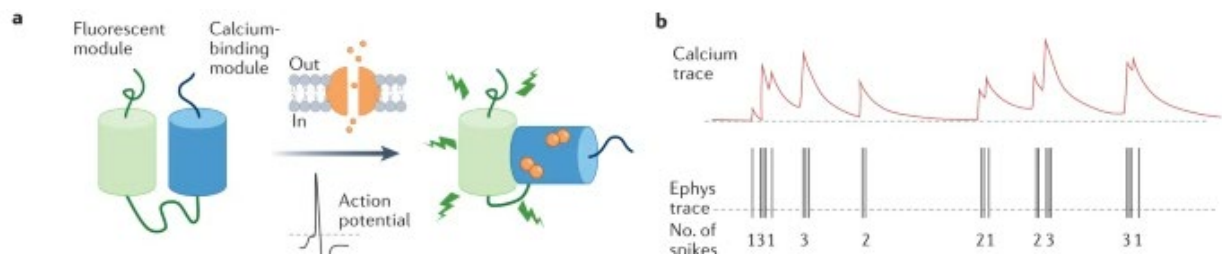
Left bottom showed schematic structure of calcium indicator (Gcamp) and right bottom showed commonly used two optogenetic tools (Halorhodopsin or Channelrhodopsin). When neurons are expressing these light gated molecules, neuronal activity is imaged (recorded) or manipulated. (adapted from (Emiliani et al. 2015 and Mollinedo-Gajate et al., 2019 and Deisseroth, K, 2015))

#### **1.3.4 Observe neural activities of cell types: in vivo Calcium imaging**

Understanding how neurons communicate with each other, requires tools to record neuronal activity. One approach to monitor circuit-specific activity dynamics is optical probing of neural activity, especially, in vivo calcium imaging (Intro\_Figure7, “recording”). During periods of increased neuronal activity, dynamic fluctuation of calcium levels can be monitored with genetically encoded calcium indicators. Neuronal activity causes rapid changes in intracellular free calcium. Calcium imaging experiments rely on this principle to track the activity of neuronal populations (Intro\_Figure8). During increased neuronal activity, the  $\text{Ca}^{2+}$  concentration inside the cell transiently rises. This can be measured by the increased fluorescent signal release by the GCaMP indicator (Intro\_Figure 7, “recording”). Thus, GCaMP fluorescence fluctuations can be used as a proxy for changes in neuronal activity (Emiliani et al., 2015, 2022; Grienberger et al., 2022; Tian et al., 2009).

One of the methods to image calcium in freely moving mice is using mini-epifluorescent microscopes with gradient index (GRIN) lenses (Barretto, Messerschmidt, and Schnitzer 2009; Wu et al. 2021). This tool takes advantage of devices that are small enough to fit on an animal's head and light enough to be carried; moreover, they are capable of recording neuronal activity many millimeters deep within the brain. Mini-epifluorescent microscopes allow repeated measures of somatic calcium activity dynamics of hundreds of genetically and spatially defined neurons in single-cell resolution. Finally, with the help of calcium

imaging techniques, it is possible to give an insight into the endogenous activity of specific neurons during behavior.



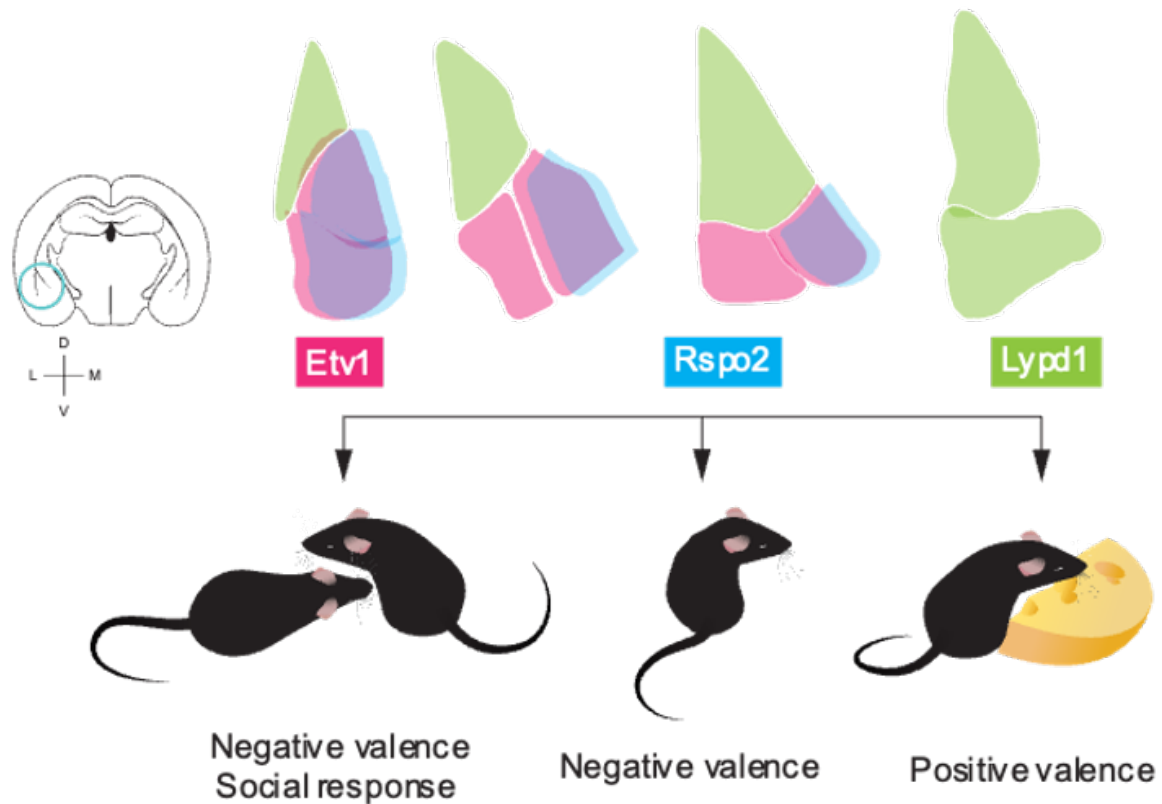
### Intro\_Figure 8. Mechanism of calcium indicator function.

- A. A calcium sensor necessitates both a calcium-binding component and a fluorescent molecule. Genetically encoded calcium indicators (GECIs) are comprised of two proteins: a calcium-binding protein and a fluorescent protein. The firing of an action potential results in the entry of  $\text{Ca}^{2+}$  ions into the cell. The binding of  $\text{Ca}^{2+}$  to the calcium-sensing module induces a structural alteration in the fluorescent molecule, which results in an increase in its luminosity.
- B. Relationship between neural spiking and calcium traces. Owing to limitations in signal-to-noise ratio and temporal resolution, calcium imaging cannot reliably detect individual spikes within trains of action potentials. (Grienberger et al. 2022)



# Thesis summary

To bring evidence to the question of topographical organization of transcriptional cell types in the BLA encoding valence differently as well as the development of the BLA neuronal types, we performed single nucleus RNA-sequencing (snRNA-Seq) on neurons from the BLA at different postnatal time points and used this data to molecularly define neuron types from transcriptomic ‘cell typing’, wherein cells with similar gene-expression properties can be identified and mapped onto higher order structural and functional roles (Cembrowski 2019c; Lein et al. 2017). Furthermore, differentially expressed genes in these cells encompass functionally relevant categories for neurons, including axon guidance and cell adhesion, ligands and receptors, calcium handling, synapses, and transcriptional regulation. Then, to map this variation in space, we used sequential multiplexed in situ hybridization (smFISH), mapping transcriptomic variation onto spatial axes of the BLA. With this, it was found that transcriptional profiling-based correlations were consistent with spatial BLA parcellation. Two of these BLA subpopulations, BLA <sup>Rspo2</sup> or <sup>Lypd1</sup>, innately responded to valence-specific, whereas one, BLA <sup>Etv1</sup>, responded to mixed - aversive and social - cues. Positive-valence BLA neurons promoted normal feeding, while mixed selectivity neurons promoted fear learning and social interactions. These findings enhance our understanding of cell type diversity and spatial organization of the BLA and the role of distinct BLA populations in representing valence-specific and mixed stimuli. Therefore, we uncovered valence specificity among transcriptional and anatomical distinct neuronal types in the BLA (Intro\_Figure 9). Altogether, this study synthesizes transcriptionally defined populations, along with anatomical parcellation of the BLA, with multimodal valence encoding properties in the BLA.



**Intro\_Figure 9. Schematic illustration of anatomy and different valence circuits from transcriptionally identified cell types from our study data.**

Schematic images explaining three different populations in different subregions of BLA (*Etv1*, *Rspo2*, and *Lypd1* neuronal types) for their correspondence to functional roles for valence

# Materials and Methods

## 3.1 Animals

Experiments were performed using juvenile mice (postnatal 10 days and 21days) and adult mice (> 8 weeks). The wild-type animals were from the C57BL/6NRj strain (Janvier Labs - <http://www.janvier-labs.com>). The Rspo2-Cre transgenic line (C57BL/6J-Tg(Rspo2-cre)Blto (RBRC10754)) from RIKEN BioResource Research Center (<https://web.brc.riken.jp>) and Etv1-Cre transgenic line (Etv1tm1.1(cre/ERT2)) from Jackson Laboratory ([www.jax.org/jaxmice](http://www.jax.org/jaxmice)) and Lypd1-Cre (Tg(Lypd1-cre)SE5Gsat/Mmucd) mice were imported from the Mutant Mouse Regional Resource Center (<https://www.mmrrc.org/>). Td-Tomato Rosa26R mouse lines were as described previously (Soriano, 1999), using the line Ai9Isl-tdTomato [B6.Cg-Gt(ROSA)26SorTM9.CAG-tdTomato/Hze/J] (Madisen et al., 2010; Ruff et al., 2021). Transgenic mice were backcrossed with a C57BL/6N background. Animals used for optogenetic manipulations and calcium imaging were handled and singly housed on a 12 h inverted light cycle for at least 5 days before the experiments.

Mice were given ad libitum food access except during food deprivation for feeding experiments. All behavior assays were conducted at a consistent time during the dark period (2 p.m.–7 p.m.). Both male and female mice were used and all the experiments were performed following regulations from the government of Upper Bavaria.

## 3.2 Viral constructs

The following adeno-associated viruses (AAVs) were purchased from the University of North Carolina Vector Core (<https://www.med.unc.edu/genetherapy/vectorcore>): AAV5-ef1a-DIO-eNpHR3.0-mCherry, AAV5-ef1a-DIO-mCherry, AAV5-Ef1 $\alpha$ -DIO-hChR2(H134R)-EYFP, AAV5-Ef1a-DIO-eYFP, AAV5.Syn.Flex.GCaMP6f.WPRE.SV40 virus was obtained from Addgene (<http://www.addgene.org/>).

### **3.3 Single nucleus RNA sequencing**

#### **3.3.1 Preparation**

Single-nucleus RNA sequencing was focused on the basolateral amygdala (BLA). For visually guided dissection of the BLA, we practiced by using the fluorescent expression in basal amygdala (BA) of *Rspo2-cre; tdTomato* mice (J. Kim et al. 2016) and dense fiber tracks surrounding BLA boundaries to facilitate complete microdissection of BLA. Each single nucleus sequencing dataset includes BLA tissues from 4 male brains (both hemispheres). To reduce potential batch effects, brains were always from the same litter, collected and processed in parallel at the same time.

Mice were deeply anesthetized by i.p. injections of 200 mg/kg Ketamine and 40 mg/kg Xylazine, and perfused with 10 mL ice-cold Sucrose-HEPES Cutting Buffer” containing (in mM) 110 NaCl, 2.5 KCl, 10 HEPES, 7.5 MgCl<sub>2</sub>, and 25 glucose, 75 sucrose (~350 mOsm/kg), pH=7.4 (Saunders et al. 2018). All the solutions/reagents were kept on ice in the following procedures unless otherwise specified. The brain was extracted and cut (300 µm) on a vibratome (Leica VT1000S, Germany) in cutting buffer, and the slices were transferred into a Dissociation Buffer containing (in mM): 82 Na<sub>2</sub>SO<sub>4</sub>, 30 K<sub>2</sub>SO<sub>4</sub>, 10 HEPES, 10 glucose and 5 MgCl<sub>2</sub>, pH=7.4 (Saunders et al. 2018). BLA was microdissected under a microscope (Olympus SZX10) covering the anterior (Bregma -0.59) and posterior (Bregma -3.0) for adult BLA and the anterior (Bregma -0.8) and posterior (Bregma -2.8) for juvenile BLA.

#### **3.3.2 Single nucleus isolation and library preparation**

The protocol for single nucleus isolation was optimized from previous studies (Mathys et al., 2019; Matson KJE, 2018) and demonstrated nucleus isolation protocol (CG000393, 10x Genomics). In brief, collected tissue chunks from the four brains were transferred in 600 µL homogenization buffer containing 320 mM sucrose, 5 mM CaCl<sub>2</sub>, 3 mM Mg(CH<sub>3</sub>COO)<sub>2</sub>, 10 mM Tris HCl pH 7.8, 0.1 mM EDTA pH 8.0, 0.1% NP-40 (70% in H<sub>2</sub>O, Sigma NP40S), 1 mM β-mercaptoethanol, and 0.4 U/µL SUPERase RNase inhibitor (Invitrogen AM2694). The homogenization was performed in a 1mL Wheaton Dounce tissue grinder with 20

strokes of loose and then 20 strokes of a tight pestle. The homogenized tissue was filtered through a 20- $\mu$ m cell strainer (Miltenyi Biotec) and mixed with an equal volume of working solution containing 50% OptiPrep density gradient medium (Sigma-Aldrich), 5 mM  $\text{CaCl}_2$ , 3 mM  $\text{Mg}(\text{CH}_3\text{COO})_2$ , 10 mM Tris HCl pH 7.8, 0.1 mM EDTA pH 8.0, and 1 mM  $\beta$ -mercaptoethanol. The resulting solution was transferred into a 2 mL centrifuge tube. A 29% OptiPrep density gradient solution including 134 mM sucrose, 5 mM  $\text{CaCl}_2$ , 3 mM  $\text{Mg}(\text{CH}_3\text{COO})_2$ , 10 mM Tris HCl pH 7.8, 0.1 mM EDTA pH 8.0, 1 mM  $\beta$ -mercaptoethanol, 0.04% NP-40, and 0.17 U/ $\mu$ L SUPERase inhibitor was slowly placed underneath the homogenized solution through a syringe with a 20G needle. In the same way, a 35% Density solution containing 96 mM sucrose, 5 mM  $\text{CaCl}_2$ , 3 mM  $\text{Mg}(\text{CH}_3\text{COO})_2$ , 10 mM Tris HCl pH 7.8, 0.1 mM EDTA pH 8.0, 1 mM  $\beta$ -mercaptoethanol, 0.03% NP-40, and 0.12 U/ $\mu$ L SUPERase inhibitor was slowly laid below the 30% density. The nucleus were separated by ultracentrifugation using an SH 3000 rotor (20 min, 3000xg, 4 °C). A total of 300  $\mu$ L of nucleus was collected from the 29%/35% interphase and washed once with 2 mL resuspension solution containing 0.3% BSA and 0.2 U/ $\mu$ L SUPERase in PBS. The nucleus were centrifuged at 300g for 5 min and resuspended in ~30  $\mu$ L resuspension solution.

The nucleus was stained with DAPI and counted. After manually determining the cell concentration using a hemocytometer, suspensions were further diluted to desired concentrations (300–700 cells/uL) if necessary. The appropriate final suspension targeted 5000 cells recovered, and loaded into the chip. Nanoliter-scale Gel Beads-in-emulsion (GEMs) generation, barcoding, cDNA amplification, and library preparation were done using the Chromium Next GEM Single Cell 3' Reagent Kits v3.1 according to the manufacturer's protocol.

### **3.3.3 snRNA-Seq analysis**

Prepared libraries were sequenced on Illumina NextSeq 500 (Mid and High Output Kit v2.5, Paired-end sequencing, 28bp-130bp). We used cellranger (version 7.0.1) to extract fastq files, align the reads to the mouse genome (10x genomics reference build MM10 2020 A), and obtain per-gene read counts. Subsequent data processing was performed in R using Seurat (version 4.1.3) with default parameters if not indicated otherwise. After merging the data, we normalized the data (normalization.method='LogNormalize', scale.factor=10000), detected variable features (selection.method='vst', nfeatures=2000), and scaled the data

(vars.to.regress=c('nCount\_RNA')) . We then applied quality control filters on cells with the following criteria: a) more than 200 genes detected b) less than 20% mitochondrial genes reads c) more than 5% ribosomal protein genes reads d) less than 0.2% hemoglobin genes reads e) singlets as determined by doubletFinder (version 2.0.3, pK = 0.09, PCs=1:10). Only genes detected in at least 4 cells were kept. The resulting dataset consisted of 7,953 cells and 21,557 genes.

Initial cell clustering was performed with resolution 0.4 after applying harmony batch correction (version 0.1.1) and subsequent UMAP embedding on the harmony reduction.

## Global annotation

For global annotation, non-neuronal clusters were identified by expression of non-neuronal markers (e.g., *Plp*, *Mbp*, *Pdgfra*, *Olig*, *Lhfp13*, *Igfbp7*, *Bsg*, *Tmem119*, *Cst3*, *P2ry12*, *Hexb*, *C1qb*, *C1qa*, *Aldh1l1*, *Gfap*, *Slc1a2*, *Cfap299*) and absence of neuronal markers (*Snap25*, *Slc17a7*, *Slc17a6*, *Neurod6*, *Syp*, *Tubb3*, *Map1b*, *Elavl2*, *Gad1*, *Gad2*, etc.). Neuronal clusters were confirmed by the expression of neuronal markers above and neurotransmitter and neuromodulator-releasing neurons were annotated by well-known markers (glutamatergic neurons: *Slc17a7*, *Slc17a6*, *Camk2a*, *Gria2*, GABAergic neurons: *Adora2a*, *Gad1*, *Gad2*, *Gabbr1*, *Gabbr1*, *Gad65*, *Gad67*)

For annotation on GABAergic neurons in BLA, firstly only GABAergic neurons based on above global annotation were subtracted and re-clustered. Next, conventional markers from a previous study (Beyeler and Dabrowska 2020a) were used (*Reln*, *Ndnf*, *Sst*, *Pvalb*, *Vip*, *Cck*, *Calb1*, *Crh*, *Npy*, *Foxp2*, *Htr2a*). Also, GABAergic neuron markers for the central amygdala (CEA) (Kim et al. 2017) were used as reference (*Prkcd*, *Ppp1r1b*, *Tac2*, *Wfs1*, *Dlk1*, *Penk*, *Drd2*, *Drd1*, *Calcr1*, *Pdyn*, *Nts*, *Tac1*). we sorted out BLA local inhibitory interneuron from neighborhood regions (e.g., projecting inhibitory neurons in the central amygdala (CeA, based on *Pkcd*, *Drd1*, and *Drd2*) (Beyeler and Dabrowska 2020a; Kim et al. 2017) or intercalated cells (ITCs, based on *Foxp2* expression) or the amygdalostratial area (based on *Rarb* expression) (Kuerbitz et al. 2018; Rataj-Baniowska et al. 2015).

For clarity, we unified the naming of cell populations in the diverse conditions as follows: clusters from unsupervised clustering were named “Clusters”, cell populations containing multiple clusters were named “Category”

### **Marker-gene selection for glutamatergic neurons for spatial validation (smFISH)**

To annotate subtypes of glutamatergic neurons in BLA we retained only glutamatergic neurons and subjected them to re-clustering. Initially, marker genes were identified using `presto::top_markers` ( $n = 5$ ,  $auc\_min = 0.5$ ,  $pct\_in\_min = 20$ ,  $pct\_out\_max = 20$ ). We then handpicked the most specific gene for each cluster. For clusters where no marker could be pinpointed, we turned to in situ hybridization (ISH) data from Allen brain atlas: mouse brain (<https://mouse.brain-map.org/>). Preference was given to genes that exhibited higher expression in the BLA than other regions and showed localized expression within BLA subregions. Based on these criteria, we selected 10 marker genes shown in Figure 1F. It's worth noting that other combinations of genes might also adequately represent these molecularly defined cell types.

### **Construction of Phylogenetic tree of glutamatergic neurons**

Cell type tree was calculated by `Seurat::BuildClusterTree` on the aggregated expression of all genes using hierarchical clustering of the distance matrix by using Euclidean distance.

### **Gene ontology (GO) enrichment**

We first identified marker genes for the clusters using `Seurat::FindAllMarkers` (default parameters). For Hypergeometric enrichment testing we then used `hyperGTest` in library `GOSstats` (version 2.62) with all genes in our scRNA dataset serving as background and the respective marker genes as foreground.

### **Comparison with published BLA data**

Mouse BLA data: <https://doi.org/10.6084/m9.figshare.c.5108165> from (O’Leary et al. 2020)

We obtained expression matrices for data set GSE148866 from GEO and cell annotation from (O'Leary et al. 2020b) and constructed a Seurat object. Normalization, scaling and UMAP embedding was performed as described above. We integrated the data with our own using Seurat::IntegrateData after selecting and subsequently finding integration anchors. Cell-to-cell mapping was performed using scmap (1.18.0) as described in [https://biocellgen-public.svi.edu.au/mig\\_2019\\_scrnaseq-workshop/comparing-and-combining-scrna-seq-datasets.html](https://biocellgen-public.svi.edu.au/mig_2019_scrnaseq-workshop/comparing-and-combining-scrna-seq-datasets.html) after splitting the Seurat object in two SingleCellExperiment objects.

### **3.3.4 Marker-gene selection for glutamatergic neurons for spatial validation (smFISH)**

Unlike to GABAergic neurons, there are not many conventional markers for glutamatergic neuron of BLA, to annotate subtypes of glutamatergic neurons in BLA, only glutamatergic neurons were remained and re-clustered. Then, we performed differential expression (DE) analysis for each of the clusters by using the 'FindAllMarkers' function and then we applied a series of selection criteria designed to allow classification of a maximum number of unique cell types using the fewest number of genes possible. As such, the expression pattern of the top 30 DE genes were listed and limiting our search to genes with an adjusted p-value cutoff of at least 0.05 and an average log-fold change of 0.55 or over. However, some genes still showed global expression across clusters. we also specifically selected markers as close to binary "on/off" expression patterns with FindMarkers with "FindMarkers" in one specific cluster from others, based on high percentage of marker positive cells in the target population compared to low percentage of marker positive cells outside the target population. This inspection on each candidate gene expression facilitated to find in possible, the most specific gene for one cluster as its marker. The selected marker genes are listed and shown in Figure 4.3E. However, several clusters could not be identified by a gene, in which case in situ hybridization (ISH) data from Allen brain atlas: mouse brain (<https://mouse.brain-map.org/>) were preferentially used to select a representative marker to be used in biological spatial analysis. In this case, only genes showing higher gene expression in BLA compared to other regions and localized expression in subregion of BLA were in priority selected. With this criteria Finally, a total of 10 marker genes were chosen and we note that this is not the only combination of genes that could feasibly serve to represent these molecularly defined cell types.



## 3.4 Hairpin chain reaction (HCR) sequential multi-fluorescent in situ hybridization

### 3.4.1 Preparation and imaging

C57BL/6J mice (n = 6, 3 male, 3 female, > 8 weeks) were anesthetized IP with a mix of ketamine/xylazine (100 mg/kg and 16 mg/kg, respectively) (Medistar and Serumwerk) and transcardially perfused with ice-cold phosphate-buffered saline (PBS), followed by 4% paraformaldehyde (PFA) (1004005, Merck) (w/v) in PBS. The brain was dissected and immediately placed in a 4% PFA buffer for 2 h at room temperature. The brain was then immersed in 30% RNase-free Sucrose (Amresco, 0335) in 1X PBS for 48 h at 4 degree until the brain sank to the bottom of the tube. The brain was then embedded in OCT and cryo-sectioned (15 mm thick) by harvesting coronal sections through the AP extent of BLA and stored at -80°C. At least three coronal section were selected for analysis within each of the anterior (-0.79 to -1.07 from bregma), anterior-middle (-1.23 to -1.55 from bregma), posterior-middle (-1.67 to -2.03 from bregma) and posterior (-2.15 to -2.45 from bregma) regions of the BLA.

The selected ten genes were targeted in four sequential HCR rounds. The probe sets (Molecular Instruments) were used as follows: Sema5a, Grik1, Rorb (Round 1); Adamts2, Bdnf (Round 2); Cdh13, Otof (Round 3); Lypd1, Etv1, Rspo2 (Round4). At all rounds Rnu6 probe was applied together to be use as a marker for nucleus. In order to avoid biased expression level from round order, round order was mixed. Sections were processed according to the sequential hybridization chain reaction (HCR) protocol from a previous paper (Rossi et al. 2021). In brief, sections were fixed in 4% PFA at 4°C, dehydrated in serial ethanol washes, and treated with RNAscope Protease IV (ACDBio). Sections were then rinsed and hybridized overnight at 37°C with probes targeting the first gene set. Sections were then washed, and probes were amplified with fluorophores (Alexa 405,488, 546, and 647) overnight at room temperature. Next, sections were washed, and autofluorescence was quenched using a Vector TrueVIEW Autofluorescence Quenching kit (Vector labs cat# SP-8400). Slides were cover-slipped with Prolong Gold antifade Mounting Medium (Invitrogen) and allowed to cure at RT for 2 hours before imaging. After each round imaging, coverslips were removed, and sections were washed to remove mounting medium.

The probes were then digested with DNase I (Sigma cat# 4716728001), and the next probe set was hybridized. Images were acquired with a Leica SP8 confocal microscope and a 20×/0.75 IMM objective (Leica).

### **3.4.2 Data analysis for HCR**

#### **Spatial organization in the BLA**

Firstly, four images from 4 rounds were superimposed by landmark and serial strain registration. Also, cell segmentation (based on Rnu6 expression) and thresholding fluorescence for positive cell per each gene were performed and quantification for cells expressing a given gene was also analyzed by HALO software (Indica Labs). Thresholding required to classify a given gene positive/negative cell was chosen based on visual inspection but double-blind way. Next, we referred to a recent anatomy paper 12 for subregion delineation and coronal section selection of BLA. In order to represent whole BLA, dataset constituted four coronal sections (anterior, anterior middle, posterior middle and posterior) and eight subregions (aLA, pLA, amBA, alBA, acBA, pBA, ppBA, ppLA). To visualize gene expression, positive cells were reconstructed and plotted in dot colorized by gene. Finally, percentage of positive cells for each gene was calculated within individual eight sub-regions. We did not separate multiple gene positive cells. Therefore, the sum of percentage per subregion are more than 100%. Last, we compared this percentage across coronal section as well as across subregions in Figure 2. Pearson's cross-correlation and clustering analysis was computed between BLA subregions and the average of each percentage per gene. Density heatmap was plotted in the in a color-scale (red = 1 and blue = 0, normalized value by the highest density area (=1)). To map smFISH and snRNA-seq data correlation, we computed pairwise Pearson correlation with hierarchical clustering of 10 marker gene expression across all glutamatergic neurons (snRNA data) and of average percentage of 10 marker gene positive cell across eight sub regions of BLA (smFISH).

#### **smFISH PCA clustering analysis**

Data including x,y position of positive cell expressing each gene were then imported to a Python workflow in which unsupervised Principal component analysis (PCA) were simply customized from the pipeline described before (Wang et al. 2021). In brief, Images

containing expression patterns of 10 marker-genes were decomposed into principal components (PCs). The eigen-images from the top 4 PCs explained on average  $80.8 \pm 5.16\%$  of variance in each sample. PCA of the expression patterns of 10 marker-genes were reconstructed and used to identify spatial patterns in BLA orientation. As the pattern demarcating BLA by each PC component across different samples was homogeneous, we only selected samples with this homogenous pattern of PCA to make populational analysis. Therefore, PC loading values for each gene were averaged by different coronal sections (total 16 PC variance, e.g., anterior PC1, anterior PC2 or Anterior-middle PC1, Anterior-middle PC2 etc) and clustered by Pearson's correlation across genes. Therefore, this was compared with the clusters from percentages of 10 marker genes positive cells in eight subregions of BLA in supervised manner.

### **Correlation between smFISH and snRNA clusters**

For mapping clusters of single cell transcriptomic data to smFISH signals and corresponding locations, we first aggregated the single cells read counts for each cluster for each gene that was used in smFISH (Fig.S6). We then correlated (Pearson) the smFISH expression data — normalized z-scores of 10 marker genes in a of radius  $50 \mu\text{m}$  10 — with each cluster expression pattern and assigned each smFISH cell to one of the 11 clusters according to the highest correlation coefficient.

## **3.5 Stereotaxic surgeries**

Mice were anesthetized for surgery with isoflurane (1.5–2%) and placed in a stereotaxic frame (Kopf Instruments). Body temperature was maintained with a heating pad. A systemic anesthetic (carprofen 5 mg/kg bodyweight) was administered. Mice used in in vitro and in vivo optogenetic were bilaterally injected with 0.4  $\mu\text{l}$  of optogenetic or control virus in the BLA by using the following coordinates calculated with respect to the bregma:  $-1.8 \text{ mm}$  anteroposterior,  $\pm 3.25 \text{ mm}$  lateral,  $-4.75 \text{ mm}$  ventral for *Lypd1*-Cre mice, bregma:  $-1.5 \text{ mm}$  anteroposterior,  $\pm 3.25 \text{ mm}$  lateral,  $-4.8 \text{ mm}$  ventral for *Rspo2* and *Etv*-Cre mice. In the same surgery, mice used in optogenetic experiments were bilaterally implanted with optic fibers (200- $\mu\text{m}$  core, 0.5 NA, 1.25-mm ferrule (Thorlabs)) above the BLA ( $-4.6 \text{ mm}$  ventral). Implants were secured with cyanoacrylic glue, and the exposed skull was covered with dental acrylic (Paladur). Mice used in in vivo calcium imaging experiments were injected in

the right BLA (coordinates as above) with 0.4  $\mu$ l AAV-GCaMP6f virus. One week later, the microendoscope was implanted. To do so, a 0.8-mm hole was drilled in the skull above the BLA. Debris was removed from the hole, and a sterile 20-gauge needle was slowly lowered into the brain to a depth of  $-4.8$  mm from the cortical surface to clear a path for the lens. The GRIN lens (GLP-0673; diameter, 0.6 mm; length,  $\sim 7.3$  mm, Inscopix) was slowly lowered into the brain to  $-4.75$  mm from the bregma by using a custom lens holder. The lens was secured in place with glue (Loctite 4305) and dental cement (Paladur). The exposed top of the lens was protected by a covering of a silicone adhesive (Kwik-cast). Approximately, four weeks after the lens implantation, the mice were assessed for observable GCaMP6 fluorescence. The heads of the mice were fixed, and the top of the lens was cleaned of debris. The miniature microscope (Inscopix) with a baseplate (BLP-2, Inscopix) was positioned above the lens such that GCaMP6 fluorescence and neural dynamics were observed. The mice were anesthetized with isoflurane, and the baseplate was secured with dental cement (Vertise Flow). A baseplate cap (BCP-2, Inscopix) was left in place until imaging experiments. Expression in *Etv1-CreER* animals was induced by intraperitoneal injections of tamoxifen (150-200  $\mu$ l, 10 mg/ml, dissolved in 90% corn oil and 10% ethanol) on 4 consecutive days in the modified way as described (Abs et al., 2018). We found for mouse recovery the injection started 2 days after surgery.

### **3.6 Acute brain slice preparation and electrophysiological recordings**

The animals were anesthetized with isoflurane and decapitated under deep anesthesia. The brain was immediately immersed in an ice-cold cutting solution consisting of NaCl (30 mM), KCl (4.5 mM),  $MgCl_2$  (1 mM),  $NaHCO_3$  (26 mM),  $NaH_2PO_4$  (1.2 mM), glucose (10 mM), and sucrose (194 mM), equilibrated with a 95%  $O_2$ /5%  $CO_2$  gas mixture. The brain was sectioned into slices of 280  $\mu$ m thickness using a Leica VT1000S vibratome and transferred to an artificial cerebrospinal fluid (aCSF) solution containing NaCl (124 mM), KCl (4.5 mM),  $MgCl_2$  (1 mM),  $NaHCO_3$  (26 mM),  $NaH_2PO_4$  (1.2 mM), glucose (10 mM), and  $CaCl_2$  (2 mM), equilibrated with 95%  $O_2$ /5%  $CO_2$  gas mixture and maintained at 30-32°C for 1 hour before being returned to room temperature.

The brain slices were mounted in a recording chamber and perfused continuously with the aforementioned aCSF solution equilibrated with 95%  $O_2$ /5%  $CO_2$  gas mixture at 30-32°C.

Whole-cell patch-clamp recordings were performed using patch pipettes prepared from filament-containing borosilicate micropipettes with a resistance of 5-7 MΩ. The intracellular solution used for recordings contained potassium gluconate (130 mM), KCl (10 mM), MgCl<sub>2</sub> (2 mM), HEPES (10 mM), Na-ATP (2 mM), Na<sub>2</sub>GTP (0.2 mM) and had an Aosmolality of 290 mOsm. The brain slices were visualized using an IR-DIC equipped fluorescence microscope (Olympus BX51) and data were acquired using a MultiClamp 700B amplifier, a Digidata 1550 digitizer, and analyzed using the Clampex 10.3 and Clampfit software from Molecular Devices. The data were sampled at 10 kHz and filtered at 2 kHz.

### **3.7 Behavior paradigms**

All mice were handled and habituated on the behavioral chamber for 4-5 days before experiments. For optogenetic experiments, mice were tethered to the optic-fiber patch cords and habituated to the context for 15 min daily. For calcium imaging experiments, dummy mini-scope and cable (Inscopix) were fixed on the head of mice and habituated to the context for 20-30min daily. The behavior arenas were housed inside a soundproof chamber equipment with houselights and video cameras (c920 webcam, Logitech).

#### **3.7.1 Feeding experiments**

Food restricted mice were placed in an empty home cage and in one corner was placed a pellet fixed-plastic container. Mice were accessible to food for 10min per day during 2 days. For optogenetic experiment, mice received the light for whole 10min in one day and another day without light. Also, the light on-off order was psedo-randomized within a cohort group to reduce any effect from order of light on. After 10min the remaining food was weighed. The session was video recorded, and feeding behaviors (e.g., frequency to food container or cumulative time in food container) were also analyzed by EthoVision XT 16.0 video tracking software (Noldus). For calcium imaging experiment, same as above but for 15min mice were placed.

#### **3.7.2 Social interaction test**

Three-chamber test was performed as previously described (S. Kim et al. 2016) but in order to combine with optogenetic and calcium imaging experiments, no door was equipped.

In brief, the stranger mice, younger than test mice but same gender, were handled for 3 min and then habituated in a wire cage placed in the 3-chamber apparatus for 5–10 min for 4 consecutive days before starting experiment. The test mouse was located to the center chamber. A wired cup with a stranger mouse and an empty cup was introduced into the other two chambers and sociability test started. The movement of the test mouse was tracked for 15 min (EthoVision XT 16.0) for calcium imaging. For optogenetic experiment, 2 days (One day with light and another day without light but pseudo-randomized order of light on-off day within a cohort group) were examined and stranger mice changed every day. Therefore, sociability was analyzed using cumulative time/frequency in social zone or for social interaction. For each set of experiments, the orientation of the two wired cups containing stranger or empty was counter-balanced.

For several calcium imaging cases to precisely analyze the comprehensive social behaviors of mice, we use Round Social Arena as described previously (S. Kim et al. 2016) or two chamber social assay instead of three chambers. In brief, round-shaped arena (inner diameter: 49 cm, height: 45 cm) with one 3d-printed transparent bar cage (diameter: 8cm, height: 10.5 cm) at the center of the arena. The inner cage was topped with a cone-shaped 3d-printed roof to prevent the test mouse from climbing up. Inside the cone roof, a wide-angle (180°) fish-eye lens camera was installed to provide a close-up view of animals' social interactions. Above the arena, a camera at the ceiling was used to track animal's positions and speed. So micro-social behaviors such as exact time point of starting of social interaction or sniffing were measured manually through a wide-angle fish eye camera as well as automatic tracking by EthoVision XT 16.0 from ceiling camera.

### **3.7.3 Contextual fear conditioning (cFC)**

Main cFC paradigm was modified from a previous study (J. Kim et al. 2016). On day 1, mice were placed in to a contextual fear conditioning chamber (Med Associates) while bilaterally connected to optic fiber cables received three foot-shocks (0.75 mA for 2 sec) at the 198-s, 278-s and 358-s time points. For optical activation experiments, simultaneously with the footshocks at the 198-s, 278-s and 358-s time points, a 10-s, 20-Hz train of 15-ms pulses of 473-nm (10–15 mW) light was used for photostimulation but constant of 620-nm (10mW) for photoinhibition. On day 2, mice were connected to optic fiber patch cables and

placed in the fear conditioning chamber for 180 s, where no shock or laser was delivered. Freezing was detected by using ANY-maze 7.1 (Stoelting).

### **Analysis of freezing behavior**

Freezing behavior, defined as complete immobility with the exception of breathing, was used as a proxy of fear response. Freezing was automatically quantified using the software ANYmaze (Stoelting) as described in a previous paper (Klein et al. 2021) . In brief, the software calculated a “freezing score” depending on the number of pixel changes between frames. If the freezing score fell below an empirically determined threshold for at least 2 s, mice were considered to be freezing. To exclude errors where resting was incorrectly detected as freezing behavior, manually freezing behaviors were verified. Animals were excluded from further analysis if they did not show any freezing behavior upon fear conditioning in a recall session.

### **3.7.4 Optogenetic conditional place preference(avoidance) test.**

Conditioned place preference (CPP) was carried out essentially as previously described (Ponserre et al., 2022). It was conducted in a custom-built arena made of two chambers: a rectangular-shaped 2 chambers (45 \* 15 cm); one compartment consisted of white walls and a metal floor with circular holes, the another had red walls and square holes.

For the optogenetic experiments, on pretest day (day1) optic cable tethered mice were freely exploring the chambers without light for 10min after 5min of habituation. Based on total time in each chamber, preferred chamber was confirmed on that day. For optogenetic activation by Chr2, preference was measured for Lypd1-Cre, but avoidance was measure for Etv1-Cre and Rspo2-Cre mice. Therefore, a preferred chamber was paired with light for Rspo2 and Etv1 Cre mice but a no-preferred chamber was paired with light for Lypd1 Cre mice for three consecutive conditioning days (day2-4). During conditioning days mice were constrained in a paired chamber with light for 15min and another chamber without light for 15min. On post-test day (day5) mice were freely exploring the chambers without light as same as pre-test(day1). The time each animal spent in each chamber and their locomotor activity (distance travelled) was recorded using EthoVision XT 16.0 (Noldus) tracking software. The preference index was calculated by (duration in the paired chamber) – (duration in the non-paired chamber).

### **3.7.5 Open field task (OFT)**

OFT was carried out essentially as previously described ((Felix-Ortiz et al. 2013a). In brief, four 3 min epochs beginning with a light-off (OFF) baseline epoch, followed by a light-on (ON) illumination epoch in total a single 12min session. For analysis first off and last on were excluded in order to avoid novelty or satiation driven factors.

## **3.8 Optogenetic manipulations**

Mice were bilaterally tied to optic-fiber patch cords (Plexon Inc) connected to a 465-nm LED (for Chr2) via Optogenetic LED module (Plexon Inc) and mating sleeve (Thorlabs). Photostimulation was performed using 10 ms, 463 nm light pulses at 20 Hz and 10 mW. Photoinhibition used constant 620nm light at 10 mW. The LED was triggered, and pulses were controlled PlexBright 4 Channel Optogenetic Controller by with Radiant Software (Plexon Inc)

## **3.9 In vivo Ca<sup>2+</sup> imaging of freely moving mice**

### **3.9.1 Imaging**

Ca<sup>2+</sup> videos were recorded using nVista acquisition software (Inscopix, Palo Alto, CA). To later account for any lag between the onset of behavior and Ca<sup>2+</sup> movies, a continuous train of TTL pulses was sent from Ethovision XT 16.0 or ANY-maze 7.1 (Stoelting) to nVista acquisition software at 1 Hz and a 50% duty cycle for the duration of the session for running synchronization of the two datasets. Ca<sup>2+</sup> videos were acquired at 15 frames per second with an automatic exposure length. An optimal LED power was selected for each mouse to optimize the dynamic range of pixel values in the field of view, and the same LED settings were used for each mouse throughout the series of imaging sessions.



### 3.9.2 Preprocessing

Ca<sup>2+</sup> videos were recorded using nVista acquisition software (Inscopix, Palo Alto, CA). To later account for any lag between the onset of behavior and Ca<sup>2+</sup> movies, a continuous train of TTL pulses was sent from Ethovision XT 16.0 or ANY-maze 7.1 (Stoelting) to nVista acquisition software at 1 Hz and a 50% duty cycle for the duration of the session to synchronize the extracted behavior statistics with calcium traces. The TTL emission-reception delay is negligible (less than 30ms), therefore the behavioral statistics time series can be synchronized with calcium traces by the emission/receival time on both devices, using a custom python script. Ca<sup>2+</sup> videos were acquired at 15 frames per second with an automatic exposure length. An optimal LED power was selected for each mouse to optimize the dynamic range of pixel values in the field of view, and the same LED settings were used for each mouse throughout the series of imaging sessions. We used the IDPS (Inscopix data processing software, version 1.8.0) for the acquisition of calcium image data, rigid motion correction, automatic selection of neuro somata as the regions of interests (ROIs), and extraction of raw calcium traces by using option, Cnmfe in IDPS and visual inspection with their tracing and morphology. To prevent potential biases resulting from temporal convolution in the calcium traces, we performed spike deconvolution using the OASIS algorithm implemented in Suite2p 19The inferred spike trains were used in the following social and food preference experiment analyses.

### 3.9.3 Calcium data analysis for Food and Social assay and fear conditioning

The relative distance between the recorded mice and food or other mice are closely related with food consumption and social behavior respectively. Therefore, we computed this relative distance for each calcium frame recorded in the food consumption or social behavior experiments. This relative distance was then normalized by the radius of the experiment chamber size.

To inspect the correlation between neuron firing rate and the relative distance to food or other animals, we discretized the relative distances into (31 bins), and we computed the averaged spike firing rate of the frames whose relative distances fall into the same distance bin. The preferred relative distance of each neuron was determined as the distance bin with

the highest averaged firing rate. The neurons were classified into difference valence-correlated categories based on their preferred distance to food / other animals.

## **Permutation test**

In order to confirm that neuronal activities related to specific contexts (Food and social assay) beyond chance level (null hypothesis), we circularly shuffled the inferred spike train for each neuron with a random time offset for 1000 times. For each shuffled spike train, we computed the null distance distribution by calculating the averaged firing rate for each distance bin. we selected 5% top of the null distribution and then among them, the distribution was performed and again 5% top of this distribution was selected. If the maximum average firing rate of the distance distribution of a neuron is higher than 95% of the null distribution, then the neuron is considered significantly tuned to distance to food/social object.

## **Significant neurons for social / food assay**

To determine if the difference of the percentage of pro/anti food/social neurons between Lypd1, Etv1 and Rspo2 neuron population are significant, we pooled the neurons from the 3 population. For each neural population, we randomly selected N neurons from the pool distribution and compute the percentage of pro/anti food/social neurons for 1000 times to obtain a null percentage distribution (N equals to the number of neurons for the testing neural population). We then compared the percentage of the testing population with the two tails of the null percentage distribution and determined the significance at the 2.5% significance level.

## **Fear conditioning calcium data analysis**

The freezing behaviors are detected automatically by ANY-maze 7.1 (Stoelting) with the 2-second minimum duration. To determine the correlation between neural activities and foot shock/freezing behavior in the fear conditioning experiment, we computed the score for foot shock as follows:

Foot shock response score=  $(F_{\text{(during shock on)}} - F_{\text{(off before shock)}}) / (F_{\text{(during shock on)}} + F_{\text{(off before shock)}})$

Similarly, the freezing score was computed as:

$$\text{Freezing score} = (F_{\text{freezing}} - F_{\text{(non-freezing)}}) / (F_{\text{freezing}} + F_{\text{(non-freezing)}})$$

Fshock on and Ffreezing are the averaged firing rate in the 2 seconds before and during the onset of foot shock or freezing events respectively.

The neurons positively correlated with foot shock events might be involved in the negative valence event representation. To investigate this, we computed the percentage of foot-shock correlated neurons in the fear-acquisition session and the freezing frequency in the fear retrieval session for each mouse. The mice did have both two sessions included. We performed the linear regression on these two statistics for quantitative descriptions of the relationships between these two statistics.

### **Classification for footshock-responsive neurons**

In order to classify positive footshock-responsive neurons (pro-footshock) or negative footshock-responsive neurons (anti-footshock) , we circularly shuffled the inferred spike train for each neuron with a random time offset for 1000 times. Then we computed the mean response score to fear stimulus for each shuffled spike train in the same way as described above in order to obtain a null response score distribution. The neuron whose mean response score are higher than the top 2.5% of the null distribution are considered as pro-footshock neurons whose activities are positively correlated with footshock event. Vice versa, the neurons with response score lower than the bottom 2.5% of the null distribution are considered as anti-footshock neurons.

## **3.10 Histology**

Animals were anesthetized IP with a mix of ketamine/xylazine (100 mg/kg and 16 mg/kg, respectively) (Medistar and Serumwerk) and transcardially perfused with ice-cold phosphate-buffered saline (PBS), followed by 4% paraformaldehyde (PFA) (1004005, Merck) (w/v) in PBS. Brains were postfixed at 4 °C in 4% PFA (w/v) in PBS overnight, embedded in 4% agarose (#01280, Biomol) (w/v) in PBS, and sliced (50-100 µm) using a Vibratome (VT1000S – Leica). Epifluorescence images were obtained with an upright epifluorescence microscope (Zeiss) with 10× or 5x/0.3 objectives (Zeiss). To acquire Fluorescence z-stack images, a Leica SP8 confocal microscope equipped with a 20×/0.75

IMM objective (Leica) was used. For full views of the brain slices, a tile scan and automated mosaic merge functions of Leica LAS AF software were used. Images were minimally processed with ImageJ software (NIH) to adjust for brightness and contrast for optimal representation of the data, always keeping the same levels of modifications between control and treated animals. To acquire Fluorescence z-stack images, a Leica SP8 confocal microscope equipped with a 20×/0.75 IMM objective (Leica) was used. For full views of the brain slices, a tile scan and automated mosaic merge functions of Leica LAS AF software were used. Images were minimally processed with ImageJ software (NIH) to adjust for brightness and contrast for optimal representation of the data, always keeping the same levels of modifications between control and experimental animals.

### **3.11 Immunohistochemistry**

For recovery of neurobiotin-filled neurons after whole-cell recordings, acute brain slices were fixed in 4% PFA at room temperature for 30–45 min. Fixed slices were kept in 0.1 M PB (80 mM  $\text{Na}_2\text{HPO}_4$  and 20 mM  $\text{NaH}_2\text{PO}_4$ ) until being processed for immunohistochemistry as described above. Slices were then washed in 0.1 M PB and incubated with fluorophore-conjugated streptavidin (1:2,000) (Jackson) diluted in 0.05 M TBS with 0.5% Triton X-100 overnight. The next day, slices were washed in 0.1 M PB and mounted with RapiClear (SunJin Lab Co). Slices were imaged 1 d later.

### **3.12 Data Analysis (statistics)**

Data and statistical analyses were performed using Prism v5 (GraphPad, USA) and Excel 2016 (Microsoft, USA). Clampfit software (Molecular Devices, USA) was used to analyze electrophysiological recordings and all statistics are indicated in the figure legends. T-tests or Ordinary one-way ANOVA with Tukey's multiple comparisons test or two-way ANOVA with Bonferroni post-hoc tests were used for individual comparisons of normally distributed data. Normality was assessed using D'Agostino & Pearson normality test. When normality was not assumed Kolmogorov-Smirnov test and Wilcoxon signed-rank test were performed for individual comparisons. P-values represent \* $p < 0.05$ ; \*\* $p < 0.01$ ; \*\*\* $p < 0.001$ . All data were represented as the mean  $\pm$  SEM or STD. All sample sizes and definitions are provided in the figure legends. After the conclusion of experiments, virus-expression and

implants placement were verified. Mice with very low or null virus expression were excluded from analysis.

# Results

## 4.1 Single-nuclei transcriptomic characterization of adult BLA neuronal types

We characterized transcriptomic cell types using single-nucleus RNA sequencing (snRNAseq) from the adult mouse basolateral amygdala (BLA), spanning 2.4 mm in the anterior-posterior direction (Figure 1A). To spatially annotate the cell clusters, we used a regional parcellation method published previously 4 (Figure 1B). Our initial analysis of the BLA transcriptomic dataset identified seven transcriptomic cell types, including 3,278 non-neuronal and 4,544 neuronal cells (Figure S1A,B). We re-clustered the neuronal cells only and separated them into GABAergic and glutamatergic neurons using specific markers for inhibitory (*Gad1*, *Gad2* and *Slc32a1*) and excitatory (*Slc17a7*) neurons (Figure 1C). Separate re-clustering of GABAergic neurons revealed 10 clusters, including intercalated cells (ITC) and amygdalostriatal area cells (marked by *Foxp2* and *Rarb*, respectively) and a newly identified cluster marked by *Tshz2* and *Rmst*, which appeared to be equally related to ITC and BLA GABAergic interneurons (Fig S1C, D). The GABAergic interneurons were separated into two populations marked by *Reln* and *Calb1* (Fig S1D). The *Calb1* population included *Calb1*, *Sst* and *Htr2a* clusters, while the *Reln* population contained *Lamp5*, *Ndnf*, and *Cck* clusters (FigS1D, S1E), showing distinct transcriptomes and correlations with each other (Fig.S1E). These findings agreed well with recent scRNA-seq studies from cortex and BLA 35–37.

Separate re-clustering of glutamatergic BLA cells identified 12 clusters including one cluster (cluster 10) from posterior medial amygdala (MEAp) marked by *Esr1* and *Pde11a* 38 (Figure 1D). Compared to GABAergic clusters, glutamatergic clusters shared many of their

top 5 differentially expressed genes (DEGs). For example, all top 5 genes for cluster 2 (cl2) were also expressed in cl6. *Rspo2* was expressed in cl1 and 11, and *Rorb* in cl7 and cl8 (Figure 1D). To identify unique combinations of markers for glutamatergic clusters, we analyzed the top 30 DEGs with adjusted p-value cutoff of 0.05 and an average log-fold change of at least 0.55 (see methods) and selected those genes that expressed in one or two clusters. This 1st filter revealed at least three selected markers for each cluster (Figure 1F). We then inspected the spatial expression of each marker in the Allen brain atlas and selected 10 genes that appeared to be expressed in subregions of the BLA (FigS1F). Marker genes that were expressed homogeneously throughout the BLA or showed high expression in nearby brain regions were not selected (FigureS1G). Some of the selected genes were strongly enriched in one cluster, including *Sema5a* (cl5), and *Grik1* (cl12), while others were enriched in two or more clusters, including *Rorb* (cl7,8), *Otof* (cl2,3,6) and *Lypd1* (cl2,8,9) (Figure1F). By this analysis, every cluster of glutamatergic BLA neurons could be represented by a combination of one to four marker genes (Figure 1E, F). This approach provided a combinatorial set of marker genes for spatial mapping of molecularly-defined glutamatergic BLA cell types.

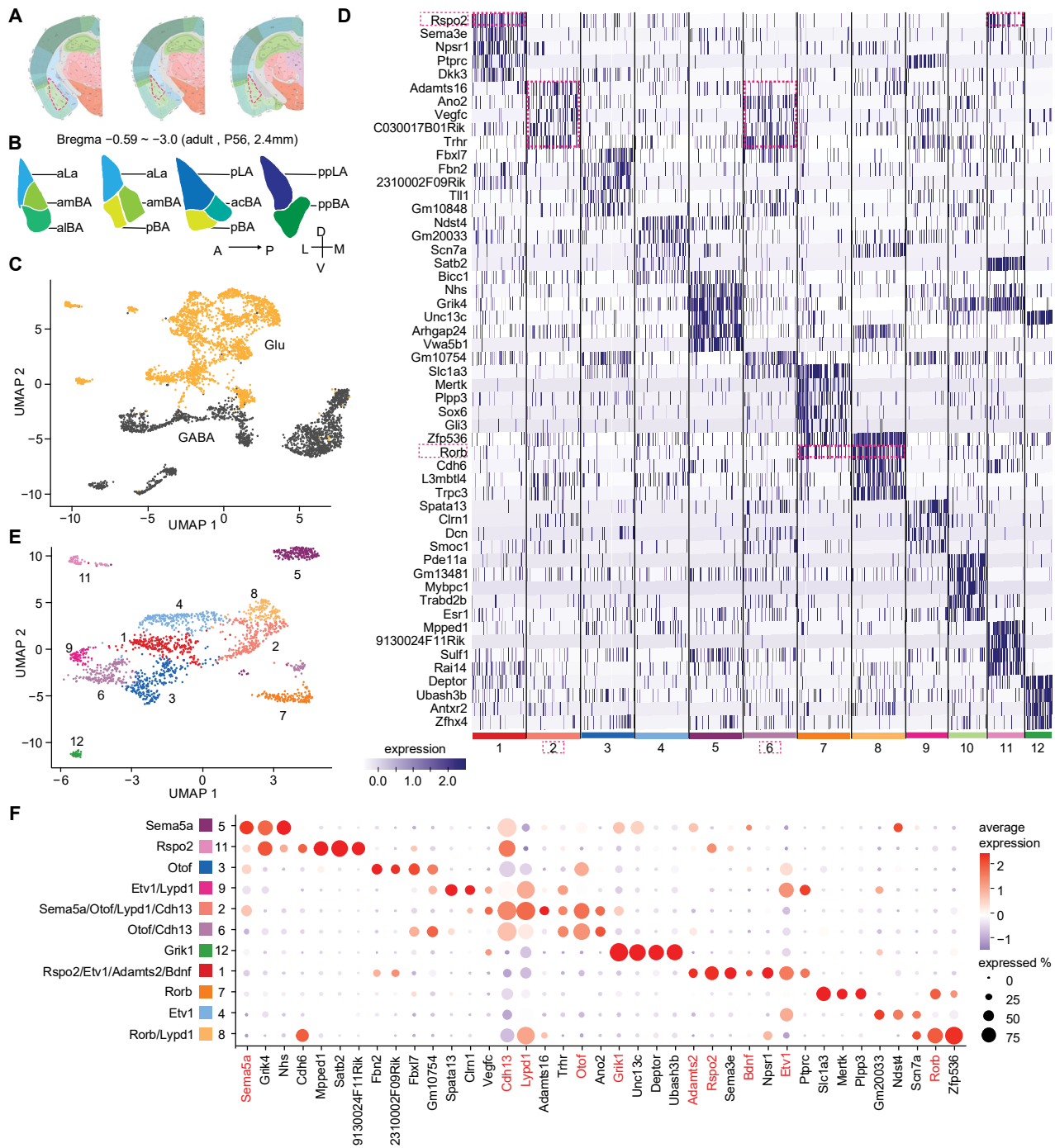


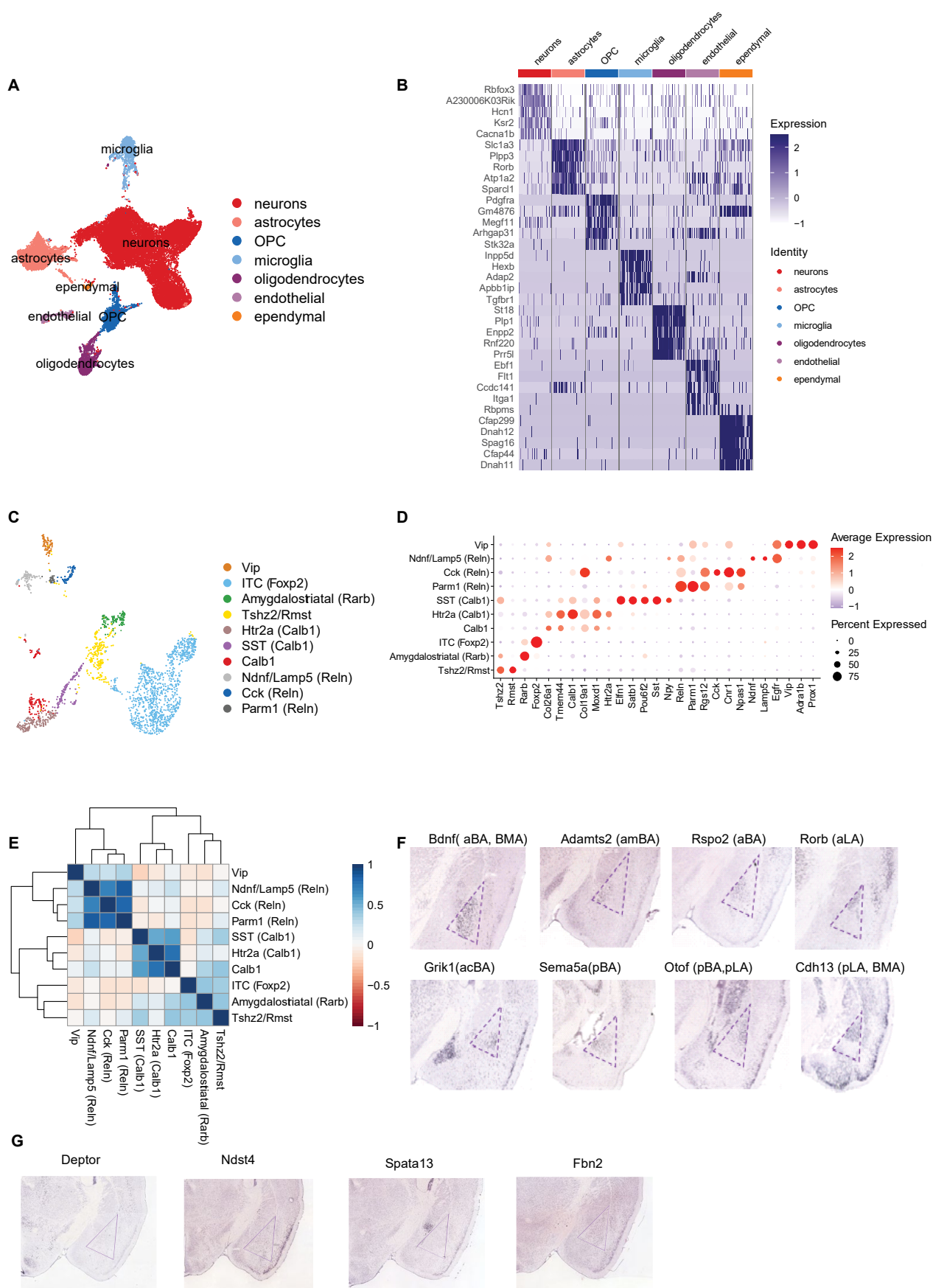
**Figure 1. Single-nuclei transcriptomic characterization of adult BLA neuron types**

- A) Schemes showing the sampled BLA regions highlighted with a triangle. The anterior-posterior extent of the samples ranged from bregma 0.59 ~-3.0 covering around 2.4 mm.
- B) Schemes showing regional parcellation of the BLA along the anterior-posterior axis (adapted from (Hintiryan et al. 2021)). Abbreviations: acBA, anterior-caudal BA; aLA,



anterior LA; alBA, anterior-lateral BA; amBA, anterior-medial BA; pBA, posterior BA; pLA, posterior LA; ppBA, posterior-posterior BA; ppLA, posterior-posterior LA.

- C) UMAP of BLA neurons (n=4,544) with cells classified as GABAergic (GABA, n=2,033, black) and glutamatergic (Glu, n=2,511, orange), respectively.
- D) Heatmap of the top 5 marker genes in each cluster of glutamatergic neurons.
- E) UMAP of glutamatergic neuron clusters after separate dimension reduction and clustering. Cell type color palette reflects the one shown in panel F.
- F) Molecular signatures of glutamatergic clusters in dot plot visualization of average gene expression of selected candidate genes. Genes highlighted in red were selected as ten key markers; percentage of cells expressing the selected marker is indicated by circle size and average gene expression level by color scale.



### **Supplementary. Figure S1 related to figure 1: total transcriptomics and GABAergic clusters in BLA**

- A) UMAP of all BLA cells with different cell types identified by established markers.
- B) Heatmap illustrating expression levels of top 5 marker genes in different cell types.
- C) UMAP of GABAergic neurons with annotated clusters.
- D) Molecular signatures of GABAergic neuronal clusters based on expression of selected marker genes.
- E) Heatmap visualization of pairwise correlation matrix of marker gene expression between clusters of GABAergic BLA neurons. Scale bar indicates Pearson's R.
- F) Representative ISH images from Allen ISH data for some of final 10 marker genes for glutamatergic clusters.
- G) Representative ISH images from Allen ISH data for genes not selected as marker-genes due to their widespread expression in many brain regions (Ndst4, Fbn2), low expression (Deptor), or high expression in other brain regions (Spata13).

## **4.2 Transcriptional correlation of genes spatially marked BLA subregions**

### **Spatial organization of glutamatergic BLA clusters**

For spatial mapping of glutamatergic BLA clusters, we performed sequential multiplexed fluorescence in situ hybridization (smFISH) from anterior to posterior whole BLA coronal sections (Fig.S2-3). We used four coronal sections (designated “anterior”, “anterior-middle”, “posterior-middle” and “posterior”) to divide the BLA into eight subregions from anterior to posterior (aLA, pLA, ppLA, amBA, alBA, acBA, pBA, ppBA) according to published methods 39(Figure 2A-D). The numbers of cells positive for each marker gene; (Lypd1, Etv1, Cdh13, Rspo2, Rorb, Grik1, Bdnf, Otof, Adamts2, Sema5a) were counted and the fractions of positive cells in each subregion were analyzed (Figure 2E, see Methods). Briefly, we thresholded the fluorescence of each marker gene to determine whether a cell was positive or negative for a particular marker and then calculated the percentages of positive cells for each gene within each subregion. Since some cells were positive for multiple markers, the

sum of cell fractions per subregion exceeded 100%. This analysis also allowed us to compare cell abundance across the different subregions. The results indicated that the clearest distinction was between LA and BA. For example, *Rorb*-positive cells were enriched in LA and less frequent in BA subregions (Fig. 2A-E). *Etv1* and *Rspo2*-positive cells showed the opposite pattern, which was most obvious in anterior and anterior-middle sections (Figure 2A, B). We also observed that cell distributions varied in the A-P axis. For example, *Cdh13* expression was absent in aLA and enriched in ppLA, whereas *Rorb* was enriched in aLA and less so in ppLA (Figure 2A, D). Some patterns were more complex: *Lypd1*-positive cells were enriched in the whole LA and several parts of the BA (Fig. 2A-E). *Grik1*-positive cells were scarce in the most anterior sections and enriched in posterior parts of LA and BA (Figure 2C, E).

Next, we asked if the pattern of cell distribution based on the expression of the ten marker genes would be sufficient to delineate subregions of BLA. Pearson correlation and subsequent hierarchical clustering analysis revealed that LA and BA formed separate clusters which could be further subdivided in the A-P axis, separating aLA from pLA/ppLA, and amBA/alBA from the more posterior acBA/pBA/ppBA (Figure 2F). These results indicate that genetically-marked cell populations were distributed in distinct patterns in BLA subregions.

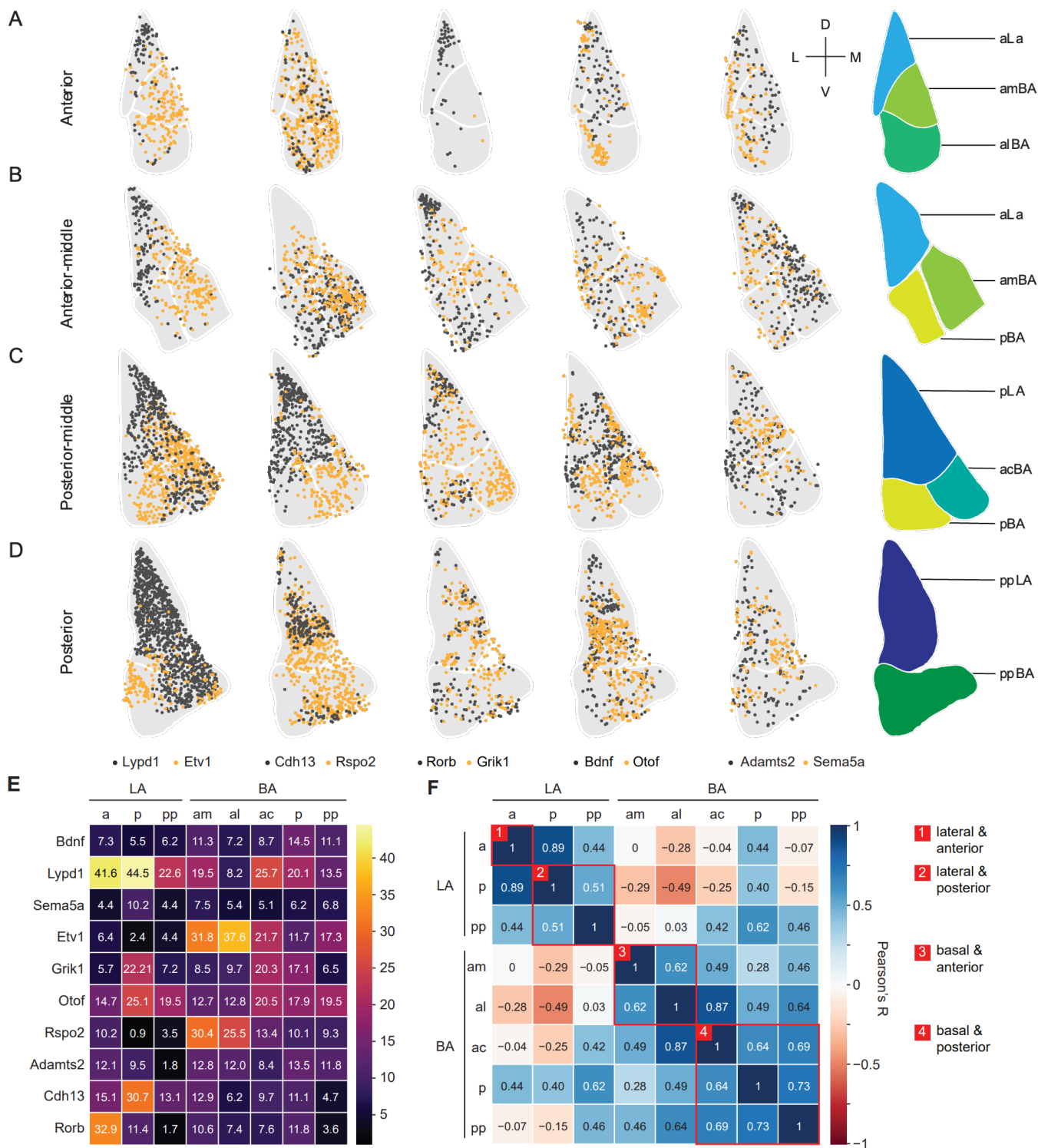


**Figure 2. Distribution of cells positive for selected marker genes in BLA subregions**

(A-D) Distribution of cells within BLA subregions along anterior-posterior axis. Examples of five pairs of marker genes colored in black and yellow are shown from left to right.

(E) Quantification of distribution of cells positive for a specific marker gene within BLA subregions. Heatmap indicating large fractions of cells in yellow and small fractions in dark purple (Average fraction size in percent is indicated in each tile).

(F) Pearson correlation of averages on percentage of cells expressing each gene in eight subregions; colors indicate Pearson's R and categorized red boxes: re-grouping closely correlated subregions to larger category.

a



## C

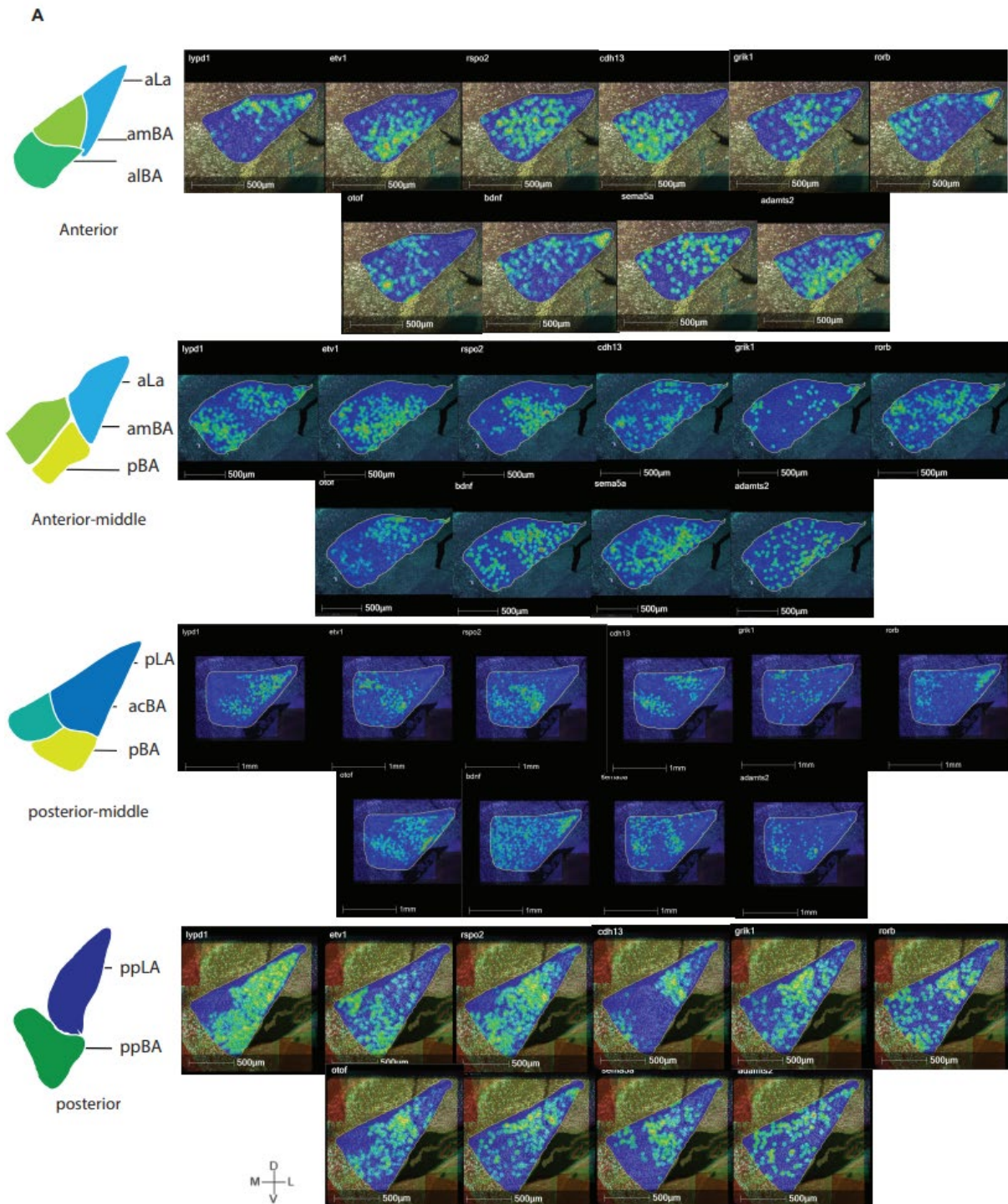


## **Supplementary. Figure S2 related to figure 1-2: workflow of snRNA and smFISH**

Whole Workflow overview from snRNA seq to smFISH image analysis.

- a) Nuclei from BLA tissues were harvested and processed through 10x genomics scRNAseq tools.
- b) Fixed BLA coronal sections were iteratively hybridized and imaged with 10 marker gene probes with different fluorescence.
- c) Image analysis: Four images from 4 rounds of hybridization were superimposed by landmark and serial strain registration, and subregions in BLA were delineated by reference 17. Cell segmentation (based on nuclear Rnu6 expression) and thresholding fluorescence for positive cells for each gene were performed and quantified using HALO software (Indica Labs). After preprocessing, the dataset including x, y positions of positive cells, was transferred to Python workspace for downstream analysis (e.g., PCA and correlation analysis). Details are explained in Methods.





Supplementary. Figure S3. Related to figure 2B, representative images showing

### positive cell for each marker gene

A) Density heatmaps of selected gene expressions in BLA. Representative samples of 10 marker genes at 4 positions are shown from anterior (left top) to posterior (right bottom). The colors represent expression levels, from blue to red color indicating the lowest and

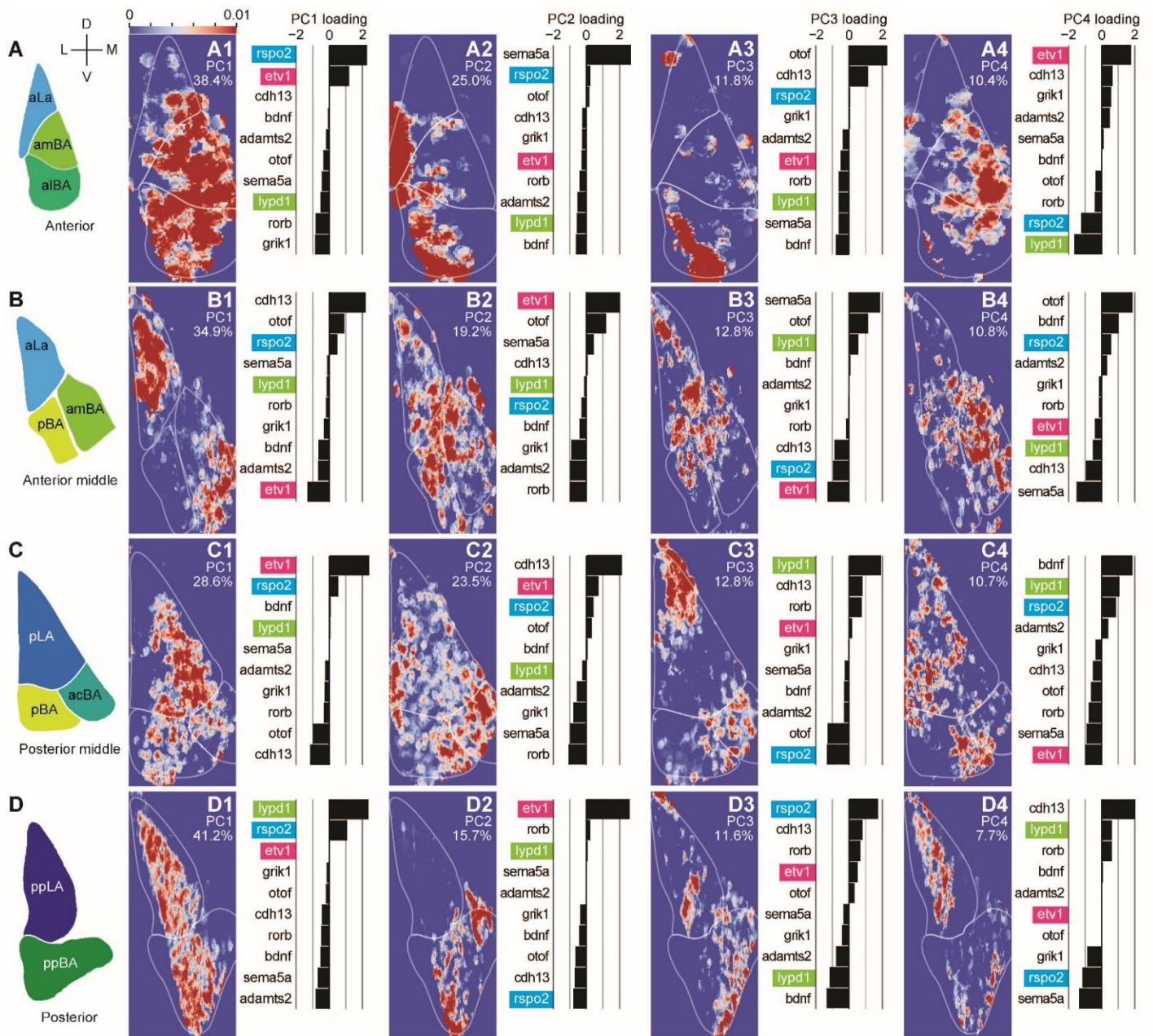
the highest expression levels (radius: 25um). Scale bar: 500µm, M: medial, L: lateral, D: dorsal, V: ventral.

## **The combination of marker genes predicts the spatial localization in the BLA**

During the above analysis, we noticed that the distribution of transcriptionally distinct neurons did not always follow the boundaries of the previously observed/published subregions, raising the possibility that subregions could be further subdivided or arranged differently. For example, *Otof*-positive cells were highly concentrated at the lateral edge of the aBA and rather scarcely present in the rest of the aBA (Figure 2A) and *Cdh13*-positive cells were enriched at the tip of pLA/ppLA (Figure 2C, D). Since every cell was characterized by a unique combination of marker genes and its unique location within the BLA, we next asked in an unsupervised way, whether cells with a similar combination of marker genes would localize to a similar subregion of the BLA. For this, we used principle component analysis (PCA) to examine the variation of marker gene expression in BLA neurons and re-constructed the spatial localization of each principle component (PC) back into the BLA. The eigen-images from the top 4 PCs explained on average  $80.8 \pm 5.16\%$  of variance in each sample. The results indicated that the PC associated with the largest variation in gene expression corresponded to differences between LA and BA (Fig.S4). PCA also revealed that the markers *Etv1*, *Rspo2* and *Lypd1* had large loadings in the top 4 PCs that demarcate the boundary between LA and BA. For example, *Etv1* and/or *Rspo2*-positive cells contributed most to BA-specific PCs (Fig. S4 A1, B2, C2, D2), while *Lypd1*-positive cells contributed most to LA-specific PCs (Fig.S4 B3, C3, D3, D4).). In addition, *Cdh13*-positive cells also contributed to LA-specific PCs (Fig, S4 B1, C3, D4). In summary, our findings suggest that cells with a similar combination of marker genes localized to similar subregions of the BLA. Moreover, the expression patterns of *Etv1*, *Rspo2* and *Lypd1*, parcellated the BLA into its LA and BA subdomains. These results show that genetically-marked cell populations distribute in distinct BLA subregions when analyzed in an unsupervised way.

To enhance the confidence of the transcriptomic and spatial expression analysis, we performed additional correlation analysis. We correlated the snRNAseq transcriptomes of all the cells positive for one of the ten marker genes and found that *Etv1*, *Bdnf*, *Adamts* and

*Rspo2* were closely correlated and separated from the others (Figure S5A). We also correlated the spatial coordinates from the smFISH data of all the cells positive for one of the markers. Similarly, we found that *Etv1*, *Bdnf*, *Adamts* and *Rspo2* were closely correlated and expressed in anterior BA (Figure S5A). Overall, the correlation patterns were very consistent: *Otof*, *Lypd1* and *Cdh13* were always closely correlated and expressed in posterior LA. Also, *Sema5a* and *Grik1* were closely correlated and expressed in posterior BA (Figure S5A, B).

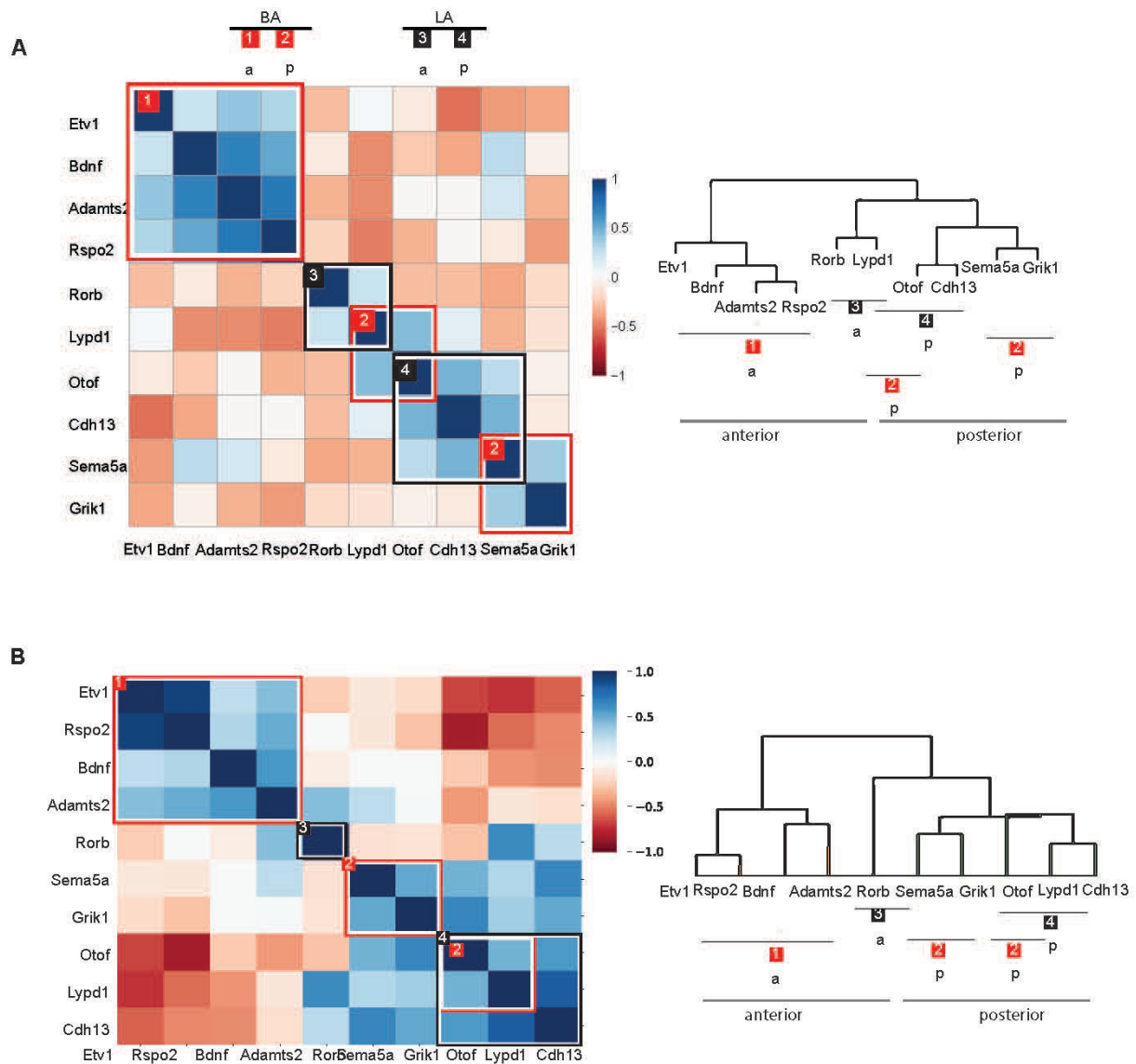


**Supplementary. Figure S 4. related to figure 2B; The combination of marker genes predicts the spatial localization in the BLA**

(A-D) Left: Anatomical parcellations from anterior (A), anterior-middle (B), posterior-middle (C) and posterior (D) BLA as previously published 17. Right: Eigen-images from the top 4 principal components (PCs) in 4 samples with percentage of each PC from the spatial distribution of principal component analysis (PCA) of marker-genes in single cell resolutions with each bar graph of PC loading values from each marker gene for each PC axis; PC1 to



PC4 (left to right in order). Contributions of Rspo2, Etv1, and Lypd1-positive cells to LA- and BA-specific PCs are highlighted.



**Supplementary. Figure S 5 related figure 1-2; correlation patterns from snRNA and smFISH data: Multimodally confirmed transcriptionally defined cell types represent anatomically defined topography.**

- A) Pairwise correlation heatmap with hierarchical clustering of marker gene expression across all glutamatergic neurons (snRNAseq data, related to Figure 1) Scale bar indicates Pearson's correlation coefficient.
- B) Pairwise correlation heatmap with hierarchical clustering of marker gene expression across eight BLA subregions (smFISH data, related to Figure 2); Boxes in heatmap and lines in dendrogram: manual grouping of closely correlated genes by their spatial expression, red for basal (BA), black for lateral (LA) and 1, 3 for anterior (a) and 2,4 for posterior (p).

### 4.3 Expression of transcriptional clusters in BLA subregions

Until now, we used the data from smFISH to assign each cell to a specific BLA subregion. Next, we assigned each transcriptomic cell cluster to a space in the BLA in an unsupervised way using Pearson correlation analysis. Since every cell belonged to a transcriptomic cell cluster and, in addition, was characterized by the smFISH read counts of ten marker genes, we could calculate the scaled sums of expression of the ten marker genes for each cluster (Figure S6A). For example, cluster 2 was characterized by high expression of *Sema5a/Otof/Lypd1/Cdh13* (0.96-1.0) and lower expression of *Etv1* (0.63) and *Rspo2* (0.47).

In the smFISH data, every cell was characterized by the normalized expression of ten marker genes. We therefore correlated (Pearson) the smFISH marker expression pattern (Figure S6A) to each transcriptomic cluster marker expression pattern and assigned each smFISH cell to one of the 11 clusters according to the highest correlation coefficient (Figure S6B). For example, one smFISH cell (Cell ID # 3234) with high *Etv1* expression had highest correlation coefficient with cl4 (*Etv1*; R: 0.46) and was therefore assigned as cl4. Another smFISH cell (cell ID # 1936) with high *Rspo2* expression showed higher correlation coefficient to cl11 (R:0.46), while a cell (cell ID # 5065) with high *Lypd1* expression showed higher correlation coefficient to cl2 (R: 0.71) (Figure S6B). After the assignment of all smFISH cells to individual transcriptional clusters, all cells were reconstructed into BLA space by using the spatial coordinates from smFISH (FigureS6C, Methods for details). For example, cl1, and cl11 were enriched in anterior BA, cl4 more in the posterior BA (Fig. 3A). These three clusters were characterized by high expression *Rspo2* and *Etv1*. Instead, cl2

and cl8 were enriched in pLA or ppLA (Fig. 3A) and were characterized by high expression of *Lypd1*. cl7 was enriched in anterior LA and was characterized by high expression of *Rorb*. By this analysis, transcriptomic clusters could be annotated to BLA subregions (Fig. 3B).

Using average expression of the ten marker genes for each cluster we analyzed the correlation between clusters and generated a hierarchical tree (Fig. 3C). We annotated the tree with BLA subregions from the above analysis. Those clusters localized to LA correlated more highly compared to BA clusters. And in each branch of the tree, clusters separated according to their A-P axis. (Fig. 3C). In summary, these results from unsupervised analysis suggest that transcriptionally distinct cell clusters of glutamatergic neurons distribute in distinct BLA subregions.

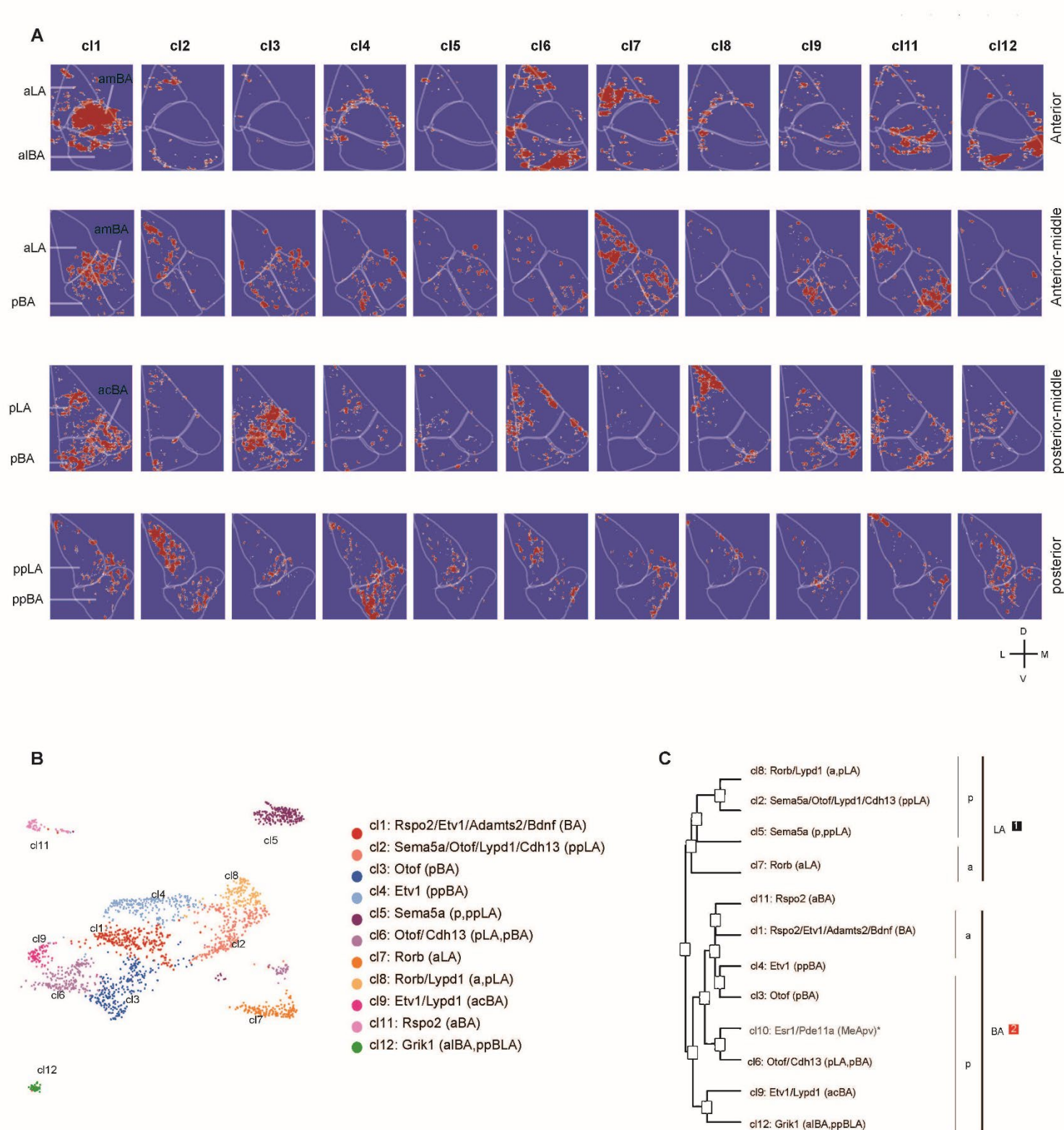


**Figure 3. Spatial expression of transcriptional clusters**



- (A) Mapping of snRNA-Seq clusters (11 clusters) to smFISH signals and corresponding locations in the BLA; Panels from top to bottom indicate anterior to posterior sections and colors represent binary expression (Red= expression, Blue = no expression, each cell ID is created after normalization within a radius of 50  $\mu$ m)
- (B) Final annotation of snRNA clusters with respect to expression of markers genes and their distribution in BLA subregions.
- (C) Dendrogram of snRNA clusters based on hierarchical clustering of aggregated mRNA expression (Subregions were categorized into large two categories either LA or BA (a, anterior and p, posterior))

A

	Bdnf	Adamts2	Rorb	Grik1	Sema5a	Rspo2	Etv1	Lypd1	Otof	Cdh13
cl1: Rspo2/Etv1/Adamts2/Bdnf	1.00	1.00	0.39	0.36	0.75	1.00	1.00	0.74	0.63	0.56
cl2: Sema5a/Otof/Lypd1/Cdh13	0.48	0.61	0.37	1.00	0.96	0.47	0.63	1.00	1.00	1.00
cl3: Otof	0.86	0.80	0.11	0.74	0.96	0.77	0.86	0.79	0.99	0.77
cl4: Etv1	0.77	0.62	0.71	0.22	0.19	0.68	0.92	0.84	0.57	0.56
cl5: Sema5a	0.89	0.80	0.29	0.93	1.00	0.43	0.35	0.47	0.76	0.86
cl6: Otof/Cdh13	0.42	0.79	0.47	0.63	0.55	0.58	0.67	0.88	0.99	0.96
cl7: Rorb	0.42	0.43	0.87	0.45	0.46	0.58	0.55	0.58	0.61	0.60
cl8: Rorb/Lypd1	0.52	0.00	1.00	0.24	0.00	0.46	0.37	0.82	0.21	0.60
cl9: Etv1/Lypd1	0.07	0.57	0.05	0.24	0.46	0.35	0.67	0.69	0.55	0.68
cl11: Rspo2	0.21	0.58	0.29	0.00	0.46	0.69	0.00	0.00	0.06	0.74
cl12: Grik1	0.00	0.11	0.00	0.73	0.15	0.00	0.31	0.27	0.00	0.00

B

	Bdnf	Adamts2	Rorb	Grik1	Sema5a	Rspo2	Etv1	Lypd1	Otof	Cdh13	R Cell #3234	R Cell #1936	R Cell #5065
cl1: Rspo2/Etv1/Adamts2/Bdnf	1.00	1.00	0.39	0.36	0.75	1.00	1.00	0.74	0.63	0.56	0.36	0.36	-0.20
cl2: Sema5a/Otof/Lypd1/Cdh13	0.48	0.61	0.37	1.00	0.96	0.47	0.63	1.00	1.00	1.00	-0.16	-0.38	0.71
cl3: Otof	0.86	0.80	0.11	0.74	0.96	0.77	0.86	0.79	0.99	0.77	0.14	0.01	0.29
cl4: Etv1	0.77	0.62	0.71	0.22	0.19	0.68	0.92	0.84	0.57	0.56	0.46	0.11	-0.11
cl5: Sema5a	0.89	0.80	0.29	0.93	1.00	0.43	0.35	0.47	0.76	0.86	-0.44	-0.33	0.19
cl6: Otof/Cdh13	0.42	0.79	0.47	0.63	0.55	0.58	0.67	0.88	0.99	0.96	-0.04	-0.20	0.63
cl7: Rorb	0.42	0.43	0.87	0.45	0.46	0.58	0.55	0.58	0.61	0.60	-0.01	0.07	0.08
cl8: Rorb/Lypd1	0.52	0.00	1.00	0.24	0.00	0.46	0.37	0.82	0.21	0.60	-0.06	0.04	0.16
cl9: Etv1/Lypd1	0.07	0.57	0.05	0.24	0.46	0.35	0.67	0.69	0.55	0.68	0.34	-0.12	0.61
cl11: Rspo2	0.21	0.58	0.29	0.00	0.46	0.69	0.00	0.00	0.06	0.74	-0.36	0.46	0.16
cl12: Grik1	0.00	0.11	0.00	0.73	0.15	0.00	0.31	0.27	0.00	0.00	0.23	-0.24	-0.17
Cell #3234	0.00	0.00	0.00	0.00	0.00	0.00	0.33	0.00	0.00	0.00	cl4: Etv1		
Cell #1936	0.00	0.00	0.00	0.00	0.00	0.14	0.00	0.00	0.00	0.00		cl11: Rspo2	
Cell #5065	0.00	0.00	0.00	0.00	0.10	0.02	0.00	0.15	0.07	0.15			cl2: Sema5a/Otof/Lypd1/Cdh13

C

mFISHgene expression/Cell ID	#1936	#3234	#5065	
Bdnf		0	0	0
Adamts2		0	0	0
Rorb		0	0	0
Grik1		0	0	0
Sema5a		0	0	0.097561
Rspo2	0.142857		0	0.02439
Etv1		0	0.333333	0
Lypd1		0	0	0.146341
Otof		0	0	0.073171
Cdh13		0	0	0.146341
cluster ID				
cl4: Etv1		0	1	0
cl9: Etv1/Lypd1		0	0	0
cl12: Grik1		0	0	0
cl3: Otof		0	0	0
cl6: Otof/Cdh13		0	0	0
cl7: Rorb		0	0	0
cl8: Rorb/Lypd1		0	0	0
cl11: Rspo2		1	0	0
cl1 : Rspo2/Etv1/Adamts2/Bdnf		0	0	0
cl5: Sema5a		0	0	0
cl2: Sema5a/Otof/Lypd1/Cdh1		0	0	1
X max	2006	1813	1100	
Y max	1775	2175	666	

Supplementary.

Figure S6 related to figure 3.

(A) The scaled sum of the expression of ten marker genes in all cells per each cluster from transcriptomics.

(B) Representative

data tables explaining how to calculate correlation coefficient (R) from a single smFISH

cell (# 3234 for cl4, # 1936 for cl11, # 5065 for cl2) to assign the best correlated transcriptional cluster.

(C) Representative table showing the assignment of three example cells from smFISH to the best correlated transcriptional cluster and the corresponding X, Y position in the BLA.

## 4.4 Cell type specific- functional circuits for valence

### 4.4.1 Activities of BLA<sup>Lypd1</sup> neurons increase during fasting and feeding

We selected three genetic markers for functional analysis. *Lypd1*, the marker with highest expression in LA and additional regions in BA, targeting three transcriptomic clusters (cl2,8,9); *Etv1*, the marker with scarce expression in LA, complementary pattern with *Lypd1* in BA subregions, targeting three clusters (cl1,4,9); *Rspo2*, scarce expression in LA, restricted pattern in anterior BA, partially overlapping with *Etv1*, targeting two clusters (cl1,10). Among these markers, only *Rspo2* had previously been analyzed functionally and will serve as a reference for comparison (J. Kim et al. 2016). A comparative mRNA expression analysis revealed that *Lypd1*-expressing cells showed little overlap with *Etv1*- or *Rspo2*-expressing cells (typically less than 20% overlap, Fig.S7C). *Etv1*- and *Rspo2*-expressing cells overlapped strongly in anterior sections (55%) and much less in posterior sections (30%) (Fig.S7C). The fraction of *Lypd1*-expressing cells increased from anterior to posterior, while those of *Rspo2*- and *Etv1*-expressing cells decreased from anterior to posterior.

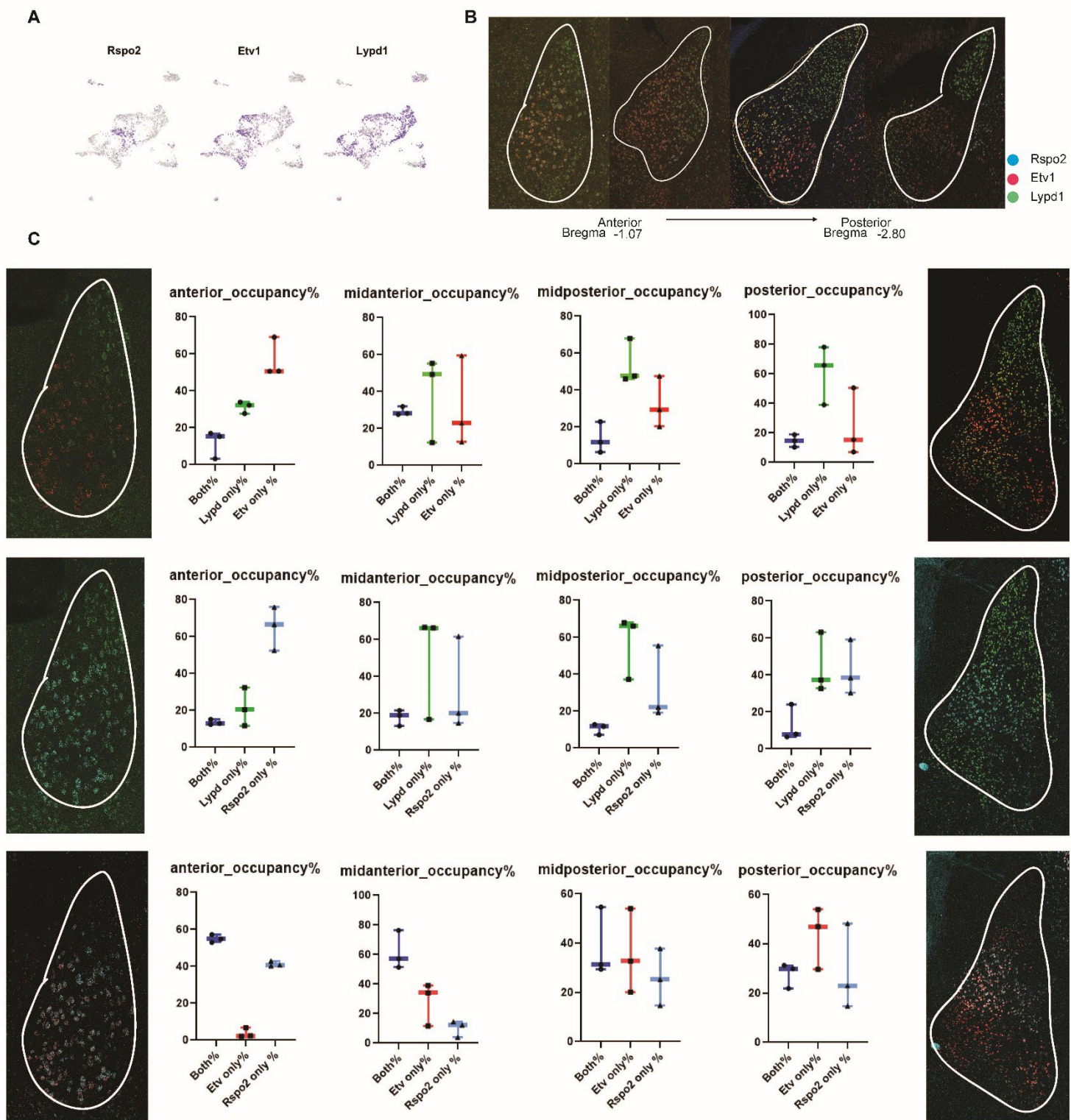
To analyze the intrinsic physiological properties of the neurons marked with the three selected genes, we used the respective Cre lines, *Lypd1*-Cre, *Etv1*-CreER, and *Rspo2*-Cre, and validated Cre expression in comparison to the endogenous markers (Fig. S8). We crossed the Cre lines to a tdTomato reporter line and performed ex vivo electrophysiology in brain slices. Whole cell current-clamp recordings revealed significant differences in the membrane potentials with BLA<sup>Lypd1</sup> neurons showing the most negative and BLA<sup>Rspo2</sup> neurons the least negative (Figure 4A), suggesting that BLA<sup>Lypd1</sup> neurons may require more excitatory inputs to fire than the other two. Basic firing rates did not differ between cells (Figure S9A); however, spontaneous excitatory postsynaptic currents (sEPSC) had a lower amplitude and spontaneous inhibitory postsynaptic currents (sIPSC) had lower frequency in

BLA<sup>Lypd1</sup> than BLA<sup>Rspo2</sup> cells (Fig.S9B), suggesting that BLA<sup>Lypd1</sup> cells express fewer glutamate receptors and receive fewer inhibitory inputs.

Since part of our analysis involved appetitive behavior (see below), which is known to be controlled by BLA neurons (Janak and Tye 2015; J. Kim et al. 2016), we asked if overnight fasting would modify neuronal activities. Current-clamp recordings showed that the firing rates of BLA<sup>Lypd1</sup>, but not BLA<sup>Etv1</sup> neurons, increased in fasted mice and their membrane potentials depolarized (Figure 4B-F). This suggests that fasting increased the excitability of BLA<sup>Lypd1</sup> neurons. Recordings of excitatory and inhibitory neurotransmission revealed increased frequencies of sEPSC and sIPSC in BLA<sup>Lypd1</sup> neurons after fasting (Figure 4G-I). Additionally, the decay time for sEPSC decreased in BLA<sup>Lypd1</sup> neurons after fasting, suggesting changes in the kinetics of the excitatory receptors (Figure 4J). Other electrophysiological parameters measured in Lypd1 neurons did not change after fasting (Fig. S9C). Together these results suggest that the physiological properties of BLA<sup>Lypd1</sup> neurons change during periods of energy deficits.

To understand how these BLA neuron populations modulate appetitive and defensive behaviors, we performed single-cell-resolution *in vivo* calcium imaging in freely moving mice. A graded-index (GRIN) lens was implanted above the BLA in the respective Cre lines previously injected with an AAV expressing a Cre-dependent GCaMP6f calcium indicator (Fig. S9E). Calcium activity was monitored with a head-mounted miniaturized microscope in a free feeding assay (Ghosh et al. 2011) (Figure 4K). We quantified mouse feeding behavior according to their approach behavior towards food rather than food consumption, because in previous work on central amygdala neurons, the presence of food correlated better with neuron activity than food consumption (Ponserre et al. 2022). In order to visually inspect the correlation between the neural activities and the distance to food, we plotted the firing rate inferred from the calcium traces (see Methods for details) with the behavior trace (Figure 4L). We observed many neurons with substantially high firing rates in specific areas. In some of these neurons, these high firing rate areas partially overlapped with the location of the food container, while we observed the opposite in other neurons (Figure 4L). To quantitatively assess the relationship between firing rate and the distance to food, we used spike detection to deconvolve calcium traces and divided the distance to food into 31 bins and computed the average firing rate at each distance bin for each neuron. The area in which we observed feeding behavior, was within a 5 cm radius around the food container

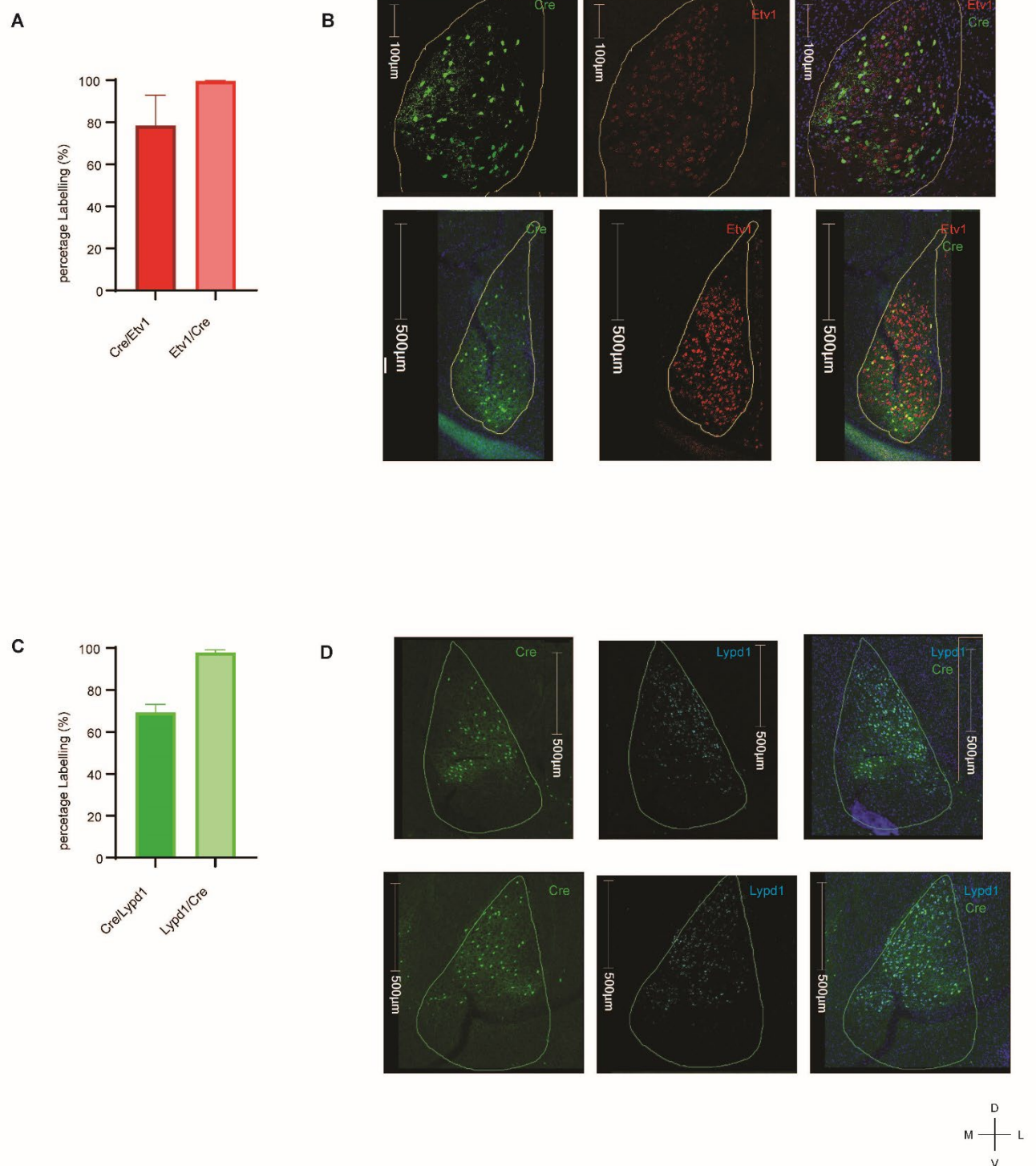
and was termed the pro-food area. The area in which no approach towards food was observed, was outside a 17 cm radius around the food container and was termed the anti-food area. The area in-between was termed neutral area (Figure 4L-N). For each neuron, we determined the peak firing rate, which was then used to sort the neuron into pro-food, neutral, or anti-food areas (Figure 4M, N). We also performed a permutation test to identify the neurons whose activity was significantly correlated with the distance to food (see method for details). In brief, we computed the null distance distribution after shuffling the spike train for each neuron and determined if the neuron was considered significantly tuned to distance to food (termed “significant neurons”), by calculating if the maximum average firing rate of the distance distribution of a neuron was higher than 95% of the null distribution (Figure 4N, O). Therefore, we found that the sorting pattern upon food-distance of the significant neurons was consistent with the pattern of all neurons (Figure 4M-O). The quantification of all neurons revealed that the largest fraction of active neurons in the BLA<sup>Lypd1</sup> population was in the pro-food area (40.8%) (Figure 4P). This value (percentage) was statistically significant, when we computed the null percentage distribution from all pooled neurons from the 3 populations (shuffled data), randomly selected N neurons (N equals the number of neurons in the tested population), and compared the percentage of recorded data with the shuffled data (Figure 4P, left). Consistently, the percentage of BLA<sup>Lypd1</sup> significant neurons in the pro-food area was significantly higher than chance level in comparison with the shuffled data from all Lypd1, Etv1 and Rspo2 significant neurons (Figure 4P, right). This was in contrast to the BLA<sup>Etv1</sup> population, where only the anti-food fraction in the significant neurons was larger than chance level (Figure 4Q). In case of BLA<sup>Rspo2</sup> neurons, the fractions of active cells in the neutral area across both all and significant neurons were larger than the chance level (Figure 4R). The averages of food consumption for recorded mice were similar across Cre lines (Fig S9G). These findings confirmed that the representation of neuronal activities according to distance-based food preference is statistically reliable and further revealed that BLA<sup>Lypd1</sup> neurons were activated during fasting and food approach behavior.



**Supplementary. Figure S 7 related to figure 4-7: three genes (Lypd1, Rspo2, Etv1) differences**

- A) UMAP plots showing *Lypd1*-, *Rspo2*-, and *Etv1*-positive clusters in BLA.
- B) Spatially distinguishable expression of three selected genes in BLA from anterior to posterior, with the white guided line for BLA. (Blue: BLA <sup>Rspo2</sup>, Red: BLA <sup>Etv1</sup>, Green: BLA <sup>Lypd1</sup> neurons)
- C) Occupancy graphs showing percentages of positive cells expressing one gene or the combination of two genes, along the anterior-to-posterior axis together with representative confocal images (Left: anterior, Right: posterior). *Etv1* with Red, *Lypd1* with Green and *Rspo2* with Blue color code.



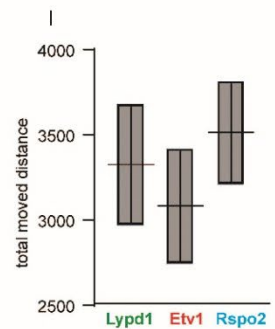
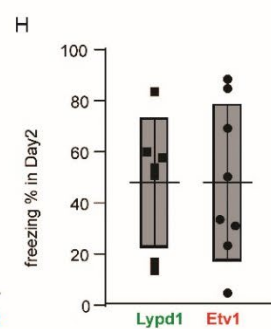
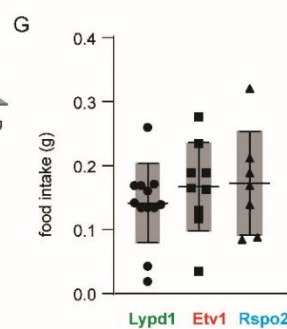
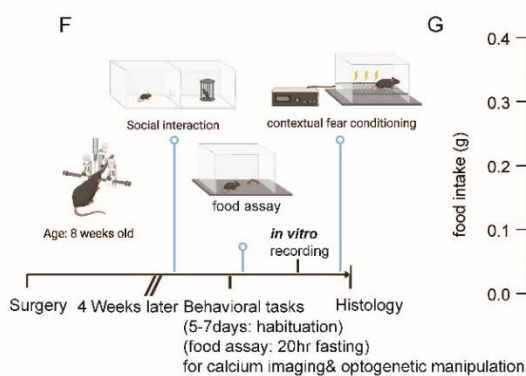
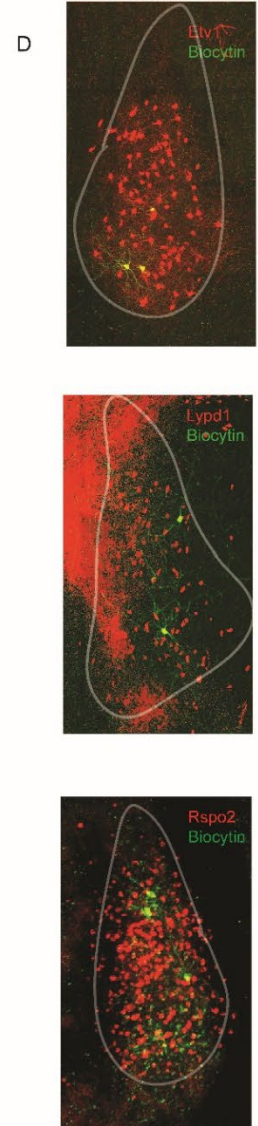
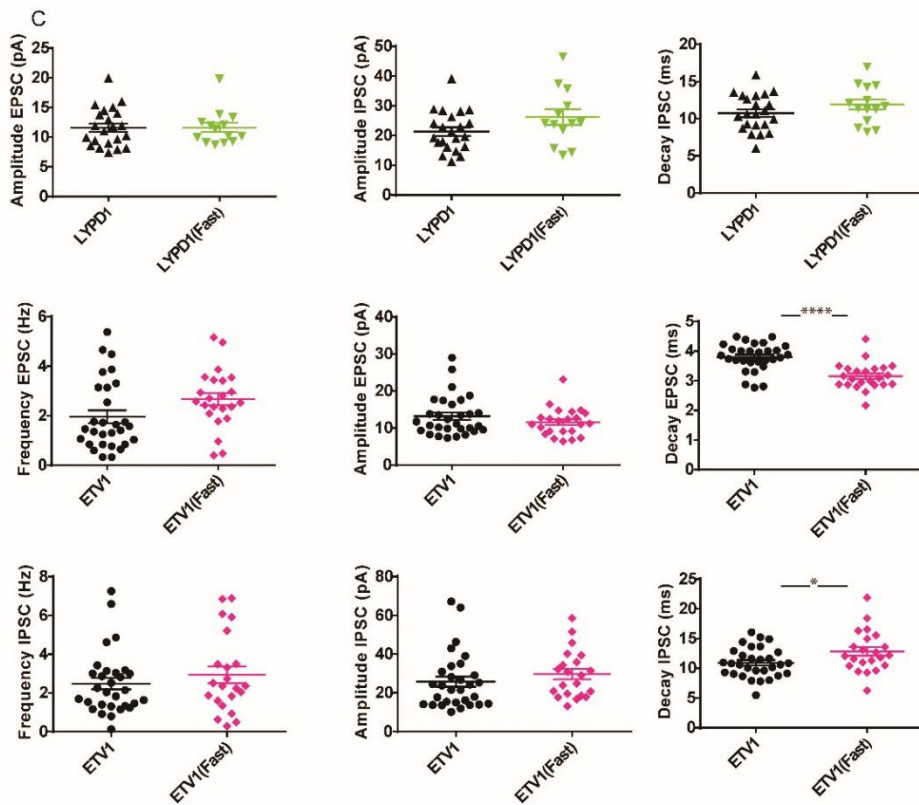
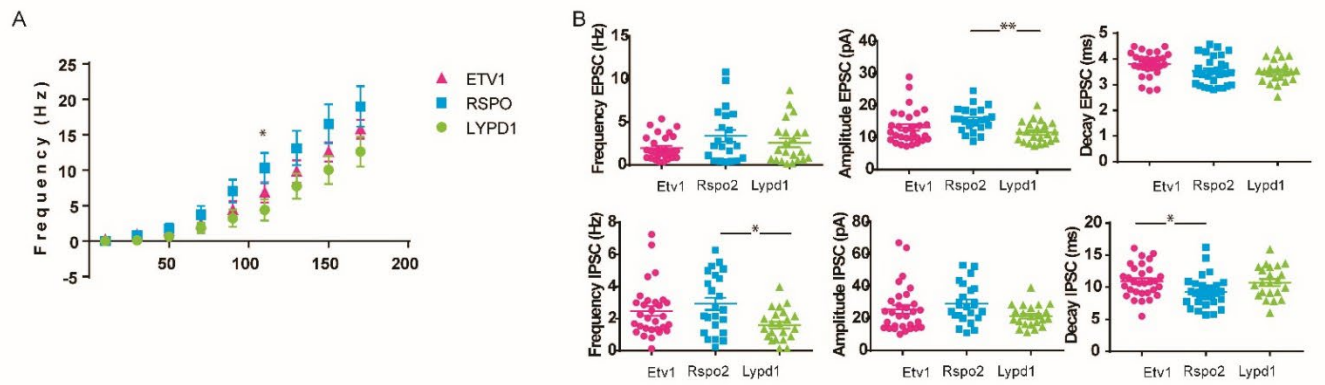


**Supplementary. Figure S 8 related to figure 4-7: Cre validation**



- A) Quantification of the percentage of Etv1-positive cells that co-express tdTomato (Cre/Etv1) and the percentage of tdTomato+ neurons that co-express endogenous Etv1 (Etv1/Cre) (n = 4 sections from 2 mice).
- B) Example images with Etv1-Cre; tdTomato expression (green) and endogenous Etv1 (red) expression in the BLA (a representative anterior (top) and posterior section (bottom)).
- C) Quantification of the percentage of Lypd1-positive cells that co-express tdTomato (Cre/Lypd1) and the percentage of tdTomato+ neurons that co-express endogenous Lypd1 (Lypd1/Cre) (n = 4 sections from 2 mice)
- D) Example images with Lypd1-Cre; tdTomato expression (green) and endogenous Lypd1 (red) expression in the BLA. (Representative anterior (top) and posterior section (bottom)).

Bar graphs show mean  $\pm$  SEM, the BLA region is indicated with a thin line in each image.



**Supplementary. Figure S 9 related to figure 4-5: Electrophysiological properties of three neuronal populations and behavioral parameters of calcium imaging mice**

- A) Firing rates (Hz) after injecting different current steps in three different types of neurons (colored by types of neurons, Two-way ANOVA Mixed-effects analysis: in Rspo2 vs Lypd1,  $*p < 0.05$ , marked at the corresponding step. ( $n$ = neuron numbers;  $BLA^{Lypd1} = 22$ ,  $BLA^{Etv1} = 30$  and  $BLA^{Rspo2} = 21$  from 2 mice per group).
- B) Synaptic properties: Quantification of frequency, amplitude, decay time (left to right) of sEPSC and sIPSC (top to bottom) in three different neuronal populations. One-way ANOVA,  $*p < 0.05$ ,  $**p < 0.01$ . ( $n$ = neuron numbers;  $BLA^{Lypd1} = 22$ ,  $BLA^{Etv1} = 30$  and  $BLA^{Rspo2} = 21$  from 2 mice per group).
- (C-D) Alterations of synaptic properties after fasting: Quantification of amplitude and decay time of sEPSC and sIPSC in  $BLA^{Lypd1}$  neurons in fed or fasted animals (C) and quantification of frequency, amplitude, and decay time of sEPSC (top) and sIPSC (bottom) in  $BLA^{Etv1}$  neurons in fed or fasted animals (D). Unpaired t-test,  $*p < 0.05$ ,  $****p < 0.0001$  (Lypd1-fed and -fast group:  $n = 22$ , 14 neurons and Etv1-fed and -fasted group:  $n = 30$ , 22 neurons from 2 mice per group)
- E) Ex-vivo representative images for neurobiotin-filled  $BLA^{Etv1}$ ,  $BLA^{Lypd1}$  and  $BLA^{Rspo2}$  neurons after whole cell patch-clamping in Etv1-Cre;tdTomato, Lypd1-Cre; tdTomato and Rspo2-Cre; tdTomato mouse, respectively. (tdTomato + neurons (Red), Ex-vivo biocytin neurons (Green) and overlapping neurons (Yellow))
- F) Representative maximum-projection images of focal planes of  $BLA^{Etv1}$ ,  $BLA^{Lypd1}$  and  $BLA^{Rspo2}$ -GCaMP6f expressing neurons. White circles indicated selected ROIs.
- G) Timeline of behavioral tests for calcium imaging and optogenetic manipulation
- H) Average of food consumption in the free-feeding assay during calcium imaging (600s): Lypd1 group:  $n = 12$ , mean = 0.1395, std = 0.06151. Etv1 group:  $n = 9$ , mean = 0.1664, std = 0.06972. Rspo2 group:  $n = 7$ , mean = 0.1718, std = 0.08155 (Dunn's multiple comparisons test, ns).
- I) Average of freezing time (%) on Day 2 during CFC calcium imaging (180s): Lypd1 group:  $n = 7$ , mean = 48.06, std = 24.86. Etv1 group:  $n = 8$ , mean = 48.17, std = 30.29 (Kolmogorov-Smirnov test, ns).

J) Average of total distance moved (cm) in the social assay during calcium imaging (600s):  
Lypd1 group: mean= 3323.64 Std= 357.206, n=6, Etv1 group: mean= 3072.7, Std= 332.517, n= 7, Rspo2 group: mean= 3505.542, Std= 300.4131387, n= 5 (Tukey's multiple comparisons test, ns).

(Electrophysiological recordings in panels A-C were performed by Christian Peters)

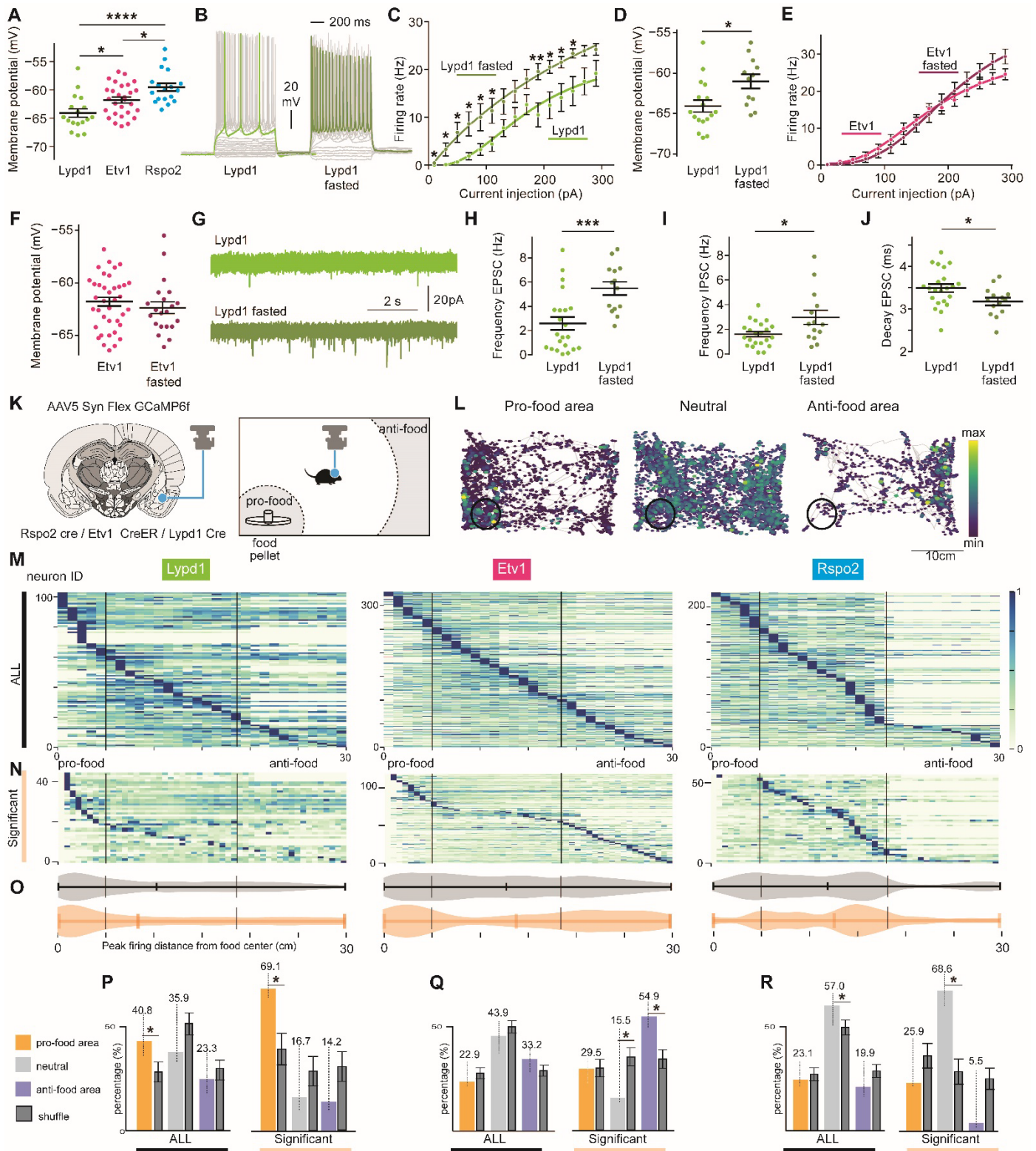


**Figure 4. Genetically- and spatially-defined neurons show different feeding related activities *in vivo* and *in vitro***

A) Membrane potentials of three BLA subpopulations (One-way ANOVA, Bonferroni corrected,  $*p<0.05$ ,  $****p<0.0001$ )

(n=2 mice per group and cell number: Lypd1 = 17, Etv1 = 28 and Rspo2 = 18)

B) Representative whole-cell current-clamp recordings of BLA<sup>Lypd1</sup> neurons from fed and fasted animals.

(C, E) Firing rates (Hz) after injecting different current steps in BLA<sup>Lypd1</sup> neurons (C) and BLA<sup>Etv1</sup> neurons (E) of fed and fasted animals. (Two-way ANOVA Mixed-effects analysis: Fed vs Fasted,  $*p<0.05$ ,  $**p<0.01$  for Lypd1, marked in corresponding steps). Lypd1 fed group: n = 17 cells, Lypd1 fasted group: n = 12 cells, Etv1 fed group = 38 cells, Etv1 fasted group: n = 21cells.

(D, F) Membrane potentials in Lypd1 neurons (D) and Etv1 neurons (F) of fed and fasted animals. Unpaired t-test,  $*p<0.05$ (Lypd1). Lypd1 fed group: n = 17 cells, Lypd1 fasted group: n = 12 cells, Etv1 fed group = 38 cells, Etv1 fasted group: n = 21cells.

(G) Representative sEPSC recordings in Lypd1 neurons of fed and fasted animals

(H-J) Quantification of sEPSC frequency (H), Decay (J) and sIPSC frequency (I) in Lypd1 neurons of fed and fasted animals. Unpaired t-test,  $*p<0.05$ ,  $**p<0.001$ ,  $****p<0.0001$ . Lypd1 fed group: n = 22 cells, Lypd1 fasted group: n = 14 cells.

(K) Schematic explanation of targeted GRIN lens position above GCaMP6f-expressing BLA neurons and free-feeding assay: regions of pro-food and anti-food areas are indicated.

(L) Response map of 3 example neurons whose activities are positively (labelled as pro-food area), negatively (anti-food area) or not correlated (neutral) with the distance to the food chamber, indicated by the black circle. The gray lines indicated the mouse moving trajectories in the chamber. The size and the color of the dots indicate the firing rate of the selected neurons normalized by the maximum firing rate into the range of 0 and 1.

(M, N) Averaged firing rate heatmaps to food distance during the feeding assay in all neurons (M) and in 'significant' neurons whose activity is significantly correlated with the distance to food determined with a permutation test (N). Each row corresponds to a neuron and each column represents a 1 cm distance bin. The pixel values represent the averaged firing rate of the corresponding neurons at the given distance to food normalized by the

peak average firing rate of each neuron. Vertical lines indicate the distance criteria for determining pro-food and anti-food areas. N = 103, 328 and 221 recorded BLA<sup>Lypd1</sup>, BLA<sup>Etv1</sup> and BLA<sup>Rspo2</sup> neurons, respectively.

(O) Violin plots of the peak firing distance of neurons (orange for significant neurons and gray for all neurons). Vertical lines for pro-food and anti-food areas.

(P-R) The percentages of neurons whose firing rates peak in pro-food, neutral and anti-food areas in BLA<sup>Lypd1</sup> (P), BLA<sup>Etv1</sup> (Q) and BLA<sup>Rspo2</sup> (R) populations. Percentage values are indicated in the top of each bar-graph. The significance at the 2.5% significance level in the comparison with the two tails of the null percentage distribution (shuffled) is indicated with an asterisk; shuffled data is shown with SD. The pools of either all neurons or significant neurons are indicated at the bottom of each bar graph.

(Electrophysiological recordings in panels A-J were performed by Christian Peters)

#### 4.4.2 BLA<sup>Etv1</sup> neurons are activated by innate fear stimuli

In previous work, BLA<sup>Rspo2</sup> neurons were activated by electric footshocks during contextual fear conditioning (CFC) (Zhang et al. 2020). We therefore asked, what fractions of BLA<sup>Lypd1</sup> and BLA<sup>Etv1</sup> neurons were activated by these negative valence stimuli. On day 1 of CFC, we recorded neuronal activities during footshocks and compared the firing rates (FR) during the 2 sec before and during footshocks (Figure 5A). Then, we calculated the shock response scores (SRC, see Methods) for each neuron with scores of 1.0 and -1.0 being maximally activated and inhibited, respectively (Figure 5B-C). To classify footshock-positive responsive neurons (pro-footshock) or footshock-negative responsive neurons (anti-footshock), we generated a null SRC distribution from the mean SRC for each shuffled spike train (see method for details). A neuron whose mean SRC was larger than the top 2.5% of the null SRC distribution was considered pro-footshock and a neuron with a mean SRC lower than the bottom 2.5% of the null distribution was considered anti-footshock neuron. This analysis revealed that the fraction of pro-footshock neurons was much larger in the BLA<sup>Etv1</sup> population (42.2%) than in the BLA<sup>Lypd1</sup> population (28.6%) (Figure 5C).

On day 2 of CFC, we monitored the contextual freezing response, which was similar between the two populations of mice (Figure S9H). When we correlated the frequency of freezing of individual mice with the percentage of pro-footshock neurons on day 1, we found a positive correlation in the BLA<sup>Etv1</sup> population, but not in the BLA<sup>Lypd1</sup> population (Figure 5D). These results indicate that a sizeable fraction of BLA<sup>Etv1</sup> neurons was activated by innate fear stimuli and raise the possibility that the fraction of pro-footshock neurons contributes to the conditioned freezing response.

#### 4.4.3 Activities of BLA<sup>Etv1</sup> neurons increase during social interactions

Next, we examined whether these three neuron populations are modulated by social interactions, a type of appetitive behavior that was previously shown to be regulated by the BLA but was not associated with a specific neuron population (Felix-Ortiz and Tye 2014a; Janak and Tye 2015; Wei et al. 2023). We confronted individual mice with a younger conspecific of the same gender in a wired container, either in a round cage or a two-compartment chamber (Figure 5E). Social behavior was quantified as the approach behavior towards the other mouse using data from both chambers. The area in which we



observed social interactions, was within a 10 cm radius around the wired container (a 5cm radius) and was termed the “pro-social area”. The area in which no approach behavior or social interactions occurred was outside a 20 cm radius around the wired container and was termed the “anti-social area”. The area in-between was termed neutral area (Figure 5E).

In the same way as above food assay, we identify the significant neurons correlated to the distance to social and found that the sorting pattern upon social-distance of the significant neurons was consistent with the pattern of all neurons (Figure 5G-I).

Furthermore, the quantification on all neurons revealed that the largest fraction of active BLA<sup>Lypd1</sup> neurons (41.5%) was in the neutral area and the smallest in the pro-social area (24.6%) (Figure 5J) as similar as BLARspo2 neurons with the largest fraction in neutral (39.7%) and the smallest in the pro-social (24%) (Figure 5L). In contrast, the largest fraction of active neurons in the BLA<sup>Etv1</sup> population was in the pro-social area (42.6%) and this value (percentage) was statistically significant (Figure 5K, right). Consistently, the percentage of BLA<sup>Etv1</sup> significant neurons in the pro-social area was also significantly higher than chance level (Figure 5K). Among the three neural populations, the pro-social population of Etv1 were significantly different to chance level from both all and significant neuronal pool, while the pro-social population in the significant neurons of Lypd1 was even lower than the chance level (Figure 5J, K). Total distance moved during social tasks were similar across Cre lines (Fig S9I). Therefore, we confirmed the BLA<sup>Etv1</sup> neuronal activity preferring for social area beyond chance level. Together, these data revealed that a larger fraction of BLA<sup>Etv1</sup> neurons was recruited to the active ensemble for social.

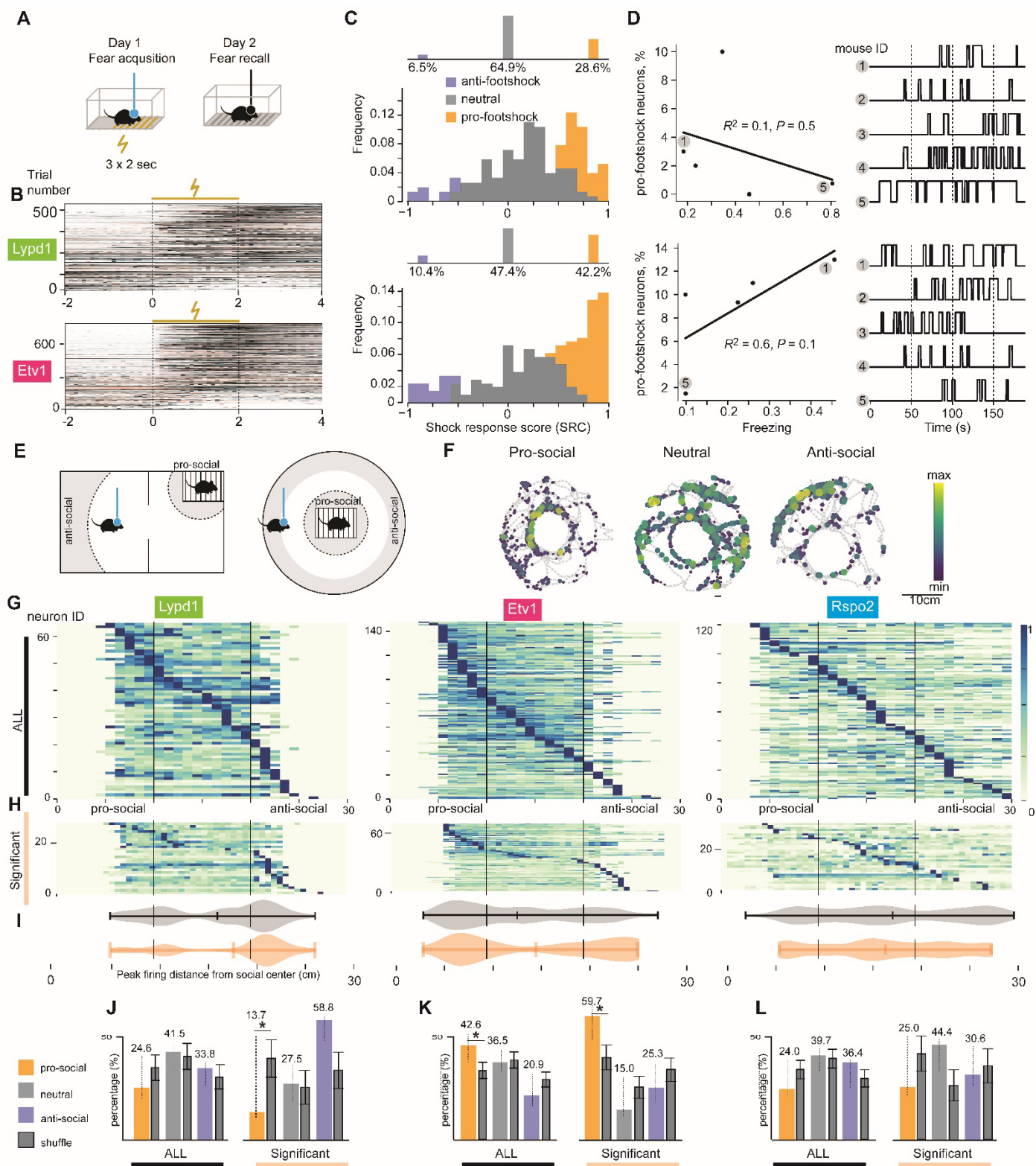


**Figure 5. Genetically- and spatially-defined neurons show different responses to aversive and social cues.**

(A) Scheme of contextual fear conditioning assay (CFC).

(B) Peri-stimulus time histogram (PSTH) illustrating the inferred spike trains from the calcium responses of the neurons recorded during the footshock session of CFC in *Lypd1* (top) and *Etv1* (bottom) mice. The vertical dashed line denotes the onset of foot shock stimulus lasting 2s indicated with a yellow line. The footshock trials were sorted by their footshock response score (see method for details) from top to bottom.

(C) Histogram of footshock response score (SRC) of neurons in the BLA *Lypd1* (top) and BLA *Etv1* (bottom) mice. The neurons whose activities are significantly correlated with footshock events were detected with a permutation test. Within these neurons, the ones with negative correlation (“anti-footshock” neurons) and positive correlation (“pro-footshock”) were colored in purple and orange respectively. The neurons which showed no significant correlation (“neutral”) were colored in gray. The percentages of pro/anti-footshock and neutral neurons are shown in the bar graph above the histograms.

(D) Scatter plots on the left show the relationship between the freezing frequency in the fear retrieval session (X axis) and the percentages of pro-footshock neurons (Y axis) observed in the fear acquisition session for *Etv1* (top) and *Lypd1* (bottom) mice (n= 5 mice each). The regression line fitted to the data is represented by the solid line, and the corresponding R<sup>2</sup> and p-values are indicated above. The plots on the right show the binarized freezing traces for each mouse (up: freezing, down: no freezing).

(E) Schemes of social interaction assays (two chamber assays with one conspecific in one chamber, or round chamber with conspecific in the center). Pro- and anti-social areas are indicated.

(F) Response maps of 3 example neurons whose activities are positively (labelled as pro-social), negatively (anti-social) or not correlated (neutral) with the distance to the mouse containing cage, indicated by the black circle. The gray lines indicate the mouse moving trajectories in the chamber. The size and the color of the dots indicate the firing rates of the selected neurons normalized by the maximum firing rate into the range of 0 to 1.

(G, H) Averaged firing rate heatmaps to social distance during the social interaction assay in all neurons (G) or in ‘significant’ neurons whose activity is significantly correlated with the distance to social chamber determined with a permutation test (H). Each row

corresponds to a neuron and each column represents a 1 cm distance bin. Pixel values represent the averaged firing rate of the corresponding neurons at the given distance to social chamber normalized by the peak average firing rate of each neuron. Vertical lines indicate the distance criteria for determining pro-social area and anti-social area. N = 64, 148 and 121 recorded BLA<sup>Lypd1</sup>, BLA<sup>Etv1</sup> and BLA<sup>Rspo2</sup> neurons, respectively.

(I) Violin plots of the peak firing distance of neurons (orange for significant neurons and gray for all neurons). Vertical lines for pro-social and anti-social areas.

(J-L) The percentage of the neurons whose firing rate peak in pro-social, neutral and anti-social area correspondingly in BLA<sup>Lypd1</sup> (J), BLA<sup>Etv1</sup> (K) and BLA<sup>Rspo2</sup> (L) populations. Percentage values are indicated in the top of each bar-graph. The significance at the 2.5% significance level in the comparison with the two tails of the null percentage distribution (shuffled) is indicated with an asterisk; shuffled data is shown with SD. The pools of either all neurons or significant neurons are indicated at the bottom of each bar graph.

#### 4.4.4 BLA<sup>Lypd1</sup> neurons promote normal food uptake.

The activation patterns of these BLA neurons suggested that they participated in valence-specific behaviors. We first asked, if optogenetic activation of these populations would be sufficient to promote appetitive behavior. We also employed optogenetic inhibition approaches to investigate, if one or more of these populations would be necessary to mediate appetitive behavior. We expressed channelrhodopsin-2 (ChR2) in all three Cre lines using a Cre-dependent viral vector (AAV5-Ef1-DIO-hChR2(H134R)-EYFP) bilaterally targeted to the BLA and implanted optical fibers bilaterally over the BLA for somata photostimulation (Figure 6A, B). Control mice received a similar AAV vector lacking ChR2 (AAV5-Ef1-DIO- EYFP). The feeding assay was the same as the one used for calcium imaging. Food consumptions during light-On and light-Off phases were measured on separate days using the same cohorts of mice. After 20h of fasting, photoactivated Lypd1-Cre;ChR2 mice consumed significantly more food than EYFP control mice and in comparison, to Light-off days (Figure 6C). This was in contrast to Etv1-CreER;ChR2 and Rspo2-Cre;ChR2 mice, which consumed significantly less food during the Light-On compared to the Light-Off phase (Figure 6C). The observed effects were independent of general locomotor behaviors (Fig.S10A). To acutely photoinhibit neurons, we expressed Cre-dependent Halorhodopsin (eNpHR3.0-mCherry) in a similar fashion as ChR2 and assessed food consumption. We found that photoinhibited, hungry Lypd1-Cre;eNpHR mice ate significantly less food than in the absence of photoinhibition (Figure 6D), while the same manipulation had no effect on Etv1-CreER;eNpHR and Rspo2-Cre;eNpHR mice. In summary, the activity of BLA<sup>Lypd1</sup> neurons is both sufficient and necessary to promote feeding. Activation of BLA<sup>Etv1</sup> or BLA<sup>Rspo2</sup> neurons can suppress feeding. However, these neurons may not be required for food uptake in the free-feeding assay.

We also assessed the intrinsic valence of optogenetic activation of the three types of BLA neurons in the neutral environment of a conditional place preference assay (CPP) (Figure 6E, see Methods). After conditioning, Lypd1-Cre;ChR2 mice exhibited a significant preference for the photostimulation-paired chamber, whereas Etv1-CreER;ChR2 and Rspo2-Cre;ChR2 mice showed significant avoidance behavior for the photostimulation-paired chamber (Figure 6E). No changes in anxiety were observed in Open-Field behavior (Fig.S10B). These results indicate that mice can learn to associate an open area with

positive valence for photoactivation of BLA<sup>Lypd1</sup> neurons and conversely, with negative valence for photoactivation of BLA<sup>Etv1</sup> or BLA<sup>Rspo2</sup> neurons.

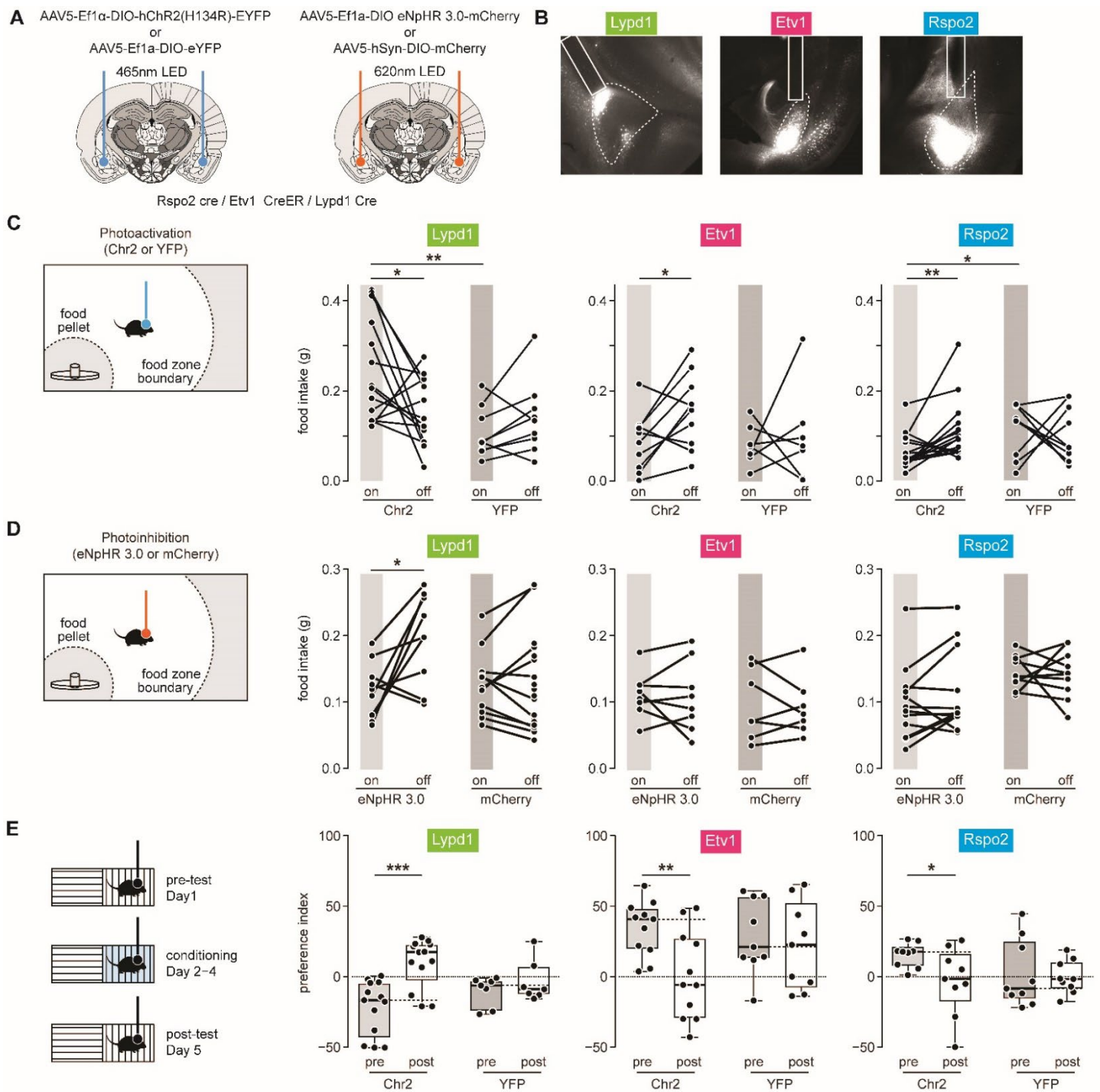


**Figure 6. BLA<sup>Lypd1</sup> neurons promote normal feeding behavior.**

A) Schemes of AAV injections and optic-fiber placements above Chr2- and eNpHR-expressing BLAs.

- B) Representative images of Chr2-eYFP expression in Rspo2, Etv1 and Lypd1-Cre mice with optic fiber locations.
- C) Left: Scheme of optogenetic activation during the free-feeding assay. Right: Food intake during optogenetic activation of three BLA populations compared to light off epochs and compared to photostimulated control groups. Lypd1 group: n = 14 (Chr2) and 9 mice (YFP) per group with two-tailed paired t test,  $t_{(13)} = 2.457$ ,  $p = 0.0288$  within Chr2 (on versus off) group. For Chr2-On versus YFP-On: two-tailed unpaired t test,  $t_{(21)} = 3.4$ ,  $p = 0.0027$  \* $p < 0.05$ , \*\* $p < 0.01$ . Etv1 group: n = 8 (Chr2) and 7 mice (YFP) per group with two-tailed paired t test,  $t_{(9)} = 2.492$ ,  $p = 0.0343$  within Chr2 group (on versus off) \* $p < 0.05$ . Rspo2 group: n = 18 (Chr2) and 9 mice (YFP) per group with Wilcoxon matched-pairs signed rank test,  $p = 0.0023$  within Chr2 (on versus off) group. For Chr2-On versus YFP-On: Kolmogorov-Smirnov test,  $p = 0.0226$ , \* $p < 0.05$ , \*\* $p < 0.01$ .
- D) Left: Scheme of optogenetic inhibition during the free-feeding assay. Right: Food intake during optogenetic inhibition of three BLA populations compared to light off epochs and compared to photostimulated control groups. Lypd1 group: n = 9 (eNpHR 3.0) and 11 mice (mCherry) per group with two-tailed paired t test,  $t_{(8)} = 2.771$ ,  $p = 0.0243$  within eNpHR 3.0 (on versus off) group) \* $p < 0.05$ . Etv1 group: n = 8 (eNpHR 3.0) and 7 mice (mCherry) per group. Rspo2 group: n = 13 (eNpHR 3.0) and 10 mice (mCherry) per group.
- E) Left: Scheme of conditioned-place preference experiment. Right: Preference index (cumulative time % in paired chamber – cumulative time % in unpaired chamber) of cohorts of mice combined with photostimulation of three BLA population before (pre) and after (post) conditioning. In case of Lypd1-Cre mice, the initially non-preferred chamber was paired with light, in case of Etv1-Cre and Rspo2-Cre mice, the initially preferred chamber was paired with light, to observe preference and avoidance, respectively. Lypd1 groups: n = 13 (Chr2) and 7 mice (YFP) per group; two-tailed paired t test,  $t_{(12)} = 4.528$ ,  $p = 0.0007$  within Chr2 group (pretest versus posttest)), \* $p < 0.05$ , \*\* $p < 0.01$ , \*\*\* $p < 0.001$ . Etv1 groups: n = 11 (Chr2) and 9 mice (YFP) per group; two-tailed paired t test,  $t_{(10)} = 3.273$ ,  $p = 0.0084$  within Chr2 group (pretest versus posttest). Rspo2 groups: n = 8 mice (Chr2 and YFP) per group; two-tailed paired t test,  $t_{(7)} = 2.695$ ,  $p = 0.0308$ , within Chr2 group (pretest versus posttest).



#### **4.4.5 BLA<sup>Etv1</sup> neurons are necessary for fear memory formation**

Given that BLA<sup>Etv1</sup> neurons were strongly activated by footshocks, we next asked if optogenetic manipulation of these neurons would affect the freezing response in a CFC experiment. On day 1 of CFC, footshocks were paired with either photoactivation or photoinhibition of the somata of BLA<sup>Etv1</sup> or BLA<sup>Lypd1</sup> neurons (Figure 7A, B). On day2 (Fear recall), the fraction of time the animals spent freezing was monitored. Photoactivation of Lypd1-Cre;ChR2 mice resulted in significantly less freezing than photoactivation of EYFP control mice, while similar levels of freezing were observed in Etv1-CreER;ChR2 mice compared to their respective EYFP control mice (Figure 7A). Conversely, photoinhibition of Etv1-CreER;eNpHR mice resulted in significantly less freezing on fear recall day compared to their respective mCherry control mice, while similar levels of freezing were observed in Lypd1-Cre;eNpHR mice compared to Lypd1-Cre;mCherry control mice (Figure 7B). The reduction in freezing of photoinhibited Etv1-CreER;eNpHR mice could already be observed during fear acquisition (day1) (Fig S10D). These results showed that BLA<sup>Etv1</sup> neurons are necessary for fear memory formation. They further indicate that BLA<sup>Lypd1</sup> neurons are sufficient to suppress freezing behavior.

#### **4.4.6 BLA<sup>Etv1</sup> neurons are necessary for social interaction**

Given that a large fraction of BLA<sup>Etv1</sup> neurons were activated during social behavior, we next asked, if optogenetic manipulation of these and other neurons would alter social behavior. Social behavior assays were performed as for calcium imaging experiments. Interestingly, photoactivation of Etv1-CreER;ChR2 mice resulted in mice spending more time in the social zone compared to the light-off phase, an effect that was not observed in control mice expressing YFP (Figure 7C). Instead, interactions of photoactivated Etv1-CreER;ChR2 mice with the empty cage were unaffected (Fig. S10E). The converse effect was observed in photoinhibited Etv1-CreER;eNpHR mice which spent significantly less time in the social zone compared to the light-off phase (Figure 7D). Neither optogenetic manipulation of BLA<sup>Lypd1</sup> nor BLA<sup>Rspo2</sup> neurons altered their social behavior, which was in



line with the observed neutral responses in the calcium imaging experiments. Together, these results showed that  $BLA^{Etv1}$  neurons encoded sociability and were sufficient and necessary to drive social interaction.

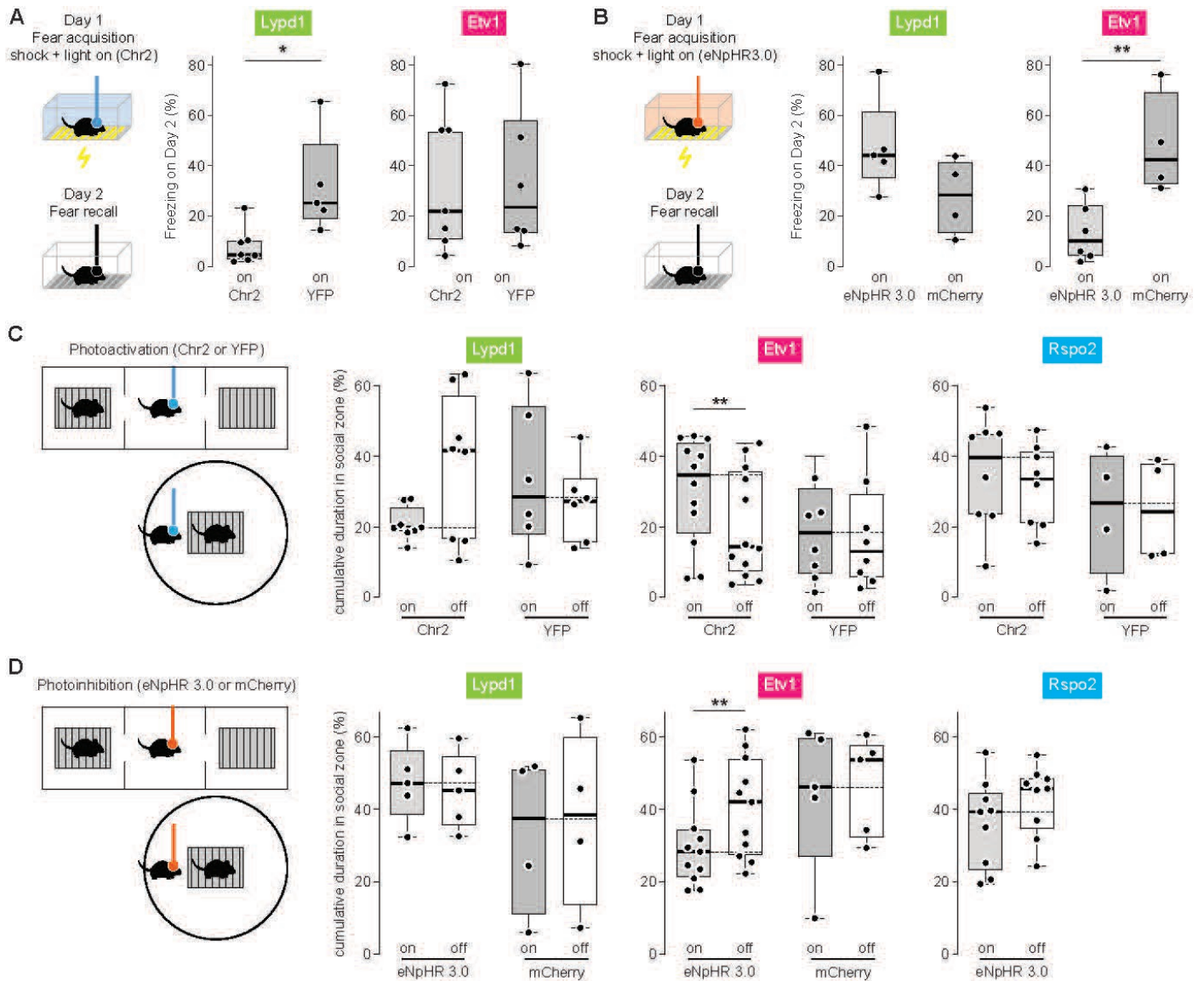


**Figure 7.  $BLA^{Etv1}$  neurons are necessary for fear memory formation and social interactions.**

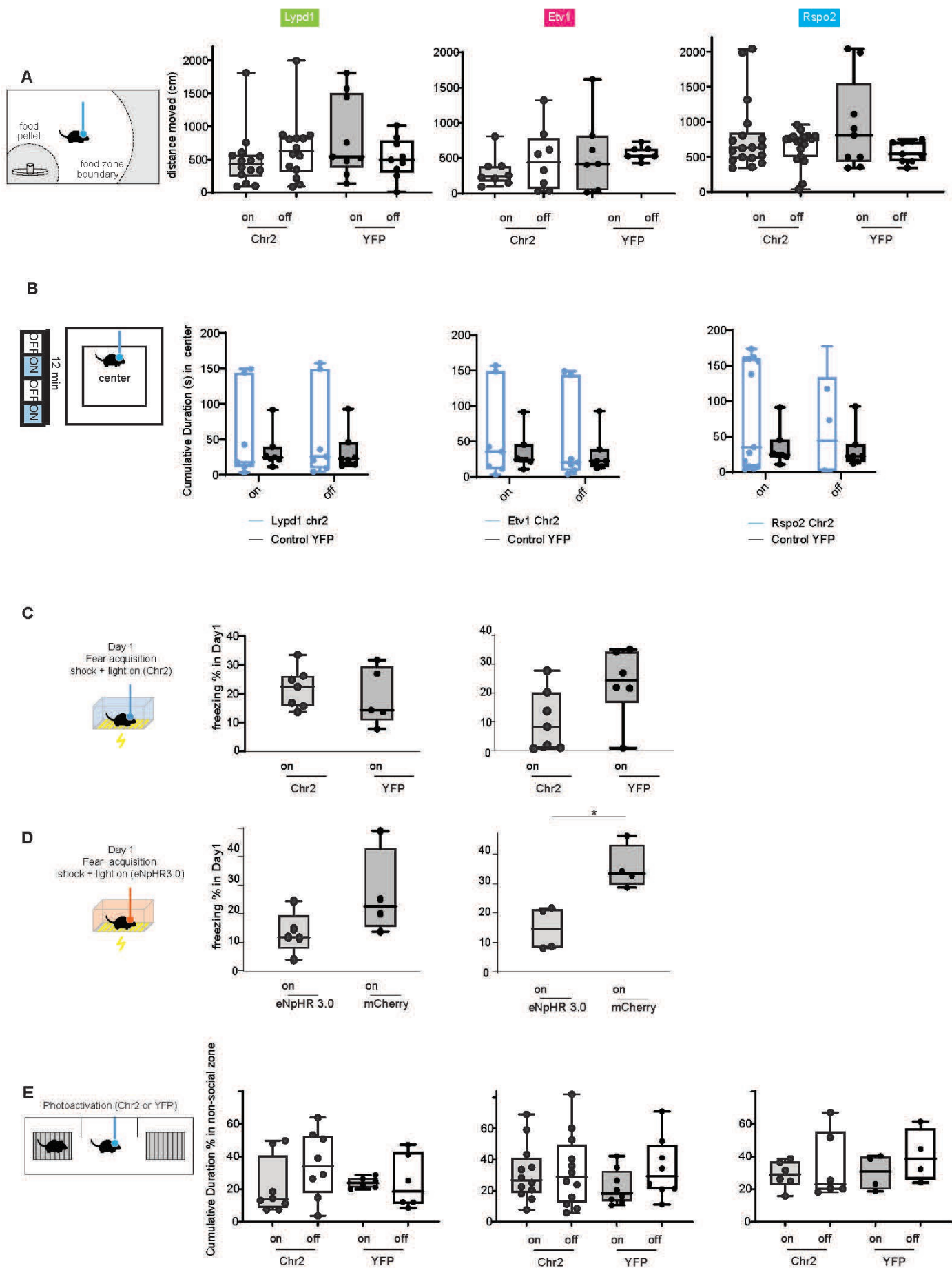
(A) Left: Scheme of contextual fear conditioning with photostimulation; day 1 with 3 times of footshocks (0.75mA) paired with light on. Freezing was measured on day 2 (fear recall). Right: Freezing behavior (%) on day 2 combined with photostimulation of two BLA

populations in comparison to controls. Lypd1 groups:  $n = 7$  (Chr2) and 5 mice (YFP) per group; Kolmogorov-Smirnov test,  $p = 0.0152$ ,  $*p < 0.05$ , Etv1 groups:  $n = 6$  (Chr2) and 7 (YFP) mice per group; Kolmogorov-Smirnov test,  $P = 0.9254$ .

(B) Left: Scheme of contextual fear conditioning with photoinhibition; Right: Freezing behavior (%) on day 2 combined with photoinhibition of two BLA populations in comparison to controls. Lypd1 groups:  $n = 5$  (eNpHR 3.0) and 5 (mcherry) mice per group; Kolmogorov-Smirnov test,  $p = 0.2857$ . Etv1 groups:  $n = 6$  (eNpHR 3.0) and 4 (mcherry) mice per group; Kolmogorov-Smirnov test,  $p = 0.0095$ ,  $**p < 0.01$ .

(C) Schemes of social interaction assays with photoactivation; Right: Cumulative duration in social zone (%) combined with photoactivation of three BLA populations in comparison to light-off epochs and controls. Lypd1 groups;  $n = 8$  (Chr2) and 6 mice (YFP) per group; two-tailed paired  $t$  test,  $t_{(7)} = 2.307$ ,  $p = 0.0544$  within Chr2 group (on versus off); Etv1 groups;  $n = 12$  (Chr2) and 8 mice (YFP) per group; two-tailed paired  $t$  test,  $t_{(11)} = 3.785$ ,  $p = 0.0030$ ,  $**p < 0.01$ , within Chr2 group (on versus off); Rspo2 groups;  $n = 6$  (Chr2) and 4 mice (YFP) per group; two-tailed paired  $t$  test,  $t_{(7)} = 0.6806$ ,  $p = 0.5180$ , within Chr2 group (on versus off).

(D) Schemes of social interaction assays with photoinhibition; Right: Cumulative duration in social zone (%) combined with photoinhibition of three BLA populations in comparison to light-off epochs and controls. Lypd1 mice,  $n = 5$  (eNpHR3.0) and 4 mice (mcherry) per group; Wilcoxon matched-pairs signed rank test,  $p = >0.9999$ , within eNpHR 3.0 group (on versus off); Etv1 mice,  $n = 11$  (eNpHR3.0) and 5 mice (mcherry) per group; two tailed paired  $t$  test,  $t_{(10)} = 3.19$ ,  $p = 0.0097$ ,  $**p < 0.01$ , within eNpHR 3.0 group (on versus off); Rspo2 mice,  $n = 9$  (eNpHR3.0) mice, Wilcoxon matched-pairs signed rank test,  $p = 0.6250$ , within eNpHR 3.0 group (on versus off).



**Supplementary. Figure S 10 related to figure6-7: motor or non-social or anxiety related behaviors did not change**

- A) Left: Scheme of free-feeding assay. Right: Total distance travelled in free-feeding assay combined with photoactivation (related to Figure 6C). Lypd1 group; n = 14 (Chr2) and 9 mice (YFP) per group with one-way ANOVA (Kruskal-Wallis test):  $p = 0.4126$ . Etv1 group; n = 8 (Chr2) and 7 mice (YFP) per group with one-way ANOVA (Kruskal-Wallis test):  $p = 0.2647$ . Rspo2 group; n = 18 (Chr2) and 9 (YFP) per group with one-way ANOVA (Kruskal-Wallis test),  $p = 0.5058$
- B) Left: Scheme of Open-field test (OFT) with light on (ON) and light off (OFF) illumination epochs. Right: cumulative duration (s) in center zone per 3 min of each epoch. Lypd1 groups; n = 7 mice in each Chr2 and YFP groups with two-way ANOVA group  $\times$  epoch interaction ( $F(1, 24) = 0.003498$ ,  $p = 0.9533$ ; Bonferroni *post hoc* analysis). Etv1 groups; n = 7 mice in each Chr2 and YFP groups with two-way ANOVA group  $\times$  epoch interaction ( $F(1, 24) = 0.05877$ ,  $p = 0.8105$ ; Bonferroni *post hoc* analysis). Rspo2 groups; n = 13 (Chr2) and 7 mice (YFP) per group with two-way ANOVA group  $\times$  epoch interaction ( $F(1, 36) = 0.2086$ ,  $p = 0.6506$ ; Tukey's multiple comparisons test, Bonferroni *post hoc* analysis). We only considered each 2<sup>nd</sup> ON and 2<sup>nd</sup> OFF epoch in order to avoid other behavioral contaminations.
- C) Freezing behavior (%) on Day 1 during CFC combined with photoactivation of BLA<sup>Lypd1</sup> or BLA<sup>Etv1</sup> neurons. The percentage of freezing was analyzed during 300s after 1<sup>st</sup> footshock offset: Lypd1 groups; n = 7 (Chr2) and 5 mice (YFP) per group with Kolmogorov-Smirnov test, ns ( $p = 0.4343$ ). Etv1 groups; n = 6 (Chr2) and 7 mice (YFP) per group with Kolmogorov-Smirnov test, ns ( $p = 0.0676$ ).
- D) Freezing behavior (%) on Day 1 during CFC combined with photoinhibition of BLA<sup>Lypd1</sup> or BLA<sup>Etv1</sup> neurons. The percentage of freezing was analyzed during 300s after 1<sup>st</sup> footshock offset: Lypd1 group; n = 4 mice per each eNpHR 3.0 and mcherry group with Kolmogorov-Smirnov test,  $p = 0.2857$ . Etv1 group; n = 4 mice per each eNpHR 3.0 and mcherry group with Kolmogorov-Smirnov test,  $p = 0.0286$ ,  $*p < 0.05$ .
- E) Left: Scheme of social interaction assay. Right: Cumulative duration (%) in non-social zone combined with photoactivation of three BLA populations in the social assay in comparison to light-off epochs and YFP controls. Lypd1 group; n = 8 (Chr2) and 6 mice (YFP) per group with one-way ANOVA (Kruskal-Wallis test; Bonferroni *post*

*hoc* analysis), ns ( $p=0.2574$ ). Etv1 group;  $n=12$  (Chr2) and 8 mice (YFP) per group with one-way ANOVA (Kruskal-Wallis test; Bonferroni *post hoc* analysis), ns ( $p=0.0407$ ). Rspo2 group;  $n=6$  (Chr2) 4 mice (YFP) per group with one-way ANOVA ((Kruskal-Wallis test; Bonferroni *post hoc* analysis), ns ( $p=0.6801$ )).

## **4.5 GO terms and comparison with published data supported our transcriptional, anatomical and functional populations in BLA**

In this study, we confirmed that our transcriptional and anatomical marker genes identified cell populations. Moreover, this could be the cell types for different valence coding neurons connected with other brain region differently as proved in previous studies (Duvarci & Pare, 2014; Felix-Ortiz et al., 2013; Felix-Ortiz & Tye, 2014; Huang et al., 2020; LeDoux et al., 1990; Morrison & Salzman, 2010; Peng et al., 2015; SAH et al., 2003; Tye et al., 2011). Hence, we hypothesized these functional differences have been hard wired in transcriptional level. Therefore, we checked Gene Ontology (GO) terms, relevant for functional roles, such as specific behaviors and memory (See methods). We confirmed behavior specific genes, such as aggressive or observational learning or feeding, differently expressed across clusters (Figure S 11A). For example, feeding behavior genes were higher in pBLA (Otof/Cdh13) cluster, while defensive behaviors including fear or pain response and aggressive behavior genes, were higher much in aBA (Rspo2/Etv1/Adamts2/Bdnf) and acBA (Etv1/Lypd1) clusters. Taken together, GO enrichment analysis across these clusters illustrated that functionally relevant genes differently expressed (Figure S 11A) and this again supported our functional results; Rspo2 and Etv1 neurons for negative valence, but Lypd1 neurons for positive valence (Figure 4-7).

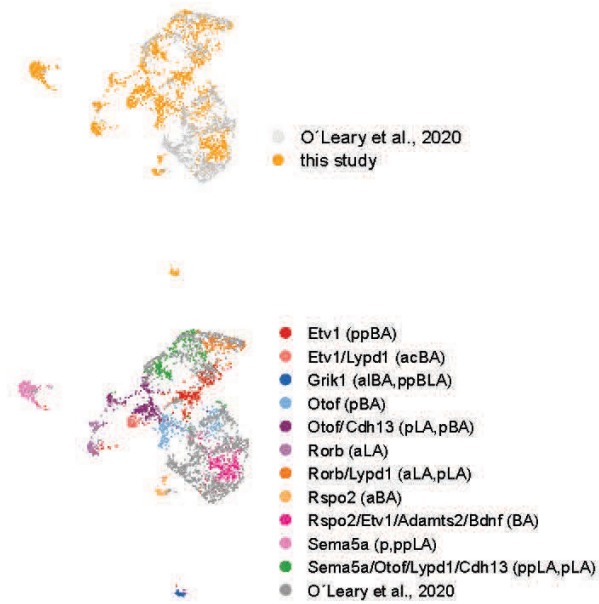
To confirm our transcriptional clusters; as “cell type” in BLA, we integrated BLA-derived excitatory neurons from our data and a published data (O’Leary et al., 2020) and then connected clusters one each from different datasets. Most of our clusters were matched with the published clusters by following well their anatomical expression (Figure S 11B). For

example, our Sema5a/Otof/Lypd1/Cdh13(ppLA,pLA) cluster matched mainly with LA2 while Rorb/Lypd1 (aLA,pLA) cluster showed similarity with LA1 (Figure S 11B). On the other hand, BA clusters: aBA(Rspo2/Etv1/Adamts2/Bdnf) , acBA (Etv1/Lypd1) and pBA (Otof) cluster were closely matched with BA specific clusters (BA1-4), especially with BA1 (Figure S 11B). Therefore, both datasets are confirmed that there must be different cellular composition between LA and BA in BLA.

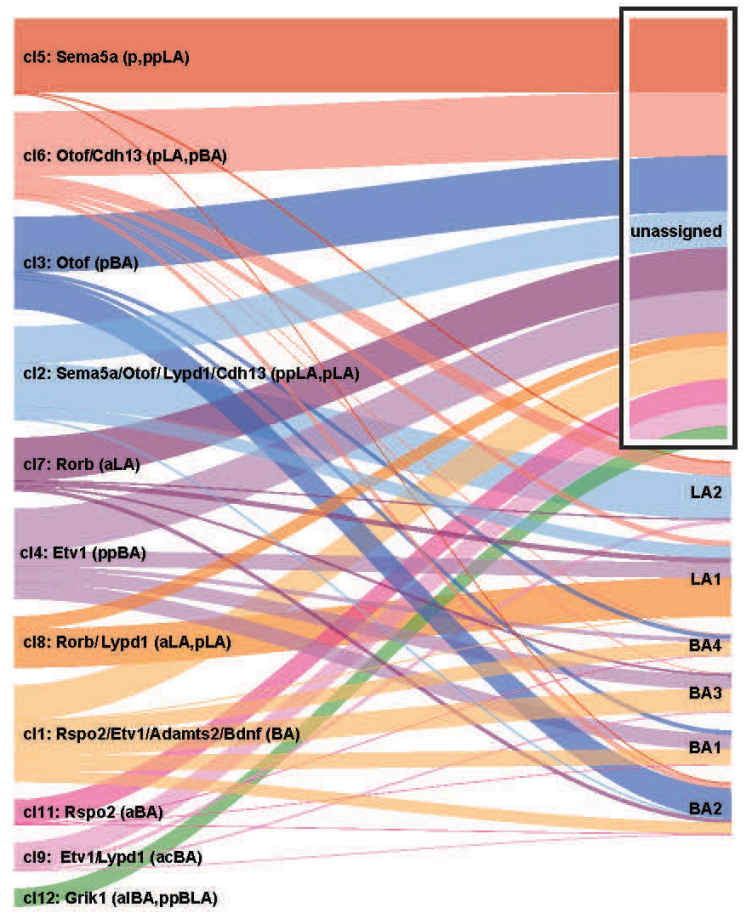
However, we found undefinable cells existing only in our dataset, written as “unassigned” (Figure S 11B). As was harvested the published data from scRNA seq but our one from snRNA seq, it is possible the difference from technical batch effect. However, a main reason for the clusters only existing in our data might be because biologically we collected more longitudinally in anterior posterior axis. Specifically, we have observed posterior-specific clusters, including Otof/Cdh13 (pLA,pBA) and Sema5a(pLA), and anterior- specific clusters, including Rorb (aLA), which exclusively exist in our dataset and likely represent the very posterior or very anterior BLA that was not included in the published data (Figure S 11B).



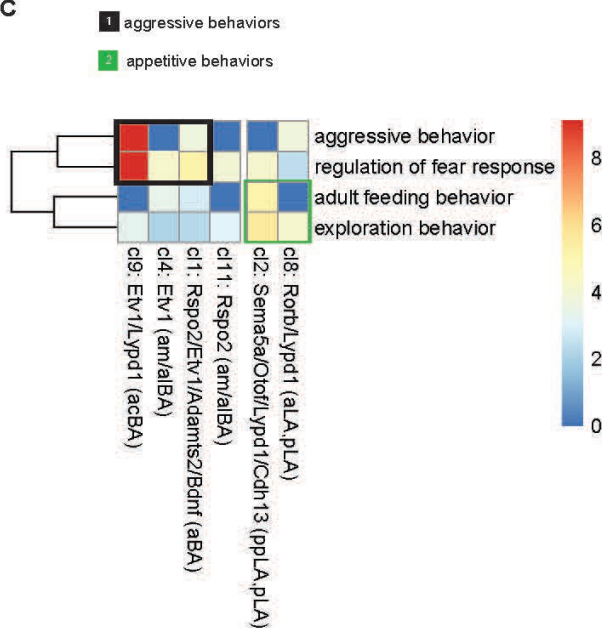
A



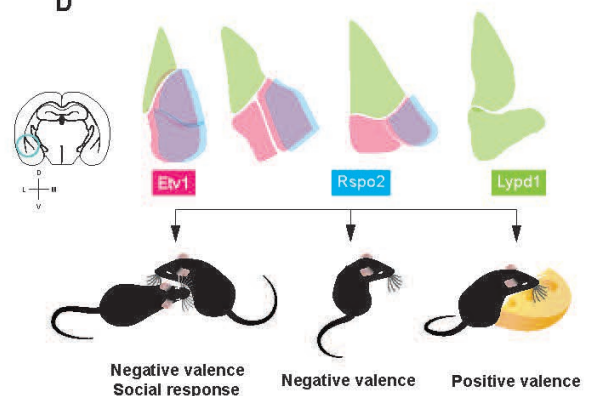
B



C



D



**Supplementary. Figure S 11 related to discussion: Comparison with published data and GO terms supported our transcriptional, anatomical and functional populations in BLA**

- A) UMAP of glutamatergic BLA neurons from published data 14 aligned with our glutamatergic BLA clusters (top: cells aligned from both datasets; published data (grey) and our data (yellow), bottom: clusters of our dataset in different colors, published data in grey).
- B) UMAP of glutamatergic BLA neurons from published data 14 aligned with our glutamatergic BLA clusters (top: cells aligned from both datasets; published data (grey) and our data (yellow), bottom: clusters of our dataset in different colors, published data in grey).
- C) Gene ontology (GO) enrichment analysis on 6 glutamatergic clusters: Enrichments of cluster marker genes within selected GO terms (valence related behavior terms).  
  
(scale bar indicates odds ratio).
- D) Schematic drawing of three different neuronal types in BLA with their distinct spatial expression pattern across the anterior-posterior extent of the BLA (from left to right) and encoding positive, negative or mixed negative/social valence.



# Discussion

## 5.1 Summary of thesis findings

Here, we described the multimodal identification of neurons in the BLA with transcriptional, molecular, and functional profiling using snRNA sequencing, smFISH, optogenetics, and calcium imaging. Together these findings describe the rich diversity of glutamatergic cell types and their spatial distribution in the BLA, and support the concept that genetically-defined subpopulations respond either to valence-specific or mixed cues, and expand their behavioral output to the promotion of normal feeding and social behavior.

## 5.2 The similarity of GABAergic interneurons between cortex and BLA

The GABAergic interneurons within the BLA have received comparatively less transcriptional scrutiny owing to their sparse and numerically inferior population in contrast to their glutamatergic counterparts (Beyeler and Dabrowska 2020). However, our investigation has revealed the presence of 10 discernible transcriptional GABAergic clusters, demonstrating analogous transcriptional profiles to those found in the cortex, characterized by canonical cortical interneuron markers (Tasic et al. 2016; Tremblay, Lee, and Rudy 2016). This lends support to the notion that the BLA shares a closer transcriptomic affinity with the cortex rather than with areas such as the central amygdala (CeA) or other nuclei comprising the amygdala complex. Notably, clusters positive for *Reln* and *Ndnf*, which are distinct from other interneuron subtypes like *SST* and *PV*, have been the subject of comparatively fewer investigations within the BLA. Recently, neurons expressing *Ndnf* in the cortex have been scrutinized for their specific localization in layer 1,

particularly for their role in disinhibiting SST-expressing neurons in the context of fear-related information processing (Abs et al. 2018). Consequently, this distinctive transcriptional attribute of the *Ndnf* cluster within the BLA may suggest the presence of undefined interneuron subtypes, potentially serving to disinhibit other interneurons and thereby modulate diverse information circuits in the BLA.

### 5.3 Molecularly-defined glutamatergic BLA cell types

The major neuronal population in the BLA is glutamatergic projecting neurons. Several previous studies have identified and separated LA versus BA molecularly (O'Leary et al. 2020) or functionally, and anterior versus posterior BA (Kim et al. 2016; Zhang et al. 2021). In BLA, the causal relationship between cell types and projections in various behaviors were uncovered previously (Janak and Tye 2015; Kim et al. 2016; Zhang et al. 2021). However, the specific behavioral functions associated with these cell types have not been extensively characterized at this level of detail. Recent studies utilizing RNA sequencing techniques have reported contradictory findings regarding the involvement of molecularly defined neurons in valence-based coding, introducing a need for further investigation (Kim et al. 2016; Zhang et al. 2021). While the studies examining reward and punishment processing within the same BLA subregion have yielded opposing results, underscoring the potential existence of additional molecular or anatomical subdivisions within the BLA to reconcile these conflicting studies (Beyeler et al. 2018; Jin et al. 2021; Zhang et al. 2021, 2020). The newly identified BLA neuronal subtypes, along with their subregion-specific marker gene expressions in our study, offer a valuable resource for exploring how different cell types participate in the functional circuitry of the BLA. Furthermore, our GO enrichment analysis provides additional support for this notion, suggesting unique functions of genes expressed across various cell types (Figure S11A). Specifically, for decades it has been known that the LA is characterized as an information-receiving hub, while the BA functions as an information-transmitting center (Duvarci and Pare 2014; Lanuza et al. 1998; LeDoux et al. 1990; Morrison and Salzman 2010; Nader, Schafe, and le Doux 2000; Tye et al. 2011). In line with this, our own analysis revealed discrete clusters that segregate LA (predominantly comprising *Cdh13*, *Rorb*, and *Lypd1* expressing neurons) from BA (primarily containing *Rspo2* and *Etv1* expressing cells). However, our finding that LA neurons, BLA

Lypd1 population, are vital for feeding behavior opened the possibility of other roles of LA, not only as an information-receiving hub.

## 5.4 Spatial organization of glutamatergic BLA clusters

Our investigation has illuminated the spatial demarcation between molecularly defined cell types within the BLA, aligning with an anatomical partitioning into eight distinct subregions (am, al, ac, p, ppBA, and a, p, ppLA). This revelation underscores a fundamental distinction in the cellular composition across these BLA subdivisions. In our correlation analysis, while the overall correlation pattern among our marker genes remained relatively consistent between transcriptomics and smFISH data (Figure S5), minor discrepancies in the correlation of marker genes were observed, possibly stemming from technical or biological distinctions. From a technical standpoint, this variation could be attributed to the combination of marker genes used to identify transcriptional clusters while in smFISH data, we used cells expressing a single gene for analysis. Additionally, biological differences, such as the source of mRNA (solely from nuclei in snRNA sequencing or from both nuclei and cytoplasm in smFISH), may contribute to these disparities. For instance, *Adamts2* and *Bdnf* exhibited sparse expression in snRNA data, whereas in the spatial approach, these genes demonstrated clear and localized expression patterns. In our study, we have confirmed subregion-specific parcellation of transcriptional clusters in the ventral-dorsal, anterior-posterior, and medial-lateral extent through multimodal approaches. This finding adds to the growing body of evidence from previous studies that have shown differences in morphologies across sub-nuclei (McDonald 1984b; SAH et al. 2003) and firing patterns of neurons (SAH et al. 2003), as well as in connectivity with other brain regions (Beyeler et al. 2018; Hintiryan et al. 2021) and in functional circuits (Jin et al. 2021; Kim et al. 2016; Zhang et al. 2021). Our spatial-transcriptional study offers a valuable tool for exploring specific parts of this brain region and understanding the complex networks it forms.

## 5.5 Putative additional functions of marker gene-identified neuronal populations

In this study, transcriptional clusters exhibited differential expression of genes related to functionally or behaviorally relevant GO terms (Figure S 11A). Notably, clusters specific to

the BLA regions displayed differential expression of GO terms associated with valence-specific behaviors such as aggression, fear, and feeding, as well as social-related behaviors like observational learning and parental behaviors. This GO enrichment analysis is consistent with our functional experiments revealing valence-specific neuronal populations in the BLA (Figure 4-7). Although the GO terms of 10 marker genes were not directly associated with particular behaviors, certain genes were found to be part of behavior-related GO classes: *Bdnf* (brain-derived neurotrophic factor) in behavioral fear response, *Rspo2* (R-spondin 2) in response to stimuli, or to cell connectivity related GO classes: *Cdh13* (cadherin 13) in cell adhesion, *Sema5a* (Semaphorin 5A) in negative regulation of axon extension, or to synaptic activity GO classes: *Lypd1* (Ly6/Plaur domain containing 1) in acetylcholine receptor inhibitor activity, *Grik1* (glutamate receptor, ionotropic, kainate 1) in ionotropic glutamate receptor activity, or to transcription related GO classes: *Rorb* (RAR-related orphan receptor beta) in DNA-binding transcription factor activity, *Etv1* (ets variant 1) in cell differentiation. Together, this suggests that the various genes expressed in various cell types may determine the positioning of cells in the BLA and the specific connectivity with other brain regions for specific functional purposes. Although the exact genes for this hard-wired program or for the fate of cells remain unknown, future studies utilizing transcriptomics and genetic mutations, such as knock-out or knock-in techniques, may provide answers.

## 5.6 Activity profiles of three transcriptionally and anatomically defined neurons during fasting and re-feeding

Prior research has established that the brain processes negative and positive information in distinct regions, including the medial amygdala (Choi et al. 2005), cortical amygdala (Root et al. 2014), gustatory cortex (Peng et al. 2015), and the BLA (Goosens and Maren 2001; Kantak et al. 2002; Kim et al. 2016). In our study, we benefitted from using precise markers based on genetic and anatomical characteristics to target specific cell types and to track and analyze neuronal activity in a cell type-specific manner. However, we still observed variability of neuronal activity even within specific populations identified by a marker gene. For instance, although we found the BLA <sup>Lypd1</sup> population as a positive encoding neuron type, a subset of neurons in the BLA<sup>Lypd1</sup> exhibited inhibitory responses

during feeding while the majority of the BLA<sup>Lypd1</sup> exhibited excitatory responses (Figure 4). Additionally, a part of the BLA<sup>Lypd1</sup> population also showed excitatory responses during freezing and the subset of BLA<sup>Etv1</sup> or BLA<sup>Rspo2</sup>, which we found as negative encoding, also showed activation during feeding. Similar to a recent study that highlighted functional diversity in pBLA neurons projecting to CeA (Massi et al. 2023), it is likely that there may be additional functional, genetic, morphological or structural distinctions even within one genetically identified neuron type. Other genetic marker genes apart from *Rspo2*, *Etv1* and *Lypd1*, were found in our transcriptional and anatomical dataset. However, they were not further investigated for functionality in this study. Therefore, we propose that future research could use other marker genes to discover subpopulations. Also, the reverse approach to first imaging the neuronal activity for a specific behavior followed by profiling the transcriptome of each neuron, might give more comprehensive and less supervised data about the cellular and molecular diversity of the neuronal circuit.

## **5.7 The distinct neuronal responses of BLA<sup>Rspo2</sup> and <sup>Etv1</sup> neurons for negative, *Lypd1* neurons for positive valence, but BLA<sup>Etv1</sup> neurons uniquely for social valence.**

Despite the heterogeneity within the three populations, the majority of BLA<sup>Lypd1</sup> neurons were found to be activated during metabolic reward (feeding) but inhibited during footshock. On the other hand, the largest population in BLA<sup>Etv1</sup> or <sup>Rspo2</sup> neurons was found to be inhibited during feeding but activated for negative stimuli (Figure 4-5). Additionally, even if the three neuronal populations have subsets and heterogeneity encoding different neuronal activities for valence stimuli, in support of the concept of “winner takes all”, optogenetic manipulation experiments demonstrated that activation of BLA<sup>Lypd1</sup> neurons increased feeding behavior and showed preference for the contextual place task but impaired fear memory. Conversely, inhibition of BLA<sup>Lypd1</sup> neurons led to a decrease in feeding. Our findings are consistent with previous studies that suggest a role of the pBLA in reward conditioning (Kantak et al. 2002; Kim et al. 2016; Kim et al. 2017).

On the contrary, the majority of BLA<sup>Etv1</sup> or BLA<sup>Rspo2</sup> neurons were found to be inhibited during feeding, but activated during footshock, and optogenetic activation of negative

valence neurons, BLA<sup>Etv1</sup> or Rspo2, led to a decrease in feeding and avoidance in the contextual place task. However, inhibiting these neurons did not result in any changes in feeding behavior. This suggests that deactivating the negative valence circuit does not necessarily promote positive valence, as previously suggested (Kim et al. 2016). Our previous study on CeA has shown that CeA<sup>Htr2a</sup> neurons play a crucial role in converging multiple appetitive routes, rather than BLA (Douglass et al. 2017). Therefore, we propose that BLA<sup>Etv1</sup> and Rspo2 may indirectly modulate food consumption by evaluating valence and sending the information to CeA rather than directly affecting metabolic circuits.

### **BLA<sup>Etv1</sup> neurons show a mixed response pattern to social and aversive cues**

We have made an unexpected discovery regarding cell type-specific valence coding in social environments. Our finding revealed that populations activated by aversive stimuli, such as BLA<sup>Etv1</sup> and BLA<sup>Rspo2</sup>, display different responses during social interaction. Specifically, while more BLA<sup>Etv1</sup> neurons are activated, BLA<sup>Rspo2</sup> neurons do not exhibit a response to social stimuli. Interestingly, BLA<sup>Lypd1</sup> neurons which are associated with positive valence, showed inhibitory responses during social interaction. Notably, optogenetic activation and inhibition of BLA<sup>Etv1</sup> neurons showed bidirectional effects on social interaction. These results support prior research indicating that social valence is distinct from other forms of valence and is contingent on various internal conditions, such as social isolation (Ferrara et al. 2022; Matthews et al. 2016), hunger (Tomova et al. 2020) or external stress (Ferrara, Trask, and Rosenkranz 2021; Folkes et al. 2020; Kim et al. 2022) or age (Douglas, Varlinskaya, and Spear 2004). However, the precise modulation of social interaction circuits by internal status remains unclear. Earlier studies have presented conflicting results. For example, the activation of the projection from BLA to NAc leads to social deficits (Folkes et al. 2020) and the activation of projections from BLA to vHPC leads to both anxiety and social deficits (Felix-Ortiz and Tye 2014), while the activation of the aversive valence engram in mPFC projecting to BLA resulted in decreased sociability (Huang et al. 2020). Hence, the impact of BLA engagement on social circuits remains uncertain. However, our findings offer a potential explanation for social valence within the BLA in line with the concept of "goal-oriented behavior". We speculate that the drive for social interaction may be goal-oriented (Roy F. Baumeister 2007) not by valence. In line

with this, using optogenetic activation, we found that activating BLA<sup>Etv1</sup> neurons promoted social preference. However, in the absence of a social target such as the novel object, approach to this object was not changed (Fig. S10). Even in context place tasks, mice avoided optogenetic activation paired place, suggesting that stimulation of BLA<sup>Etv1</sup> neurons is felt as aversive. This raises the possibility that a negative-affective state driven by the activity of BLA<sup>Etv1</sup> neurons motivates the animal to seek social contact as a compensatory mechanism. In summary, our study supports a concept that social behavior is not determined by innate valence mechanisms, like anxiety or defensive and appetitive behaviors. Instead, it may be regulated by a balancing system that maintains homeostasis of the internal state (So et al. 2015).

In addition to the internal state modulation scenario, neuroendocrine factors have been identified as an alternative regulatory network for behavioral modulation in BLA, including oxytocin (Takayanagi et al. 2017) and vasopressin (Meyer-Lindenberg et al. 2011) for social behaviors. A recent study also highlighted the role of secretin, a classical gut-peptide hormone, in BLA neurons, particularly in the anterior basal amygdala, mediating social behaviors (Wei et al. 2023). It remains to be investigated if BLA<sup>Etv1</sup> neurons overlap with various neuroendocrine-releasing or receptor-expressing neurons involved in social modulation.

## **The differences between two negative valence neurons**

The different neuronal activities observed in BLA<sup>Rspo2</sup> and BLA<sup>Etv1</sup> neurons for valence may be due to the non-overlapping cells between these two populations while the overlapping cells, the larger fraction of both cell types, are engaged in consistently negative valence coding. The expression pattern of BLA<sup>CCK</sup> projection neurons to NAc, driving depression-like behaviors (Shen et al. 2019) showed similarity to BLA<sup>Rspo2</sup> neurons to NAc (Kim et al. 2016). Therefore, it is possible that BLA<sup>Rspo2</sup> influences depression rather than loneliness-like behavior associated with BLA<sup>Etv1</sup> neurons. Also, in our analysis of neuronal activity based on distance, BLA<sup>Rspo2</sup> neurons demonstrated higher activity at a moderate distance from social conspecifics (Figure 5). Furthermore, our optogenetic manipulation of BLA<sup>Rspo2</sup> neurons during social tasks (Figure 7) did not yield any discernible changes in behavioral responses. This suggests that BLA<sup>Rspo2</sup> neurons may be temporally phasic-

specific. During the transitional phase, such as mouse is moving toward a social conspecific from other behaviors, BLA <sup>Rspo2</sup> neurons represented the highest firing rates (Figure 5). Hence, the firing of BLA <sup>Rspo2</sup> neurons during the shifting period could potentially indirectly or directly activate BLA <sup>Etv1</sup> neurons, which directly promote social interaction at the end. This is in line with a prior study demonstrating that a subpopulation of neurons exclusively triggers consummatory behaviors when the neurons are activated only during mice initiate approaching behaviors as opposed to continuous stimulation (Lee et al. 2023). While our study did not directly investigate this hypothesis, future research employing behavioral and imaging setups with enhanced temporal resolution to target discrete specific temporal windows along with simultaneous imaging and manipulation on two populations such as in close-loop manipulation, could shed light on the direct and indirect effects of social motivation by observing neuronal activity during the temporal transition and action phases.

Additionally, prior research has indicated that BLA-to-NAc projections are implicated in positive behaviors (Alexander, Muller, and Mascagni 2002; Paton et al. 2006). However, a recent study has controversially proposed that these same projections mediate social avoidance (Folkes et al. 2020). This suggests that projections to the same region may encode valence and social coding inconsistently. To address this heterogeneity even within seemingly uniform cell types or within the same projection target, research incorporating "cell type-specific" and "connectivity" approaches could be highly beneficial.

Finally, due to the controlled environment in a wired cage of the social conspecific, a detailed analysis for behavioral ethogram like attack, mounting, or allo-grooming, was not conducted in this study. Nevertheless, we used juveniles as conspecifics following a social affective preference (SAP) test, where experimental animals displayed an inclination to approach stressed juveniles but avoid stressed adult conspecifics (Djerdjaj et al. 2022; Rogers-Carter et al. 2019). This led us to believe that the interactions observed were more reflective of affective social engagement rather than other forms of social behaviors. Nonetheless, during social interaction, neurons within each specific population exhibited heterogeneous activities, suggesting the potential existence of subpopulations encoding specific behavioral ethograms differently. Therefore, the analysis of neuronal activity upon specific behavioral ethograms could elaborate the function of BLA neuron types for social behaviors.



## 5.8 Future Experiments

Our research has identified the spatial transcriptomic populations of glutamatergic neurons in the BLA and has identified three neuronal types that are differently engaged in valence coding. Fortunately, recent global transcriptomics studies targeting the whole brain and across different species have been conducted (Hochgerner et al. 2022; Tasic et al. 2016; Tosches et al. 2018; Yao et al. 2023; Yu et al. 2023), and are accessible from [Brain Cell Data Center \(BCDC\) \(biccn.org\)](https://brainiac.biccn.org/). While this research provides resources for further studies targeting specific genes or seeking marker genes to annotate cell types overall, studies with deeper analysis for a specific brain region are still required to uncover subregional differences or to reveal sparse but important genetic profiles. Therefore, our work can be used in future studies to access BLA neuronal types that are spatially distinguishable to target micro-subregions using transgenic Cre mice and to manipulate specific genes only in the BLA.

Furthermore, two previous studies demonstrated an anteroposterior topography of BLA *Rspo2* and *Ppp1r1b* neurons (Kim et al. 2016) having BLA-NAc and BLA-CeA projections, respectively. However, this finding was contrary to another study showing intermingled occupation of those projection neurons (Beyeler and Dabrowska 2020). This discrepancy may be attributed to the exclusion of the LA in the study that found anteroposterior topography (Kim et al. 2016). The neuronal populations in our study encompassed the entire BLA in mediolateral, dorsoventral, and anteroposterior dimensions. Hence, our research has the potential to explain discrepancies of previous studies. Also, the resource we are providing on the spatial location of transcriptional clusters could be combined with tracing techniques to investigate the distinct or common connections to other brain regions. This would ultimately validate the interconnected pathways between local circuits of BLA and global connectivity. Future studies in combination with novel technical tools should address the diversity within apparently homogeneous local populations at different levels (from transcriptional/molecular until behavioral level) .

# Abbreviations

ABRREVIATION	DEFFINITION
AB	accessory basal
AOD	acousto-optic deflector
AAV	adenoassociated viruses
ATP	Adenosine triphosphate
AMPA	$\alpha$ -am+ A1:B72ino-3-hydroxy-5-methyl-4-isoxazolepropionic acid
ANOVA	Analysis of variance
ACR	anion channel rhodopsins
ACSF	artificial cerebrospinal fluid
AC	auditory cortex
ASD	autism
BA	Basal amygdala
B	Basal amygdala
BM	Basomedial amygdala
BMA	Basomedial amygdala
BNST	bed nucleus of the stria terminalis
CGRP	Calcitonin gene-related peptide
CGE	Caudal Ganglion Eminence
CEA	Central amygdala
CCK	cholecystokinin
CFC	Conditional Fear conditioning
CPP	Conditioned place preference

CRH	Corticotrophin-releasing hormone
DE	Differential expression
DEG	differently expressed gene
DIO	Double floxed inverted open reading frame
EYFP	Enhanced yellow fluorescent protein
EDTA	Ethylenediaminetetraacetic acid
GABA	gamma amino-butyric acid
GO	Gene ontology
GECI	Genetically encoded calcium indicators
GRIN	gradient index
HCR	Hairpin chain reaction
NpHR	Halorhodopsin
IL	infralimbic
IPSC	inhibitory postsynaptic current
ITC	intercalated cells
IP	intraperitoneal
LA	Lateral amygdala
LGE	Lateral ganglion eminence
LED	Light emitting diode
ME	Medial amygdala
NGE	Medial ganglion eminence
NGEM	Nanoliterscale Gel Beads-in-emulsion
NAC	nucleus accumbens
NA	numerical appetite
OFT	Open field task

PVT	paraventricular nucleus of the thalamus
PSTH	peri-stimulus time histogram
PBS	phosphate-buffered saline
PA	Posterior amygdala
PPBA	Posterior-Posterior basal amygdala
PPLA	Posterior-Posterior Lateral amygdala
PFC	prefrontal cortices
PCA	Principal component analysis
PKCD	protein kinase C $\delta$
ROI	region of interest
SCT	secretin
SMFISH	Sequential multiplexed (multi-florescent) in situ hybridization
SNN	shared nearest neighbor
SST	Somatostatin
SD	Standard Deviation
UMAP	Uniform Manifold Approximation and Projection

# References

- Abs, Elisabeth, Rogier B. Poorthuis, Daniella Apelblat, Karzan Muhammad, M. Belen Pardi, Leona Enke, Dahlia Kushinsky, De-Lin Pu, Max Ferdinand Eizinger, Karl-Klaus Conzelmann, Ivo Spiegel, and Johannes J. Letzkus. 2018. 'Learning-Related Plasticity in Dendrite-Targeting Layer 1 Interneurons'. *Neuron* 100(3):684-699.e6. doi: <https://doi.org/10.1016/j.neuron.2018.09.001>.
- Ambroggi, Frederic, Akinori Ishikawa, Howard L. Fields, and Saleem M. Nicola. 2008. 'Basolateral Amygdala Neurons Facilitate Reward-Seeking Behavior by Exciting Nucleus Accumbens Neurons'. *Neuron* 59(4):648–61. doi: <https://doi.org/10.1016/j.neuron.2008.07.004>.
- Ashwin, Chris, Simon Baron-Cohen, Sally Wheelwright, Michelle O'Riordan, and Edward T. Bullmore. 2007. 'Differential Activation of the Amygdala and the "Social Brain" during Fearful Face-Processing in Asperger Syndrome'. *Neuropsychologia* 45(1):2–14. doi: <https://doi.org/10.1016/j.neuropsychologia.2006.04.014>.
- Balleine, Bernard W., and Simon Killcross. 2006. 'Parallel Incentive Processing: An Integrated View of Amygdala Function'. *Trends in Neurosciences* 29(5):272–79. doi: <https://doi.org/10.1016/j.tins.2006.03.002>.
- Barretto, Robert P. J., Bernhard Messerschmidt, and Mark J. Schnitzer. 2009. 'In Vivo Fluorescence Imaging with High-Resolution Microlenses'. *Nature Methods* 6(7):511–12. doi: 10.1038/nmeth.1339.
- Baxter, Mark G., and Elisabeth A. Murray. 2002a. 'The Amygdala and Reward'. *Nature Reviews Neuroscience* 3(7):563–73. doi: 10.1038/nrn875.
- Belova, Marina A., Joseph J. Paton, Sara E. Morrison, and C. Daniel Salzman. 2007. 'Expectation Modulates Neural Responses to Pleasant and Aversive Stimuli in Primate Amygdala'. *Neuron* 55(6):970–84. doi: <https://doi.org/10.1016/j.neuron.2007.08.004>.
- Bergstrom, Hadley C., Craig G. McDonald, Smita Dey, Haying Tang, Reed G. Selwyn, and Luke R. Johnson. 2013. 'The Structure of Pavlovian Fear Conditioning in the Amygdala'. *Brain Structure and Function* 218(6):1569–89. doi: 10.1007/s00429-012-0478-2.
- Beyeler, Anna, Chia-Jung Chang, Margaux Silvestre, Clémentine Lévêque, Praneeth Namburi, Craig P. Wildes, and Kay M. Tye. 2018. 'Organization of Valence-Encoding and Projection-Defined Neurons in the Basolateral Amygdala'. *Cell Reports* 22(4):905–18. doi: <https://doi.org/10.1016/j.celrep.2017.12.097>.

- Beyeler, Anna, and Joanna Dabrowska. 2020. 'Chapter 3 - Neuronal Diversity of the Amygdala and the Bed Nucleus of the Stria Terminalis'. Pp. 63–100 in *Handbook of Behavioral Neuroscience*. Vol. 26, edited by J. H. Urban and J. A. Rosenkranz. Elsevier.
- Bickart, Kevin C., Bradford C. Dickerson, and Lisa Feldman Barrett. 2014. 'The Amygdala as a Hub in Brain Networks That Support Social Life'. *Neuropsychologia* 63:235–48. doi: <https://doi.org/10.1016/j.neuropsychologia.2014.08.013>.
- Björklund, Anders, Tomas G. M. Hökfelt, and Larry W. Swanson. 1987. 'Integrated Systems of the CNS'.
- BOOKHEIMER, SUSAN Y., A. TING WANG, ASHLEY SCOTT, MARIAN SIGMAN, and MIRELLA DAPRETTO. 2008. 'Frontal Contributions to Face Processing Differences in Autism: Evidence from FMRI of Inverted Face Processing'. *Journal of the International Neuropsychological Society* 14(6):922–32. doi: DOI: 10.1017/S135561770808140X.
- Boyden, Edward S., Feng Zhang, Ernst Bamberg, Georg Nagel, and Karl Deisseroth. 2005. 'Millisecond-Timescale, Genetically Targeted Optical Control of Neural Activity'. *Nature Neuroscience* 8(9):1263–68. doi: 10.1038/nn1525.
- Brown, Sanger, and Edward Albert Sharpey-Schafer. 1997. 'XI. An Investigation into the Functions of the Occipital and Temporal Lobes of the Monkey's Brain'. *Philosophical Transactions of the Royal Society of London. (B.)* 179:303–27. doi: 10.1098/rstb.1888.0011.
- Cador, M., T. W. Robbins, and B. J. Everitt. 1989. 'Involvement of the Amygdala in Stimulus-Reward Associations: Interaction with the Ventral Striatum'. *Neuroscience* 30(1):77–86. doi: [https://doi.org/10.1016/0306-4522\(89\)90354-0](https://doi.org/10.1016/0306-4522(89)90354-0).
- Cembrowski, Mark S. 2019. 'Single-Cell Transcriptomics as a Framework and Roadmap for Understanding the Brain'. *Journal of Neuroscience Methods* 326:108353. doi: <https://doi.org/10.1016/j.jneumeth.2019.108353>.
- Cembrowski, Mark S., Lihua Wang, Andrew L. Lemire, Monique Copeland, Salvatore F. DiLisio, Jody Clements, and Nelson Spruston. 2018. 'The Subiculum Is a Patchwork of Discrete Subregions' edited by L. Colgin and G. L. Westbrook. *ELife* 7:e37701. doi: 10.7554/eLife.37701.
- Chevallier, Coralie, Gregor Kohls, Vanessa Troiani, Edward S. Brodtkin, and Robert T. Schultz. 2012. 'The Social Motivation Theory of Autism'. *Trends in Cognitive Sciences* 16(4):231–39. doi: <https://doi.org/10.1016/j.tics.2012.02.007>.
- Choi, Gloria B., Hong-wei Dong, Andrew J. Murphy, David M. Valenzuela, George D. Yancopoulos, Larry W. Swanson, and David J. Anderson. 2005. 'Lhx6 Delineates a Pathway Mediating Innate Reproductive Behaviors from the Amygdala to the Hypothalamus'. *Neuron* 46(4):647–60. doi: <https://doi.org/10.1016/j.neuron.2005.04.011>.
- Chow, Brian Y., Xue Han, Allison S. Dobry, Xiaofeng Qian, Amy S. Chuong, Mingjie Li, Michael A. Henninger, Gabriel M. Belfort, Yingxi Lin, Patrick E. Monahan, and Edward S. Boyden.

2010. 'High-Performance Genetically Targetable Optical Neural Silencing by Light-Driven Proton Pumps'. *Nature* 463(7277):98–102. doi: 10.1038/nature08652.
- Cocas, Laura A., Goichi Miyoshi, Rosalind S. E. Carney, Vitor H. Sousa, Tsutomu Hirata, Kevin R. Jones, Gord Fishell, Molly M. Huntsman, and Joshua G. Corbin. 2009. 'Lineage Progenitors Differentially Contribute to Neural Diversity in the Striatum and Amygdala'. *The Journal of Neuroscience* 29(50):15933. doi: 10.1523/JNEUROSCI.2525-09.2009.
- Daviu, Nuria, Michael R. Bruchas, Bitá Moghaddam, Carmen Sandi, and Anna Beyeler. 2019. 'Neurobiological Links between Stress and Anxiety'. *Neurobiology of Stress* 11:100191. doi: <https://doi.org/10.1016/j.ynstr.2019.100191>.
- Djerdjaj, Anthony, Alexandra J. Ng, Nathaniel S. Rieger, and John P. Christianson. 2022. 'The Basolateral Amygdala to Posterior Insular Cortex Tract Is Necessary for Social Interaction with Stressed Juvenile Rats'. *Behavioural Brain Research* 435:114050. doi: <https://doi.org/10.1016/j.bbr.2022.114050>.
- Douglas, Lewis A., Elena I. Varlinskaya, and Linda P. Spear. 2004. 'Rewarding Properties of Social Interactions in Adolescent and Adult Male and Female Rats: Impact of Social versus Isolate Housing of Subjects and Partners'. *Developmental Psychobiology* 45(3):153–62. doi: <https://doi.org/10.1002/dev.20025>.
- Douglass, Amelia M., Hakan Kucukdereli, Marion Ponserre, Milica Markovic, Jan Gründemann, Cornelia Strobel, Pilar L. Alcalá Morales, Karl-Klaus Conzelmann, Andreas Lüthi, and Rüdiger Klein. 2017. 'Central Amygdala Circuits Modulate Food Consumption through a Positive-Valence Mechanism'. *Nature Neuroscience* 20(10):1384–94. doi: 10.1038/nn.4623.
- Duvarci, Sevil, and Denis Pare. 2014. 'Amygdala Microcircuits Controlling Learned Fear'. *Neuron* 82(5):966–80. doi: <https://doi.org/10.1016/j.neuron.2014.04.042>.
- Emiliani, Valentina, Adam E. Cohen, Karl Deisseroth, and Michael Häusser. 2015. 'All-Optical Interrogation of Neural Circuits'. *The Journal of Neuroscience* 35(41):13917. doi: 10.1523/JNEUROSCI.2916-15.2015.
- Emiliani, Valentina, Emilia Entcheva, Rainer Hedrich, Peter Hegemann, Kai R. Konrad, Christian Lüscher, Mathias Mahn, Zhuo-Hua Pan, Ruth R. Sims, Johannes Vierock, and Ofer Yizhar. 2022. 'Optogenetics for Light Control of Biological Systems'. *Nature Reviews Methods Primers* 2(1):55. doi: 10.1038/s43586-022-00136-4.
- Everitt, B. J., M. Cador, and T. W. Robbins. 1989. 'Interactions between the Amygdala and Ventral Striatum in Stimulus-Reward Associations: Studies Using a Second-Order Schedule of Sexual Reinforcement'. *Neuroscience* 30(1):63–75. doi: [https://doi.org/10.1016/0306-4522\(89\)90353-9](https://doi.org/10.1016/0306-4522(89)90353-9).
- Fanselow, Michael S., and Joseph E. LeDoux. 1999. 'Why We Think Plasticity Underlying Pavlovian Fear Conditioning Occurs in the Basolateral Amygdala'. *Neuron* 23(2):229–32.

- Felix-Ortiz, A. C., A. Burgos-Robles, N. D. Bhagat, C. A. Leppla, and K. M. Tye. 2016. 'Bidirectional Modulation of Anxiety-Related and Social Behaviors by Amygdala Projections to the Medial Prefrontal Cortex'. *Neuroscience* 321:197–209. doi: <https://doi.org/10.1016/j.neuroscience.2015.07.041>.
- Felix-Ortiz, Ada C., Anna Beyeler, Changwoo Seo, Christopher A. Leppla, Craig P. Wildes, and Kay M. Tye. 2013. 'BLA to VHPC Inputs Modulate Anxiety-Related Behaviors'. *Neuron* 79(4):658–64. doi: <https://doi.org/10.1016/j.neuron.2013.06.016>.
- Felix-Ortiz, Ada C., and Kay M. Tye. 2014. 'Amygdala Inputs to the Ventral Hippocampus Bidirectionally Modulate Social Behavior'. *The Journal of Neuroscience* 34(2):586. doi: 10.1523/JNEUROSCI.4257-13.2014.
- Ferrara, Nicole C., Sydney Trask, Alexandra Ritger, Mallika Padival, and J. Amiel Rosenkranz. 2022. 'Developmental Differences in Amygdala Projection Neuron Activation Associated with Isolation-Driven Changes in Social Preference'. *Frontiers in Behavioral Neuroscience* 16. doi: 10.3389/fnbeh.2022.956102.
- Ferrara, Nicole C., Sydney Trask, and J. Amiel Rosenkranz. 2021. 'Maturation of Amygdala Inputs Regulate Shifts in Social and Fear Behaviors: A Substrate for Developmental Effects of Stress'. *Neuroscience & Biobehavioral Reviews* 125:11–25. doi: <https://doi.org/10.1016/j.neubiorev.2021.01.021>.
- Ferri, Sarah L., Arati S. Kreibich, Matthew Torre, Cara T. Piccoli, Holly Dow, Ashley A. Pallathra, Hongzhe Li, Warren B. Bilker, Ruben C. Gur, Ted Abel, and Edward S. Brodtkin. 2016. 'Activation of Basolateral Amygdala in Juvenile C57BL/6J Mice during Social Approach Behavior'. *Neuroscience* 335:184–94. doi: <https://doi.org/10.1016/j.neuroscience.2016.08.006>.
- Folkes, Oakleigh M., Rita Báldi, Veronika Kondev, David J. Marcus, Nolan D. Hartley, Brandon D. Turner, Jade K. Ayers, Jordan J. Baechle, Maya P. Misra, Megan Altemus, Carrie A. Grueter, Brad A. Grueter, and Sachin Patel. 2020. 'An Endocannabinoid-Regulated Basolateral Amygdala–Nucleus Accumbens Circuit Modulates Sociability'. *The Journal of Clinical Investigation* 130(4):1728–42. doi: 10.1172/JCI131752.
- Freese, Jennifer L., and David G. Amaral. 2005. 'The Organization of Projections from the Amygdala to Visual Cortical Areas TE and V1 in the Macaque Monkey'. *Journal of Comparative Neurology* 486(4):295–317. doi: <https://doi.org/10.1002/cne.20520>.
- Ganella, Despina E., and Jee Hyun Kim. 2014. 'Developmental Rodent Models of Fear and Anxiety: From Neurobiology to Pharmacology'. *British Journal of Pharmacology* 171(20):4556–74. doi: <https://doi.org/10.1111/bph.12643>.
- Ganella, Despina E., Ly Dao Nguyen, Liubov Lee-Kardashyan, Leah E. Kim, Antonio G. Paolini, and Jee Hyun Kim. 2018. 'Neurocircuitry of Fear Extinction in Adult and Juvenile Rats'. *Behavioural Brain Research* 351:161–67. doi: <https://doi.org/10.1016/j.bbr.2018.06.001>.



- Ghosh, Kunal K., Laurie D. Burns, Eric D. Cocker, Axel Nimmerjahn, Yaniv Ziv, Abbas el Gamal, and Mark J. Schnitzer. 2011. 'Miniaturized Integration of a Fluorescence Microscope'. *Nature Methods* 8(10):871–78. doi: 10.1038/nmeth.1694.
- Goosens, Ki A., and Stephen Maren. 2001. 'Contextual and Auditory Fear Conditioning Are Mediated by the Lateral, Basal, and Central Amygdaloid Nuclei in Rats'. *Learning & Memory* 8(3):148–55.
- Gorski, Jessica A., Tiffany Talley, Mengsheng Qiu, Luis Puelles, John L. R. Rubenstein, and Kevin R. Jones. 2002. 'Cortical Excitatory Neurons and Glia, But Not GABAergic Neurons, Are Produced in the Emx1-Expressing Lineage'. *The Journal of Neuroscience* 22(15):6309. doi: 10.1523/JNEUROSCI.22-15-06309.2002.
- Gothard, Katalin. 2014. 'The Amygdalo-Motor Pathways and the Control of Facial Expressions'. *Frontiers in Neuroscience* 8. doi: 10.3389/fnins.2014.00043.
- Grienberger, Christine, Andrea Giovannucci, William Zeiger, and Carlos Portera-Cailliau. 2022. 'Two-Photon Calcium Imaging of Neuronal Activity'. *Nature Reviews Methods Primers* 2(1):67. doi: 10.1038/s43586-022-00147-1.
- Hatfield, Tammy, Jung-Soo Han, Michael Conley, Michela Gallagher, and Peter Holland. 1996. 'Neurotoxic Lesions of Basolateral, But Not Central, Amygdala Interfere with Pavlovian Second-Order Conditioning and Reinforcer Devaluation Effects'. *The Journal of Neuroscience* 16(16):5256. doi: 10.1523/JNEUROSCI.16-16-05256.1996.
- Hintiryan, Houri, Ian Bowman, David L. Johnson, Laura Korobkova, Muye Zhu, Neda Khanjani, Lin Gou, Lei Gao, Seita Yamashita, Michael S. Bienkowski, Luis Garcia, Nicholas N. Foster, Nora L. Benavidez, Monica Y. Song, Darrick Lo, Kaelan R. Cotter, Marlene Becerra, Sarvia Aquino, Chunru Cao, Ryan P. Cabeen, Jim Stanis, Marina Fayzullina, Sarah A. Ustrell, Tyler Boesen, Amanda J. Tugangui, Zheng-Gang Zhang, Bo Peng, Michael S. Fanselow, Peyman Golshani, Joel D. Hahn, Ian R. Wickersham, Giorgio A. Ascoli, Li I. Zhang, and Hong-Wei Dong. 2021. 'Connectivity Characterization of the Mouse Basolateral Amygdalar Complex'. *Nature Communications* 12(1):2859. doi: 10.1038/s41467-021-22915-5.
- Hiroi, N., and N. M. White. 1991. 'The Lateral Nucleus of the Amygdala Mediates Expression of the Amphetamine-Produced Conditioned Place Preference'. *The Journal of Neuroscience* 11(7):2107. doi: 10.1523/JNEUROSCI.11-07-02107.1991.
- Hochgerner, Hannah, Muhammad Tibi, Shai Netser, Osnat Ophir, Nuphar Reinhardt, Shelly Singh, Zhige Lin, Shlomo Wagner, and Amit Zeisel. 2022. 'Cell Types in the Mouse Amygdala and Their Transcriptional Response to Fear Conditioning'. *BioRxiv* 2022.10.25.513733. doi: 10.1101/2022.10.25.513733.
- Holland, Peter C., and Michela Gallagher. 1999. 'Amygdala Circuitry in Attentional and Representational Processes'. *Trends in Cognitive Sciences* 3(2):65–73. doi: [https://doi.org/10.1016/S1364-6613\(98\)01271-6](https://doi.org/10.1016/S1364-6613(98)01271-6).

- Huang, Wen-Chin, Aya Zucca, Jenna Levy, and Damon T. Page. 2020. 'Social Behavior Is Modulated by Valence-Encoding MPFC-Amygdala Sub-Circuitry'. *Cell Reports* 32(2):107899. doi: <https://doi.org/10.1016/j.celrep.2020.107899>.
- Janak, Patricia H., and Kay M. Tye. 2015. 'From Circuits to Behaviour in the Amygdala'. *Nature* 517(7534):284–92. doi: 10.1038/nature14188.
- Jarvis, Erich D., Onur Güntürkün, Laura Bruce, András Csillag, Harvey Karten, Wayne Kuenzel, Loreta Medina, George Paxinos, David J. Perkel, Toru Shimizu, Georg Striedter, J. Martin Wild, Gregory F. Ball, Jennifer Dugas-Ford, Sarah E. Durand, Gerald E. Hough, Scott Husband, Lubica Kubikova, Diane W. Lee, Claudio v Mello, Alice Powers, Connie Siang, Tom v Smulders, Kazuhiro Wada, Stephanie A. White, Keiko Yamamoto, Jing Yu, Anton Reiner, and Ann B. Butler. 2005. 'Avian Brains and a New Understanding of Vertebrate Brain Evolution'. *Nature Reviews Neuroscience* 6(2):151–59. doi: 10.1038/nrn1606.
- Jasnow, A. M., D. E. Ehrlich, D. C. Choi, J. Dabrowska, M. E. Bowers, K. M. McCullough, D. G. Rainnie, and K. J. Ressler. 2013. 'Thy1-Expressing Neurons in the Basolateral Amygdala May Mediate Fear Inhibition'. *Journal of Neuroscience* 33(25):10396–404. doi: 10.1523/JNEUROSCI.5539-12.2013.
- Jin, Hao, Z. Hershel Fishman, Mingyu Ye, Li Wang, and Charles S. Zuker. 2021. 'Top-Down Control of Sweet and Bitter Taste in the Mammalian Brain'. *Cell* 184(1):257-271.e16. doi: <https://doi.org/10.1016/j.cell.2020.12.014>.
- Johnson, Carolyn M., F. Alexandra Loucks, Hannah Peckler, A. Wren Thomas, Patricia H. Janak, and Linda Wilbrecht. 2016. 'Long-Range Orbitofrontal and Amygdala Axons Show Divergent Patterns of Maturation in the Frontal Cortex across Adolescence'. *Developmental Cognitive Neuroscience* 18:113–20. doi: <https://doi.org/10.1016/j.dcn.2016.01.005>.
- Josh Huang, Z., and Hongkui Zeng. 2013. 'Genetic Approaches to Neural Circuits in the Mouse'. *Annual Review of Neuroscience* 36(1):183–215. doi: 10.1146/annurev-neuro-062012-170307.
- Kantak, Kathleen M., Yolanda Black, Eric Valencia, Kristen Green-Jordan, and Howard B. Eichenbaum. 2002a. 'Dissociable Effects of Lidocaine Inactivation of the Rostral and Caudal Basolateral Amygdala on the Maintenance and Reinstatement of Cocaine-Seeking Behavior in Rats'. *The Journal of Neuroscience* 22(3):1126. doi: 10.1523/JNEUROSCI.22-03-01126.2002.
- Kantak, Kathleen M., Yolanda Black, Eric Valencia, Kristen Green-Jordan, and Howard B. Eichenbaum. 2002b. 'Dissociable Effects of Lidocaine Inactivation of the Rostral and Caudal Basolateral Amygdala on the Maintenance and Reinstatement of Cocaine-Seeking Behavior in Rats'. *The Journal of Neuroscience* 22(3):1126. doi: 10.1523/JNEUROSCI.22-03-01126.2002.
- Keaveney, Marianna K., Bahar Rahsepar, Hua-an Tseng, Fernando R. Fernandez, Rebecca A. Mount, Tina Ta, John A. White, Jim Berg, and Xue Han. 2020. 'CaMKII $\alpha$ -Positive

- Interneurons Identified via a MicroRNA-Based Viral Gene Targeting Strategy'. *The Journal of Neuroscience* 40(50):9576. doi: 10.1523/JNEUROSCI.2570-19.2020.
- Kennedy, Daniel P., and Ralph Adolphs. 2012. 'The Social Brain in Psychiatric and Neurological Disorders'. *Trends in Cognitive Sciences* 16(11):559–72. doi: <https://doi.org/10.1016/j.tics.2012.09.006>.
- Kim, Joshua, Michele Pignatelli, Sangyu Xu, Shigeyoshi Itohara, and Susumu Tonegawa. 2016. 'Antagonistic Negative and Positive Neurons of the Basolateral Amygdala'. *Nature Neuroscience* 19(12):1636–46. doi: 10.1038/nn.4414.
- Kim, Joshua, Xiangyu Zhang, Shruti Muralidhar, Sarah A. LeBlanc, and Susumu Tonegawa. 2017. 'Basolateral to Central Amygdala Neural Circuits for Appetitive Behaviors'. *Neuron* 93(6):1464-1479.e5. doi: <https://doi.org/10.1016/j.neuron.2017.02.034>.
- Kim, Somi, TaeHyun Kim, Hye-Ryeon Lee, Eun-Hye Jang, Hyun-Hee Ryu, Minkyung Kang, So-Young Rah, Juyoun Yoo, Bolam Lee, Jae-Ick Kim, Chae Seok Lim, Sang Jeong Kim, Uh-Hyun Kim, Yong-Seok Lee, and Bong-Kiun Kaang. 2016. 'Impaired Learning and Memory in CD38 Null Mutant Mice'. *Molecular Brain* 9(1):16. doi: 10.1186/s13041-016-0195-5.
- Kim, Sunwhi, Yong-Eun Kim, Inuk Song, Yusuke Ujihara, Namsoo Kim, Yong-Hui Jiang, Henry H. Yin, Tae-Ho Lee, and Il Hwan Kim. 2022. 'Neural Circuit Pathology Driven by Shank3 Mutation Disrupts Social Behaviors'. *Cell Reports* 39(10):110906. doi: <https://doi.org/10.1016/j.celrep.2022.110906>.
- Klein, Alexandra S., Nate Dolensek, Caroline Weiland, and Nadine Gogolla. 2021. 'Fear Balance Is Maintained by Bodily Feedback to the Insular Cortex in Mice'. *Science* 374(6570):1010–15. doi: 10.1126/science.abj8817.
- Kling, Arthur, Jane Lancaster, and Jerry Benitone. 1970. 'Amygdalectomy in the Free-Ranging Vervet (*Cercopithecus Aethiops*)'. *Journal of Psychiatric Research* 7(3):191–99. doi: [https://doi.org/10.1016/0022-3956\(70\)90006-3](https://doi.org/10.1016/0022-3956(70)90006-3).
- Klumpp, Heide, and Jacklynn M. Fitzgerald. 2018. 'Neuroimaging Predictors and Mechanisms of Treatment Response in Social Anxiety Disorder: An Overview of the Amygdala'. *Current Psychiatry Reports* 20(10):89. doi: 10.1007/s11920-018-0948-1.
- Kuerbitz, Jeffrey, Melinda Arnett, Sarah Ehrman, Michael T. Williams, Charles v Vorhees, Simon E. Fisher, Alistair N. Garratt, Louis J. Muglia, Ronald R. Waclaw, and Kenneth Campbell. 2018. 'Loss of Intercalated Cells (ITCs) in the Mouse Amygdala of Tshz1 Mutants Correlates with Fear, Depression, and Social Interaction Phenotypes'. *Journal of Neuroscience* 38(5):1160–77. doi: 10.1523/JNEUROSCI.1412-17.2017.
- Laine, Christopher M., Kevin M. Spitler, Clayton P. Mosher, and Katalin M. Gothard. 2009. 'Behavioral Triggers of Skin Conductance Responses and Their Neural Correlates in the Primate Amygdala'. *Journal of Neurophysiology* 101(4):1749–54. doi: 10.1152/jn.91110.2008.

- Lanuza, Enrique, Margarita Belekova, Alino Martínez-Marcos, Cristian Font, and Fernando Martínez-García. 1998a. 'Identification of the Reptilian Basolateral Amygdala: An Anatomical Investigation of the Afferents to the Posterior Dorsal Ventricular Ridge of the Lizard *Podarcis Hispanica*'. *European Journal of Neuroscience* 10(11):3517–34. doi: <https://doi.org/10.1046/j.1460-9568.1998.00363.x>.
- LeDoux, J. E., P. Cicchetti, A. Xagoraris, and L. M. Romanski. 1990. 'The Lateral Amygdaloid Nucleus: Sensory Interface of the Amygdala in Fear Conditioning'. *The Journal of Neuroscience* 10(4):1062. doi: 10.1523/JNEUROSCI.10-04-01062.1990.
- LeDoux, Joseph E. 2000. 'Emotion Circuits in the Brain'. *Annual Review of Neuroscience* 23(1):155–84. doi: 10.1146/annurev.neuro.23.1.155.
- Lee, Young Hee, Yu-Been Kim, Kyu Sik Kim, Mirae Jang, Ha Young Song, Sang-Ho Jung, Dong-Soo Ha, Joon Seok Park, Jaegwon Lee, Kyung Min Kim, Deok-Hyeon Cheon, Inhyeok Baek, Min-Gi Shin, Eun Jeong Lee, Sang Jeong Kim, and Hyung Jin Choi. 2023. 'Lateral Hypothalamic Leptin Receptor Neurons Drive Hunger-Gated Food-Seeking and Consummatory Behaviours in Male Mice'. *Nature Communications* 14(1):1486. doi: 10.1038/s41467-023-37044-4.
- Lein, Ed S., T. Grant Belgard, Michael Hawrylycz, and Zoltán Molnár. 2017. 'Transcriptomic Perspectives on Neocortical Structure, Development, Evolution, and Disease'. *Annual Review of Neuroscience* 40(1):629–52. doi: 10.1146/annurev-neuro-070815-013858.
- Li, Hao, Praneeth Namburi, Jacob M. Olson, Matilde Borio, Mackenzie E. Lemieux, Anna Beyeler, Gwendolyn G. Calhoun, Natsuko Hitora-Imamura, Austin A. Coley, Avraham Libster, Aneesh Bal, Xin Jin, Huan Wang, Caroline Jia, Sourav R. Choudhury, Xi Shi, Ada C. Felix-Ortiz, Verónica de la Fuente, Vanessa P. Barth, Hunter O. King, Ehsan M. Izadmehr, Jasmin S. Revanna, Kanha Batra, Kyle B. Fischer, Laurel R. Keyes, Nancy Padilla-Coreano, Cody A. Siciliano, Kenneth M. McCullough, Romy Wichmann, Kerry J. Ressler, Ila R. Fiete, Feng Zhang, Yulong Li, and Kay M. Tye. 2022. 'Neurotensin Orchestrates Valence Assignment in the Amygdala'. *Nature* 608(7923):586–92. doi: 10.1038/s41586-022-04964-y.
- L., PRICE J. 1987. 'The Limbic Region. II. The Amygdaloid Complex'. *Integrated Systems of the CNS* 0:279–388.
- Málková, Ludiše, David Gaffan, and Elisabeth A. Murray. 1997. 'Excitotoxic Lesions of the Amygdala Fail to Produce Impairment in Visual Learning for Auditory Secondary Reinforcement But Interfere with Reinforcer Devaluation Effects in Rhesus Monkeys'. *The Journal of Neuroscience* 17(15):6011. doi: 10.1523/JNEUROSCI.17-15-06011.1997.
- Maren, Stephen. 2005. 'Building and Burying Fear Memories in the Brain'. *The Neuroscientist* 11:89–99.
- Maren, Stephen, and Gregory J. Quirk. 2004. 'Neuronal Signalling of Fear Memory'. *Nature Reviews Neuroscience* 5(11):844–52. doi: 10.1038/nrn1535.

- Mascagni, F., A. J. McDonald, and J. R. Coleman. 1993. 'Corticoamygdaloid and Corticocortical Projections of the Rat Temporal Cortex: APhaseolus Vulgaris Leucoagglutinin Study'. *Neuroscience* 57(3):697–715. doi: [https://doi.org/10.1016/0306-4522\(93\)90016-9](https://doi.org/10.1016/0306-4522(93)90016-9).
- Massi, Léma, Kenta M. Hagihara, Julien Courtin, Julian Hinz, Christian Müller, Maria Sol Fustiñana, Chun Xu, Nikolaos Karalis, and Andreas Lüthi. 2023. 'Disynaptic Specificity of Serial Information Flow for Conditioned Fear'. *Science Advances* 9(3):eabq1637. doi: [10.1126/sciadv.abq1637](https://doi.org/10.1126/sciadv.abq1637).
- Mathys, Hansruedi, Jose Davila-Velderrain, Zhuyu Peng, Fan Gao, Shahin Mohammadi, Jennie Z. Young, Madhvi Menon, Liang He, Fatema Abdurrob, Xueqiao Jiang, Anthony J. Martorell, Richard M. Ransohoff, Brian P. Hafler, David A. Bennett, Manolis Kellis, and Li-Huei Tsai. 2019. 'Single-Cell Transcriptomic Analysis of Alzheimer's Disease'. *Nature* 570(7761):332–37. doi: [10.1038/s41586-019-1195-2](https://doi.org/10.1038/s41586-019-1195-2).
- Matson KJE, Sathyamurthy A, Johnson KR, Kelly MC, Kelley MW, Levine AJ. 2018. 'Isolation of Adult Spinal Cord Nuclei for Massively Parallel Single-Nucleus RNA Sequencing'. *J Vis Exp*.
- Matthews, Gillian A., Edward H. Nieh, Caitlin M. Vander Weele, Sarah A. Halbert, Roma V. Pradhan, Ariella S. Yosafat, Gordon F. Globler, Ehsan M. Izadmehr, Rain E. Thomas, Gabrielle D. Lacy, Craig P. Wildes, Mark A. Ungless, and Kay M. Tye. 2016. 'Dorsal Raphe Dopamine Neurons Represent the Experience of Social Isolation'. *Cell* 164(4):617–31. doi: <https://doi.org/10.1016/j.cell.2015.12.040>.
- McCullough, K. M., D. Choi, J. Guo, K. Zimmerman, J. Walton, D. G. Rainnie, and K. J. Ressler. 2016. 'Molecular Characterization of Thy1 Expressing Fear-Inhibiting Neurons within the Basolateral Amygdala'. *Nature Communications* 7. doi: [10.1038/ncomms13149](https://doi.org/10.1038/ncomms13149).
- McDonald, A. J., and J. R. Augustine. 1993. 'Localization of GABA-like Immunoreactivity in the Monkey Amygdala'. *Neuroscience* 52(2):281–94. doi: [https://doi.org/10.1016/0306-4522\(93\)90156-A](https://doi.org/10.1016/0306-4522(93)90156-A).
- McDonald, A J, J. F. Muller, and F. Mascagni. 2002. 'GABAergic Innervation of Alpha Type II Calcium/Calmodulin-Dependent Protein Kinase Immunoreactive Pyramidal Neurons in the Rat Basolateral Amygdala'. *Journal of Comparative Neurology* 446(3):199–218. doi: [10.1002/cne.10204](https://doi.org/10.1002/cne.10204).
- McDonald, Alexander J. 1982. 'Neurons of the Lateral and Basolateral Amygdaloid Nuclei: A Golgi Study in the Rat'. *Journal of Comparative Neurology* 212(3):293–312. doi: <https://doi.org/10.1002/cne.902120307>.
- McDonald, Alexander J. 1984. 'Neuronal Organization of the Lateral and Basolateral Amygdaloid Nuclei in the Rat'. *Journal of Comparative Neurology* 222(4):589–606. doi: <https://doi.org/10.1002/cne.902220410>.
- McDonald, Alexander J. 1998. 'Cortical Pathways to the Mammalian Amygdala'. *Progress in Neurobiology* 55(3):257–332. doi: [https://doi.org/10.1016/S0301-0082\(98\)00003-3](https://doi.org/10.1016/S0301-0082(98)00003-3).

- McDonald, Alexander J, Jay F. Muller, and Franco Mascagni. 2002. 'GABAergic Innervation of Alpha Type II Calcium/Calmodulin-Dependent Protein Kinase Immunoreactive Pyramidal Neurons in the Rat Basolateral Amygdala'. *Journal of Comparative Neurology* 446(3):199–218. doi: <https://doi.org/10.1002/cne.10204>.
- Medina, Loreta, Isabel Legaz, Gertrudis González, Fernando de Castro, John L. R. Rubenstein, and Luis Puelles. 2004. 'Expression of Dbx1, Neurogenin 2, Semaphorin 5A, Cadherin 8, and Emx1 Distinguish Ventral and Lateral Pallial Histogenetic Divisions in the Developing Mouse Claustroamygdaloid Complex'. *Journal of Comparative Neurology* 474(4):504–23. doi: <https://doi.org/10.1002/cne.20141>.
- Meyer-Lindenberg, Andreas, Gregor Domes, Peter Kirsch, and Markus Heinrichs. 2011. 'Oxytocin and Vasopressin in the Human Brain: Social Neuropeptides for Translational Medicine'. *Nature Reviews Neuroscience* 12(9):524–38. doi: 10.1038/nrn3044.
- Minxha, Juri, Clayton Mosher, Jeremiah K. Morrow, Adam N. Mamelak, Ralph Adolphs, Katalin M. Gothard, and Ueli Rutishauser. 2017. 'Fixations Gate Species-Specific Responses to Free Viewing of Faces in the Human and Macaque Amygdala'. *Cell Reports* 18(4):878–91. doi: <https://doi.org/10.1016/j.celrep.2016.12.083>.
- Morrison, Sara E., and C. Daniel Salzman. 2010. 'Re-Valuing the Amygdala'. *Current Opinion in Neurobiology* 20(2):221–30. doi: <https://doi.org/10.1016/j.conb.2010.02.007>.
- Munuera, Jérôme, Mattia Rigotti, and C. Daniel Salzman. 2018. 'Shared Neural Coding for Social Hierarchy and Reward Value in Primate Amygdala'. *Nature Neuroscience* 21(3):415–23. doi: 10.1038/s41593-018-0082-8.
- Nader, Karim, Glenn E. Schafe, and Joseph E. le Doux. 2000. 'Fear Memories Require Protein Synthesis in the Amygdala for Reconsolidation after Retrieval'. *Nature* 406(6797):722–26. doi: 10.1038/35021052.
- Nagel, Georg, Tanjef Szellas, Wolfram Huhn, Suneel Kateriya, Nona Adeishvili, Peter Berthold, Doris Ollig, Peter Hegemann, and Ernst Bamberg. 2003. 'Channelrhodopsin-2, a Directly Light-Gated Cation-Selective Membrane Channel'. *Proceedings of the National Academy of Sciences* 100(24):13940–45. doi: 10.1073/pnas.1936192100.
- Namburi, Praneeth, Anna Beyeler, Suzuko Yorozu, Gwendolyn G. Calhoon, Sarah A. Halbert, Romy Wichmann, Stephanie S. Holden, Kim L. Mertens, Melodi Anahtar, Ada C. Felix-Ortiz, Ian R. Wickersham, Jesse M. Gray, and Kay M. Tye. 2015a. 'A Circuit Mechanism for Differentiating Positive and Negative Associations'. *Nature* 520(7549):675–78. doi: 10.1038/nature14366.
- O'Leary, Timothy P., Kaitlin E. Sullivan, Lihua Wang, Jody Clements, Andrew L. Lemire, and Mark S. Cembrowski. 2020a. 'Extensive and Spatially Variable Within-Cell-Type Heterogeneity across the Basolateral Amygdala' edited by A. E. West, L. L. Colgin, and B. W. Okaty. *ELife* 9:e59003. doi: 10.7554/eLife.59003.

- Pare, Denis, and Sevil Duvarci. 2012. 'Amygdala Microcircuits Mediating Fear Expression and Extinction'. *Current Opinion in Neurobiology* 22(4):717–23. doi: <https://doi.org/10.1016/j.conb.2012.02.014>.
- Paton, Joseph J., Marina A. Belova, Sara E. Morrison, and C. Daniel Salzman. 2006. 'The Primate Amygdala Represents the Positive and Negative Value of Visual Stimuli during Learning'. *Nature* 439(7078):865–70. doi: 10.1038/nature04490.
- Peng, Yueqing, Sarah Gillis-Smith, Hao Jin, Dimitri Tränkner, Nicholas J. P. Ryba, and Charles S. Zuker. 2015a. 'Sweet and Bitter Taste in the Brain of Awake Behaving Animals'. *Nature* 527(7579):512–15. doi: 10.1038/nature15763.
- Phillips, R. G. ,. & LeDoux, J. E. 1992. *Differential Contribution of Amygdala and Hippocampus to Cued and Contextual Fear Conditioning*. *Behavioral Neuroscience*. Vols 106(2), 274–285.
- Pitkänen, Asla, Vesa Savander, and Joseph E. LeDoux. 1997. 'Organization of Intra-Amygdaloid Circuitries in the Rat: An Emerging Framework for Understanding Functions of the Amygdala'. *Trends in Neurosciences* 20(11):517–23. doi: [https://doi.org/10.1016/S0166-2236\(97\)01125-9](https://doi.org/10.1016/S0166-2236(97)01125-9).
- Ponserre, Marion, Federica Fermani, Louise Gaitanos, and Rüdiger Klein. 2022. 'Encoding of Environmental Cues in Central Amygdala Neurons during Foraging'. *Journal of Neuroscience* 42(18):3783–96. doi: 10.1523/JNEUROSCI.1791-21.2022.
- Rataj-Baniowska, Monika, Anna Niewiadomska-Cimicka, Marie Paschaki, Monika Szyszka-Niagolov, Laura Carramolino, Miguel Torres, Pascal Dollé, and Wojciech Krężel. 2015. 'Retinoic Acid Receptor  $\beta$  Controls Development of Striatonigral Projection Neurons through FGF-Dependent and Meis1-Dependent Mechanisms'. *The Journal of Neuroscience* 35(43):14467. doi: 10.1523/JNEUROSCI.1278-15.2015.
- Redondo, Roger L., Joshua Kim, Autumn L. Arons, Steve Ramirez, Xu Liu, and Susumu Tonegawa. 2014. 'Bidirectional Switch of the Valence Associated with a Hippocampal Contextual Memory Engram'. *Nature* 513(7518):426–30. doi: 10.1038/nature13725.
- Roesch, Matthew R., Guillem R. Esber, Jian Li, Nathaniel D. Daw, and Geoffrey Schoenbaum. 2012. 'Surprise! Neural Correlates of Pearce–Hall and Rescorla–Wagner Coexist within the Brain'. *European Journal of Neuroscience* 35(7):1190–1200. doi: <https://doi.org/10.1111/j.1460-9568.2011.07986.x>.
- Rogers-Carter, Morgan M., Anthony Djerdjaj, K. Bates Gribbons, Juan A. Varela, and John P. Christianson. 2019a. 'Insular Cortex Projections to Nucleus Accumbens Core Mediate Social Approach to Stressed Juvenile Rats'. *The Journal of Neuroscience* 39(44):8717. doi: 10.1523/JNEUROSCI.0316-19.2019.

- Romanski, Lizabeth M., and Joseph E. LeDoux. 1993. 'Information Cascade from Primary Auditory Cortex to the Amygdala: Corticocortical and Corticoamygdaloid Projections of Temporal Cortex in the Rat'. *Cerebral Cortex* 3(6):515–32. doi: 10.1093/cercor/3.6.515.
- Root, Cory M., Christine A. Denny, René Hen, and Richard Axel. 2014. 'The Participation of Cortical Amygdala in Innate, Odour-Driven Behaviour'. *Nature* 515(7526):269–73. doi: 10.1038/nature13897.
- Rossi, Mark A., Marcus L. Basiri, Yuejia Liu, Yoshiko Hashikawa, Koichi Hashikawa, Lief E. Fenno, Yoon Seok Kim, Charu Ramakrishnan, Karl Deisseroth, and Garret D. Stuber. 2021. 'Transcriptional and Functional Divergence in Lateral Hypothalamic Glutamate Neurons Projecting to the Lateral Habenula and Ventral Tegmental Area'. *Neuron* 109(23):3823–3837.e6. doi: <https://doi.org/10.1016/j.neuron.2021.09.020>.
- Roy F. Baumeister, Mark R. Leary. 2007. *The Need to Belong: Desire for Interpersonal Attachments as a Fundamental Human Motivation*.
- SAH, P., E. S. L. FABER, M. LOPEZ DE ARMENTIA, and J. POWER. 2003. 'The Amygdaloid Complex: Anatomy and Physiology'. *Physiological Reviews* 83(3):803–34. doi: 10.1152/physrev.00002.2003.
- Sah, P., and M. Lopez De Armentia. 2003. 'Excitatory Synaptic Transmission in the Lateral and Central Amygdala'. Pp. 67–77 in *Annals of the New York Academy of Sciences*. Vol. 985.
- Sangha, Susan, James Z. Chadick, and Patricia H. Janak. 2013. 'Safety Encoding in the Basal Amygdala'. *The Journal of Neuroscience* 33(9):3744. doi: 10.1523/JNEUROSCI.3302-12.2013.
- Sanghera, M. K., E. T. Rolls, and A. Roper-Hall. 1979. 'Visual Responses of Neurons in the Dorsolateral Amygdala of the Alert Monkey'. *Experimental Neurology* 63(3):610–26. doi: [https://doi.org/10.1016/0014-4886\(79\)90175-4](https://doi.org/10.1016/0014-4886(79)90175-4).
- Saunders, Arpiar, Evan Z. Macosko, Alec Wysoker, Melissa Goldman, Fenna M. Krienen, Heather de Rivera, Elizabeth Bien, Matthew Baum, Laura Bortolin, Shuyu Wang, Aleksandrina Goeva, James Nemesh, Nolan Kamitaki, Sara Brumbaugh, David Kulp, and Steven A. McCarroll. 2018. 'Molecular Diversity and Specializations among the Cells of the Adult Mouse Brain'. *Cell* 174(4):1015–1030.e16. doi: 10.1016/J.CELL.2018.07.028.
- Schoenbaum, Geoffrey, Andrea A. Chiba, and Michela Gallagher. 1998. 'Orbitofrontal Cortex and Basolateral Amygdala Encode Expected Outcomes during Learning'. *Nature Neuroscience* 1(2):155–59. doi: 10.1038/407.
- Schoenbaum, Geoffrey, Andrea A. Chiba, and Michela Gallagher. 1999. 'Neural Encoding in Orbitofrontal Cortex and Basolateral Amygdala during Olfactory Discrimination Learning'. *The Journal of Neuroscience* 19(5):1876. doi: 10.1523/JNEUROSCI.19-05-01876.1999.



- Shabel, Steven J., Will Schairer, Rachel J. Donahue, Victoria Powell, and Patricia H. Janak. 2011. 'Similar Neural Activity during Fear and Disgust in the Rat Basolateral Amygdala'. *PLOS ONE* 6(12):e27797-.
- Shen, Chen-Jie, Di Zheng, Ke-Xin Li, Jian-Ming Yang, Hao-Qi Pan, Xiao-Dan Yu, Jia-Yu Fu, Yi Zhu, Qi-Xin Sun, Meng-Yu Tang, Ying Zhang, Peng Sun, Yi Xie, Shumin Duan, Hailan Hu, and Xiao-Ming Li. 2019. 'Cannabinoid CB1 Receptors in the Amygdalar Cholecystokinin Glutamatergic Afferents to Nucleus Accumbens Modulate Depressive-like Behavior'. *Nature Medicine* 25(2):337–49. doi: 10.1038/s41591-018-0299-9.
- Sigurdsson, Torfi, Valérie Doyère, Christopher K. Cain, and Joseph E. LeDoux. 2007. 'Long-Term Potentiation in the Amygdala: A Cellular Mechanism of Fear Learning and Memory'. *Neuropharmacology* 52(1):215–27. doi: <https://doi.org/10.1016/j.neuropharm.2006.06.022>.
- So, Nina, Becca Franks, Sean Lim, and James P. Curley. 2015. 'A Social Network Approach Reveals Associations between Mouse Social Dominance and Brain Gene Expression'. *PLOS ONE* 10(7):e0134509-.
- Stuber, Garret D., Dennis R. Sparta, Alice M. Stamatakis, Wieke A. van Leeuwen, Juanita E. Hardjoprajitno, Saemi Cho, Kay M. Tye, Kimberly A. Kempadoo, Feng Zhang, Karl Deisseroth, and Antonello Bonci. 2011. 'Excitatory Transmission from the Amygdala to Nucleus Accumbens Facilitates Reward Seeking'. *Nature* 475(7356):377–80. doi: 10.1038/nature10194.
- Swanson, Larry W., and Gorica D. Petrovich. 1998. 'What Is the Amygdala?' *Trends in Neurosciences* 21(8):323–31. doi: [https://doi.org/10.1016/S0166-2236\(98\)01265-X](https://doi.org/10.1016/S0166-2236(98)01265-X).
- Takayanagi, Yuki, Masahide Yoshida, Akihide Takashima, Keiko Takanami, Shoma Yoshida, Katsuhiko Nishimori, Ichiko Nishijima, Hirotaka Sakamoto, Takanori Yamagata, and Tatsushi Onaka. 2017. 'Activation of Supraoptic Oxytocin Neurons by Secretin Facilitates Social Recognition'. *Biological Psychiatry* 81(3):243–51. doi: <https://doi.org/10.1016/j.biopsych.2015.11.021>.
- Tasic, Bosiljka, Vilas Menon, Thuc Nghi Nguyen, Tae Kyung Kim, Tim Jarsky, Zizhen Yao, Boaz Levi, Lucas T. Gray, Staci A. Sorensen, Tim Dolbeare, Darren Bertagnolli, Jeff Goldy, Nadiya Shapovalova, Sheana Parry, Changkyu Lee, Kimberly Smith, Amy Bernard, Linda Madisen, Susan M. Sunkin, Michael Hawrylycz, Christof Koch, and Hongkui Zeng. 2016a. 'Adult Mouse Cortical Cell Taxonomy Revealed by Single Cell Transcriptomics'. *Nature Neuroscience* 19(2):335–46. doi: 10.1038/nn.4216.
- Tian, Lin, S. Andrew Hires, Tianyi Mao, Daniel Huber, M. Eugenia Chiappe, Sreekanth H. Chalasani, Leopoldo Petreanu, Jasper Akerboom, Sean A. McKinney, Eric R. Schreiter, Cornelia I. Bargmann, Vivek Jayaraman, Karel Svoboda, and Loren L. Looger. 2009. 'Imaging Neural Activity in Worms, Flies and Mice with Improved GCaMP Calcium Indicators'. *Nature Methods* 6(12):875–81. doi: 10.1038/nmeth.1398.

- Tomova, Livia, Kimberly L. Wang, Todd Thompson, Gillian A. Matthews, Atsushi Takahashi, Kay M. Tye, and Rebecca Saxe. 2020. 'Acute Social Isolation Evokes Midbrain Craving Responses Similar to Hunger'. *Nature Neuroscience* 23(12):1597–1605. doi: 10.1038/s41593-020-00742-z.
- Tosches, Maria Antonietta, Tracy M. Yamawaki, Robert K. Naumann, Ariel A. Jacobi, Georgi Tushev, and Gilles Laurent. 2018. 'Evolution of Pallium, Hippocampus, and Cortical Cell Types Revealed by Single-Cell Transcriptomics in Reptiles'. *Science* 360(6391):881–88. doi: 10.1126/science.aar4237.
- Tremblay, Robin, Soohyun Lee, and Bernardo Rudy. 2016. 'GABAergic Interneurons in the Neocortex: From Cellular Properties to Circuits'. *Neuron* 91(2):260–92. doi: <https://doi.org/10.1016/j.neuron.2016.06.033>.
- Tye, Kay M., and Patricia H. Janak. 2007. 'Amygdala Neurons Differentially Encode Motivation and Reinforcement'. *The Journal of Neuroscience* 27(15):3937. doi: 10.1523/JNEUROSCI.5281-06.2007.
- Tye, Kay M., Rohit Prakash, Sung-Yon Kim, Lief E. Fenno, Logan Grosenick, Hosniya Zarabi, Kimberly R. Thompson, Viviana Gradinaru, Charu Ramakrishnan, and Karl Deisseroth. 2011. 'Amygdala Circuitry Mediating Reversible and Bidirectional Control of Anxiety'. *Nature* 471(7338):358–62. doi: 10.1038/nature09820.
- Tye, Kay M., Garret D. Stuber, Bram de Ridder, Antonello Bonci, and Patricia H. Janak. 2008. 'Rapid Strengthening of Thalamo-Amygdala Synapses Mediates Cue–Reward Learning'. *Nature* 453(7199):1253–57. doi: 10.1038/nature06963.
- Uwano, T., H. Nishijo, T. Ono, and R. Tamura. 1995. 'Neuronal Responsiveness to Various Sensory Stimuli, and Associative Learning in the Rat Amygdala'. *Neuroscience* 68(2):339–61. doi: [https://doi.org/10.1016/0306-4522\(95\)00125-3](https://doi.org/10.1016/0306-4522(95)00125-3).
- Wang, Yuhan, Mark Eddison, Greg Fleishman, Martin Weigert, Shengjin Xu, Tim Wang, Konrad Rokicki, Cristian Goina, Fredrick E. Henry, Andrew L. Lemire, Uwe Schmidt, Hui Yang, Karel Svoboda, Eugene W. Myers, Stephan Saalfeld, Wyatt Korff, Scott M. Sternson, and Paul W. Tillberg. 2021. 'EASI-FISH for Thick Tissue Defines Lateral Hypothalamus Spatio-Molecular Organization'. *Cell* 184(26):6361-6377.e24. doi: <https://doi.org/10.1016/j.cell.2021.11.024>.
- Wassum, Kate M., and Alicia Izquierdo. 2015. 'The Basolateral Amygdala in Reward Learning and Addiction'. *Neuroscience & Biobehavioral Reviews* 57:271–83. doi: <https://doi.org/10.1016/j.neubiorev.2015.08.017>.
- Wei, Ji-an, Qing Han, Zhihua Luo, Linglin Liu, Jing Cui, Jiahui Tan, Billy K. C. Chow, Kwok-Fai So, and Li Zhang. 2023. 'Amygdala Neural Ensemble Mediates Mouse Social Investigation Behaviors'. *National Science Review* 10(1):nwac179. doi: 10.1093/nsr/nwac179.

- Wu, Xiaoting, Xiangyu Yang, Lulu Song, Yang Wang, Yamin Li, Yuanyuan Liu, Xiaowei Yang, Yijun Wang, Weihua Pei, and Weidong Li. 2021. 'A Modified Miniscope System for Simultaneous Electrophysiology and Calcium Imaging in Vivo'. *Frontiers in Integrative Neuroscience* 15. doi: 10.3389/fnint.2021.682019.
- Yao, Zizhen, Cindy T. J. van Velthoven, Michael Kunst, Meng Zhang, Delissa McMillen, Changkyu Lee, Won Jung, Jeff Goldy, Aliya Abdelhak, Pamela Baker, Eliza Barkan, Darren Bertagnolli, Jazmin Campos, Daniel Carey, Tamara Casper, Anish Bhaswanth Chakka, Rushil Chakrabarty, Sakshi Chavan, Min Chen, Michael Clark, Jennie Close, Kirsten Crichton, Scott Daniel, Tim Dolbeare, Lauren Ellingwood, James Gee, Alexandra Glandon, Jessica Gloe, Joshua Gould, James Gray, Nathan Guilford, Junitta Guzman, Daniel Hirschstein, Windy Ho, Kelly Jin, Matthew Kroll, Kanan Lathia, Arielle Leon, Brian Long, Zoe Maltzer, Naomi Martin, Rachel McCue, Emma Meyerdierks, Thuc Nghi Nguyen, Trangthanh Pham, Christine Rimorin, Augustin Ruiz, Nadiya Shapovalova, Cliff Slaughterbeck, Josef Sulc, Michael Tieu, Amy Torkelson, Herman Tung, Nasmil Valera Cuevas, Katherine Wadhwani, Katelyn Ward, Boaz Levi, Colin Farrell, Carol L. Thompson, Shoaib Mufti, Chelsea M. Pagan, Lauren Kruse, Nick Dee, Susan M. Sunkin, Luke Esposito, Michael J. Hawrylycz, Jack Waters, Lydia Ng, Kimberly A. Smith, Bosiljka Tasic, Xiaowei Zhuang, and Hongkui Zeng. 2023. 'A High-Resolution Transcriptomic and Spatial Atlas of Cell Types in the Whole Mouse Brain'. *BioRxiv* 2023.03.06.531121. doi: 10.1101/2023.03.06.531121.
- Yu, Bin, Qianqian Zhang, Lin Lin, Xin Zhou, Wenji Ma, Shaonan Wen, Chunyue Li, Wei Wang, Qian Wu, Xiaoqun Wang, and Xiao-Ming Li. 2023. 'Molecular and Cellular Evolution of the Amygdala across Species Analyzed by Single-Nucleus Transcriptome Profiling'. *Cell Discovery* 9(1):19. doi: 10.1038/s41421-022-00506-y.
- Zhang, Feng, Li-Ping Wang, Martin Brauner, Jana F. Liewald, Kenneth Kay, Natalie Watzke, Phillip G. Wood, Ernst Bamberg, Georg Nagel, Alexander Gottschalk, and Karl Deisseroth. 2007. 'Multimodal Fast Optical Interrogation of Neural Circuitry'. *Nature* 446(7136):633–39. doi: 10.1038/nature05744.
- Zhang, Wujie, David M. Schneider, Marina A. Belova, Sara E. Morrison, Joseph J. Paton, and C. Daniel Salzman. 2013. 'Functional Circuits and Anatomical Distribution of Response Properties in the Primate Amygdala'. *The Journal of Neuroscience* 33(2):722. doi: 10.1523/JNEUROSCI.2970-12.2013.
- Zhang, Xian, Wuqiang Guan, Tao Yang, Alessandro Furlan, Xiong Xiao, Kai Yu, Xu An, William Galbavy, Charu Ramakrishnan, Karl Deisseroth, Kimberly Ritola, Adam Hantman, Miao He, Z. Josh Huang, and Bo Li. 2021. 'Genetically Identified Amygdala–Striatal Circuits for Valence-Specific Behaviors'. *Nature Neuroscience* 24(11):1586–1600. doi: 10.1038/s41593-021-00927-0.
- Zhang, Xiangyu, Joshua Kim, and Susumu Tonegawa. 2020. 'Amygdala Reward Neurons Form and Store Fear Extinction Memory'. *Neuron* 105(6):1077–1093.e7. doi: <https://doi.org/10.1016/j.neuron.2019.12.025>.

- Zirlinger, Mariela, Gabriel Kreiman, and David J. Anderson. 2001. 'Amygdala-Enriched Genes Identified by Microarray Technology Are Restricted to Specific Amygdaloid Subnuclei'. *Proceedings of the National Academy of Sciences* 98(9):5270–75. doi: 10.1073/pnas.091094698.
- Mollinedo-Gajate, I., Song, C., Knöpfel, T. (2019). Genetically Encoded Fluorescent Calcium and Voltage Indicators. In: Barrett, J., Page, C., Michel, M. (eds) *Concepts and Principles of Pharmacology. Handbook of Experimental Pharmacology*, vol 260. Springer, Cham. [https://doi.org/10.1007/164\\_2019\\_299](https://doi.org/10.1007/164_2019_299)
- Deisseroth, K. Optogenetics: 10 years of microbial opsins in neuroscience. *Nat Neurosci* 18, 1213–1225 (2015). <https://doi.org/10.1038/nn.4091>
- Lieselot L.G. Carrette, Elizabeth A. Sneddon, Olivier George, Chapter 8 - Amygdala circuits, Editor(s): NICHOLAS W. GILPIN, *Neurocircuitry of Addiction*, Academic Press, 2023, Pages 289-320, ISBN 9780128234532
- Pan, Y.; Cao, W.; Mu, Y.; Zhu, Q. Microfluidics Facilitates the Development of Single-Cell RNA Sequencing. *Biosensors* 2022, 12, 450. <https://doi.org/10.3390/bios12070450>

# Author Contributions

List of Contributors: Yue Zhang, Christian Peters, Tobias Straub

H.L designed, performed and analyzed sc/sn RNAseq, smFISH, optogenetic, calcium imaging and behavior experiments. Y.Z supported downstream calcium imaging analysis and C.P performed electrophysiology experiments. T.S supported snRNA data analysis

Munchen, 01. 10 .2023

Supervisor's Signature : Ruediger Klein

First author's Signature : Hansol Lim

## CV

### HANSOL LIM

#### EDUCATION

---

##### **Max-Planck-Institute of Neurobiology**

**Doctorate candidate (IMPRS doctorate program)** Planegg, Germany/  
Sep.2019-Present

- In the Department of Molecules – Signaling – Development (Prof.Dr. Ruediger Klein).
- Co-supported by IMPRS program and MPG PhD network.
- As a main member of the rewiring amygdala project using scRNA sequencing, virus-tracing, opto&chemogenetic manipulation, and in vivo calcium imaging with behavioral tasks
- Independent PhD project: Transcriptional and anatomical diversity in BLA neuronal cell types also encoding valence differently

##### **Goethe University**

**MSc, Interdisciplinary Neuroscience, GPA:1.2 (A, 4.3/4.5)** Frankfurt am Main, Germany/ 2017-2019

- Received DAAD Study Scholarships for Graduates of All disciplines from the Federal Republic of Germany.
- Received Johanna-Quandt Scholarship from European Forum Alpbach and Johanna Quandt Foundation.

### **Konkuk University**

**BSc, Animal biotechnology, GPA:4.48/4.5 (1.0 grade with 198 CP under EU Standard)** Seoul, South Korea/ March 2014

- Received All 4 years of academic excellent scholarship from the university.
- Graduation thesis: The current progress in understanding Parthenogenetic development.

## **Publication**

---

- Genetically- and spatially-defined basolateral amygdala neurons control food consumption and social interaction  
**Hansol Lim**<sup>1\*</sup>, Yue Zhang, Christian Peters, Tobias Straub, Ruediger Klein (Under revision, 2023)
- Transcriptomics reveals amygdala neuron regulation by fasting and ghrelin thereby promoting feeding Christian Peters<sup>1</sup>, Songwei He, Federica Fermani, **Hansol Lim**<sup>\*</sup>, Wenyu Ding, Christian Mayer, Ruediger Klein ( Science Advance 2023).
- Short- and Long-Term Plasticity of inhibition in Neocortical Layer 1 during Learning  
Leona Enke<sup>1</sup>, **Hansol Lim**<sup>1\*</sup>, Mahyar Moghimi, Sebastian Onasch, Julijana Gjorgjieva, Johannes J. Letzkus (in preparation)

## **REWARDS AND CERTIFICATES**

---

- Presented a poster at the Lake conference 2024, Thun, Swiss.
- Received the Travel awards by the Max Planck Florida Scientific Fellowship Program 2024.
- Participated in 2024 Neuroimaging Techniques Course, MPFI.
- Participated in Cajal course: Modern Approaches to Behavioural Analysis 2023
- Selected as a poster prize winner at GRC amygdala 2023
- Presented a poster at GRC/GRS amygdala 2023
- Selected & a poster presented on “Interact with circuit” Cajal summer school 2023

- Presented a poster in Cold Spring Harbor Laboratory Conference (Molecular Mechanisms of Neuronal Connectivity) 2022
- Presented a poster at the society of Neuroscience (SFN) 2022, San Diego, USA
- Participated in Neuroscience School of Advanced Studies summer school 2022 (Learning and Memory Cellular and System Mechanisms)
- Certificate for 22nd EMBL PhD Symposium: The Roaring 20s: A New Decade for Life Sciences.
- Participant at the Cold Spring Harbor Laboratory Conference: Molecular Mechanisms of Neuronal Connectivity 2021
- Certificate for EMBL Virtual starting single-cell RNA seq Analysis course
- Certificate of participation: Neurizons 2020: networks grow, ideas flow
- 2021 scholarship by Rosa-Laura and Harmut Wekerle Foundation
- Certificate of GMP basic course by Humboldt University Berlin 2020
- Certificate of Poster oral presentation skill course by natural science careers 2020
- Received DAAD Study Scholarships for Graduates of All disciplines from the Federal Republic of Germany 2019
- Received Johanna-Quandt Scholarship from European Forum Alpbach and Johanna Quandt Foundation 2019
- Poster presented at Neuro EPFL Symposium 2019 “Fear Learning: from neuronal circuits to translation” 2019

## RESEARCH AND TECHNICAL EXPERIENCE

---

**Letzkus group/ Max Planck Institute for Brain Research Frankfurt am Main/Sep 2018-2019 Master Thesis Project:**

**-title: Learning induced plasticity of layer 1 interneuron responses in primary auditory cortex**

- Main research: how activity in Layer 1 NDNF inhibitory interneurons changes with operant learning via 2-photon calcium imaging of layer 1 interneurons in head-fixed mice (NDNF-Ires-Cre ERT mice with viral injection: AAV2.1- CAG-flex-GCaMP6f & AAV2.1-CAG-flex-tdTom)
- Also, to find out how inhibition of NDNF neurons modulates other neuronal activities, somatostatin and pyramidal neurons have been imaged and analyzed for the related neuronal circuit.
- With longitudinal research during the whole 14days learning period, NDNF and SST neurons are inhibited through learning but pyramidal neurons are more activated.

**Gottschalk group/ Buchmann institute for Molecular Life Science, Goethe University**  
Aug-Sep 2018 internship

- Introduced new optogenetic tools (bPAC) to zebrafish lines by using crossbreeding, cloning, and transgenesis.
- Analyzed the change of behavior during stimulation on ChR2 and bPAC in zebrafishes caused by synaptic transmission between motor neurons and muscle cells indirectly.

**Letzkus group/ Max Planck Institute for Brain Research June-Aug 2018 intern**

- Characterized the basic properties of different, genetically- identified cortical neurons, especially layer 5 pyramidal neurons, by using in vitro patch clamp recording in slice of mouse auditory cortex.
- Participated in ongoing experiments that address the circuit mechanism of auditory fear learning and memory expression in vivo.

**Gaese group/Inst. Cell Biology and Neuroscience / Goethe University March-May 2018 intern**

- Investigated brain activity underlying the processing of sensory information in the auditory domain with electrophysiological single-cell techniques in rodents in the awake and anesthetized preparations; ABR and extracellular IC recording.
- Measured neuronal activity in different configurations of in-vivo recording techniques; ASR.
- Analyzed larger data sets via software (Matlab) for data handling, signal processing, statistical analysis and graphical display.

**Klein Group/ Department of Pharmacology for Scientists/ Goethe University**  
Feb 2018- Dec 2017 intern

- Manufactured probes for microdialysis studies and carried out measurements of neurotransmitters (e.g. acetylcholine, glutamate) and energy metabolites (glucose, lactate) via chromatographic (HPLC)
- Analyzed the change of metabolism under local injection of Metformin via Retro microdialysis in the hypothalamus.
- Collected CSF from Cisterna Magna for more precise CSF control through punctation of capillaries.

**SK Chemicals/Seoul, Korea, 2014-2016**

**Junior researcher (full-time permanent employed)**

- Checked GMP documents and reports.
- Translated Korean to English documents (Vaccine study reports and Quality documents)



- Coordinate joint-vaccine projects with Sanofi Pasteur and assist researchers; with pneumococcal conjugate vaccine (PCV), and meningococcal conjugate vaccine.
- Supporting An-dong vaccine factory Quality system.

## LEADERSHIP & ADDITIONAL EXPERIENCE

---

### **European Forum Alpbach** Alpbach, Austria/

Aug 2018 Summer program

Studied microbiome and new technique with nanoparticles during medical symposium.

Exchanged critical thinking of European immigration laws and international relationship.

Addressed more opportunity for natural scientists to insist their opinions for being reflected to legal proposals.

### **Konkuk University** Seoul, South Korea/ 2013-2014 Teaching assistant

- Assisted and tutored for 150 fresh biology undergraduates for group works in several practical courses.
- Taught weekly discussion sections and lab course for 100 new undergraduates by helping PhD fellows.
- Introduced and scheduled mutual discussion between faculties, professors and representatives of undergraduates for better curriculum.

### **University of Malaysia** Kuala Lumpur, Malaysia/ 2012 Culture Exchange program

- Introduced Korean educational system and online studying based on internet to faculties and Malaysia undergraduates.
- Learned the religion of Islam and the life styles based on The Koran and respect to the diversity.
- Mutual discussion by suggesting the better strategy for exchange of culture and education system.

### **University of Queensland** Brisbane, Australia/ 2011

Undergraduate Exchange program

- Rotated several labs in department of biology and learned different methodology compared to Korea system.
- Studied especially marine ecosystem by directly experiencing various marine lives.
- Proposed to the director of exchange program for opening practical training courses for international students.

### **Local Open study organization (NGO)** Seoul, Korea/ 2009-2014 Tutor

- Taught English, mathematics and biology to children in the underprivileged.
- Mentored 2 high school students on exploring career opportunities and setting important development goals.

- Educational volunteer works in Laos and Cambodia with KOICA (Cooperation Agency from Korea government)

## **SKILLS & INTERESTS**

---

### **Skills:**

- Computer/Technical: Microsoft Office, Linux, Adobe Photoshop & Illustrator.
- Bioinformatics: Experience with Python (intermediate), R (intermediate), MATLAB (beginner), GraphPad Prism.
- FELASA: Both of Theory and Practice Courses on Laboratory Animals-Function A, D and C\*
- Language: Korean (Native), English (Bilingual proficiency), German (Beginner)

### **Affiliations:**

- Germany scholarship Alumni of EFA, DAAD
- IMPRS PhD program member

### **Personality:**

- Professional Qualities, Responsible, High motivation, Hard worker and open mind.